UNIVERSITAT
POLITÈCNICA
DE VALÈNCIA

Numerical and Physical Modelling Approaches to the Study of the Hydraulic Jump and its Application in Large-Dam Stilling Basins

Juan Francisco Macián Pérez

Supervisors: Dr. Rafael L. García Bartual & Dr. Francisco J. Vallés Morán

Thesis submitted for the degree of Doctor of Philosophy at Universitat Politècnica de València (Valencia, Spain), July 2020

Declaration by the Author

The author declares that, except where due reference has been made in the text, this thesis is composed of original work that has not been submitted in whole or in part for consideration for any other degree or qualification in this, or any other university. The contributions by others to the thesis, through collaborations or jointly-authored works, have been clearly specified and acknowledged in the text.

Juan Francisco Macián Pérez

June 2020

Scientific Contributions Derived from the Research

Macián-Pérez, J. F., Bayón, A., García-Bartual, R., López-Jiménez, P.A. and Vallés-Morán, F. J. (2020). "Characterization of structural properties in a high Reynolds hydraulic jump based on CFD and physical modeling approaches," *J. Hydraul. Eng.* (accepted for publication).

Macián-Pérez, J. F., Vallés-Morán, F. J., Sánchez-Gómez, S., De-Rossi-Estrada, M. and García-Bartual, R. (2020). "Experimental Characterization of the Hydraulic Jump Profile and Velocity Distribution in a Stilling Basin Physical Model," *Water*, vol. 12, no. 6, p. 1758.

Macián-Pérez, J. F., García-Bartual, R., Huber, B., Bayón, A. and Vallés-Morán, F. J. (2020). "Analysis of the Flow in a Typified USBR II Stilling Basin through a Numerical and Physical Modeling Approach," *Water*, vol. 12, no. 1, p. 227.

Macián-Pérez, J. F., Huber, B., Bayón, A., García-Bartual, R. and Vallés-Morán, F. J. (2019). "Influencia de la elección del modelo de turbulencia en el análisis numérico CFD de un cuenco amortiguador tipificado USBR II," in *VI Jorandas de Ingeniería del Agua, Toledo, Spain*.

Macián-Pérez, J. F., García-Bartual, R., Huber, B., Bayón, A. and Vallés-Morán, F. J. (2019). "Approach to the void fraction distribution within a hydraulic jump in a typified USBR II stilling basin," in *E-proceedings of the 38th IAHR World Congress, Panama City, Panama*.

Bayón, A., Macián-Pérez, J. F., Vallés-Morán, F. J. and López-Jiménez, P. A., (2019). "Effect of RANS turbulence model in hydraulic jump CFD simulations," in *E-proceedings of the 38th IAHR World Congress, Panama City, Panama*.

Macián-Pérez, J. F., Bayón, A., Vallés-Morán, F. J., García-Bartual, R. and López-Jiménez, P.A. (2017). "Caracterización experimental de resaltos hidráulicos estacionarios con alto número de Reynolds," in *V Jorandas de Ingeniería del Agua, A Coruña, Spain*.

Agradecimientos

En primer lugar, me gustaría agradecer todo su apoyo a mis directores, Rafa y Paco. Gracias por haber compartido conmigo vuestro conocimiento y vuestros consejos pero sobre todo, gracias por haberme tratado como a un igual y por haber confiado en mí siempre, más que yo mismo. Gracias también al resto de compañeros de la UPV. A Arnau, por tu ayuda y los caminos que me has abierto. A Bea, por tu ejemplo y por haber cuidado de mí en todo momento. A Ximo y Carlos, gracias por vuestro trabajo y por los almuerzos. A Andrea, gracias por escucharme, por no darme siempre la razón y por hacerme mejorar. Me gustaría agradecer también su colaboración en la campaña experimental a Pepe, Santi, Marco y el resto de compañeros de topografía.

Tampoco puedo olvidarme de Boris, Koen y el resto de compañeros de la Universidad Técnica de Viena. Gracias, no solo por colaborar en esta investigación, sino también por vuestra acogida y por hacer mi estancia tan agradable.

Gracias a mis amigos por alegrarme la vida. A los de Valencia. Después de tanto tiempo, no me cabe duda de que sois todos especiales. No podría haber imaginado mejores personas con las que compartir tantas y tantas cosas. A los de Bejís. Gracias por la tranquilidad y los buenos momentos cada vez que nos juntamos. A los de la universidad y a los de Cranfield. Gracias por las experiencias inolvidables y por vuestro cariño.

Gracias a toda mi familia. Gracias por vuestro amor y vuestra confianza incondicionales. A mis padres y a mi hermano. Gracias por aguantar mis frustraciones, por guiarme y por todo lo que aprendo de vosotros. A vuestro lado es imposible perderse.

Por último, gracias a mi abuelo. Trabajo para intentar ser la mitad de lo que tú eras. Te echo de menos.

Funding Information

The research here presented was funded by ‘Generalitat Valenciana predoctoral grants (Grant number [2015/7521])’, in collaboration with the European Social Funds and by the research project ‘La aireación del flujo y su implementación en prototipo para la mejora de la disipación de energía de la lámina vertiente por resalto hidráulico en distintos tipos de presas’ (BIA2017-85412-C2-1-R), funded by the Spanish Ministry of Economy in cooperation with European FEDER funds.

"Las cosas podían haber sucedido de cualquier otra manera y, sin embargo, sucedieron así."

Miguel Delibes (El camino)

Abstract

The hydraulic jump constitutes one of the most complex phenomena with application in hydraulic engineering. On the one hand, a series of features bound to the hydraulic jump nature, such as the large turbulent fluctuations, the intense air entrainment and the significant energy dissipation, contribute to build its complexity, which places the current knowledge far from a full understanding of the phenomenon. On the other hand, it is precisely this energy dissipating nature that justifies its use in large-dam stilling basins, which constitutes its main practical application.

Hence, the research here presented aimed to contribute to the general knowledge of the hydraulic jump phenomenon and its application for energy dissipation purposes in large-dam stilling basins. To this end, the bases of the phenomenon were addressed by characterising a classical hydraulic jump (CHJ). The research was conducted under a double numerical and physical modelling approach. Computational Fluid Dynamics (CFD) techniques were employed to simulate the hydraulic jump, whereas an experimental campaign in a physical model designed for the purpose was carried out too. The most relevant hydraulic jump characteristics were investigated, including sequent depths ratio, hydraulic jump efficiency, roller length, free surface profile, distributions of velocity and pressure, hydraulic jump length and fluctuating variables. The results from the physical and the numerical models were compared not only between them, but also with bibliographic information coming from an extensive literature review. It was found that both modelling approaches were able to accurately represent the hydraulic jump free surface profile, roller length, efficiency and sequent depths ratio, consistently with previous research. Some significant differences were found between models regarding velocity distributions and pressure fluctuations, although in general, the results were in good agreement with bibliographic data and expressions, showing the suitability of the methodology employed to analyse the phenomenon under study.

Once the characterisation of the CHJ was carried out, the analysis of an energy dissipation stilling basin was developed. In particular, a general and representative case study consisting in a typified USBR II stilling basin was analysed through a physical and numerical modelling approach. In addition, the modelled results were compared with data and expressions coming from a bibliographic review. This comparison was intended to assess the particular characteristics of the hydraulic jump in a large-dam

stilling basin, as well as the affection of the energy dissipation devices to the flow. The analysis involved the hydraulic jump shape, velocity profiles, pressure and void fraction distributions. The results revealed not only similarities to the CHJ, but also the influence of the energy dissipation devices existing in the stilling basin, all in good agreement with bibliographic information, despite some slight differences. Consequently, the presented modelling approach showed to be a useful tool to address free surface flows occurring in stilling basins.

Overall, the presented research encouraged the use of methodologies based on a double numerical and physical modelling approach in the study of complex flows in hydraulic structures. In particular, the results reported contribute to the enhancement of the knowledge concerning the CHJ and the flow in a typified USBR II stilling basin. These results can be used to improve the design of large-dam energy dissipation structures. This is a key issue in hydraulic engineering, especially in the recent years. Thus, there is an increasing urgency for the adaptation of existing stilling basins, which must cope with higher discharges than those considered in their original design. The adaptation of these structures becomes even more important due to climate change effects and increasing society demands regarding security and flood protection. In these terms, contributions to hydraulic jump modelling, as the ones presented in this research, are crucial to face the challenge of energy dissipation structures adaptation.

Resumen

El resalto hidráulico constituye uno de los fenómenos más complejos con aplicación en el campo de la ingeniería hidráulica. Por un lado, las propias características del resalto, entre las que se encuentran las grandes fluctuaciones turbulentas, la intensa entrada de aire y una disipación de energía muy significativa, contribuyen a su complejidad situando el conocimiento actual del fenómeno lejos de una comprensión total del mismo. Por otro lado, es precisamente la naturaleza disipadora de energía del resalto la que da lugar a su principal aplicación práctica.

Así pues, la investigación que aquí se presenta trata de contribuir al conocimiento general del resalto hidráulico y su aplicación para disipar energía en cuencos amortiguadores de grandes presas. Para ello, se abordaron las bases del fenómeno mediante la caracterización de un resalto hidráulico clásico (RHC). La investigación se llevó a cabo bajo una doble perspectiva de modelación numérica y física. Se emplearon técnicas de Dinámica de Fluidos Computacional (DFC) para la realización de simulaciones de este resalto hidráulico, a la vez que se llevó a cabo una campaña experimental en un modelo físico específicamente diseñado para tratar el caso. De este modo, se abordaron los aspectos más relevantes del resalto hidráulico, incluyendo el ratio de calados conjugados, la eficiencia del resalto, la longitud de la zona de recirculación, el perfil de la lámina libre, las distribuciones de velocidad y presión, la longitud del resalto y el análisis de frecuencias. Los resultados de los modelos físico y numérico fueron comparados, no solo entre ellos, sino también con información de otros autores procedente de una extensa revisión bibliográfica. Ambos modelos mostraron su capacidad para representar con precisión la lámina libre del resalto hidráulico, la longitud de la zona de recirculación, la eficiencia y el ratio de calados conjugados, de acuerdo con las fuentes de contraste. Con respecto a las distribuciones de velocidad y presión, los modelos mostraron ciertas discrepancias, a pesar de que, en general, los resultados se situaron en la línea de los datos y expresiones bibliográficas. En base a este análisis se observa que la metodología empleada resulta adecuada para la investigación del fenómeno a estudiar.

Una vez llevada a cabo la caracterización del RHC, se procedió a analizar un cuenco amortiguador para disipación de energía. En particular, se estudió un caso general y representativo de cuenco amortiguador tipificado USBR II, a partir de la doble perspectiva de modelación física y numérica. Asimismo, los resultados se compararon

con datos y expresiones bibliográficas. Esta comparación pretendía evaluar los rasgos particulares del resalto hidráulico en cuencos amortiguadores de grandes presas, así como la influencia de los elementos disipadores de energía en el flujo. El análisis incluyó la forma del resalto hidráulico, perfiles de velocidad, presiones y distribución de la fracción de vacío. Los resultados revelaron ciertas similitudes con el RHC, pero también la influencia de los elementos disipadores de energía presentes en el cuenco amortiguador. Todos estos resultados mostraron estar en la línea de las investigaciones de otros autores, más allá de ciertas diferencias relativamente pequeñas. En consecuencia, la metodología desarrollada muestra su utilidad para abordar el estudio del flujo en cuencos amortiguadores.

En general, la investigación que aquí se presenta respalda el uso de una metodología de modelación desde la doble perspectiva física y numérica, para el estudio de flujos complejos y su interacción con estructuras hidráulicas. En concreto, los resultados presentados contribuyen a expandir el conocimiento sobre el RHC y el flujo en un cuenco amortiguador tipificado USBR II. Así pues, los resultados pueden emplearse para mejorar el diseño de estructuras de disipación de energía en grandes presas. Durante los últimos años, la adaptación de cuencos amortiguadores a caudales superiores a los empleados para su diseño ha ganado gran relevancia. Esta adaptación resulta clave por los efectos del cambio climáticos y las crecientes exigencias de la sociedad en materia de seguridad y protección frente a avenidas. De este modo, toda contribución a la modelación de resaltos hidráulicos, como la que aquí se presenta, resulta crucial para afrontar el reto de la adaptación de las estructuras hidráulicas para disipación de energía.

Resum

El ressalt hidràulic constitueix un dels fenòmens de major complexitat amb aplicació en el camp de l'enginyeria hidràulica. D'una banda, les característiques del propi ressalt, com poden ser les grans fluctuacions turbulentes, la intensa entrada d'aire i una dissipació d'energia molt significativa, contribueixen a la seua complexitat, de manera que el coneixement actual del ressalt està lluny d'una comprensió total del mateix. D'altra banda, és precisament la gran dissipació d'energia associada al ressalt la que motiva la seua principal aplicació pràctica.

La investigació que ací es presenta tracta de contribuir al coneixement general del ressalt hidràulic i la seua aplicació per dissipar energia al vas esmorteïdor de grans preses. En primer lloc, s'abordaren les bases del fenomen mitjançant la caracterització d'un ressalt hidràulic clàssic (RHC). La investigació es va dur a terme sota una doble perspectiva de modelització física i numèrica. El ressalt hidràulic es va simular emprant tècniques de Dinàmica de Fluids Computacional (DFC), mentre paral·lelament es desenvolupava una campanya experimental amb un model físic específicament dissenyat per tractar aquest cas. D'aquesta manera, es van abordar els aspectes més rellevants del ressalt, incloent el ràtio de calats conjugats, l'eficiència, la llargària de la regió de recirculació, el perfil de la superfície lliure, les distribucions de velocitat i pressió, la llargària del ressalt i l'anàlisi de freqüències. Els resultats dels models físic i numèric es compararen, no solament entre ells, sinó també amb informació procedent d'una extensa revisió bibliogràfica. Ambdós models van mostrar la seua capacitat per reproduir amb precisió la superfície lliure del ressalt, la llargària de la regió de recirculació, l'eficiència i el ràtio de calats conjugats, d'acord amb les fonts de comparació. Pel que fa a les distribucions de velocitat i pressió, els models mostraren lleugeres discrepàncies, tot i que en general els resultats se situaren en la línia de les dades i expressions bibliogràfiques. Prenent aquest anàlisi, s'observa que la metodologia desenvolupada resulta apropiada per investigar fenòmens com el ressalt hidràulic.

Caracteritzat el RHC, s'analitzà un vas esmorteïdor amb funció dissipadora d'energia. Concretament, s'estudià un cas general i representatiu de vas esmorteïdor tipificat USBR II, partint de la doble perspectiva de modelització física i numèrica. Així mateix, els resultats es van comparar amb dades i expressions bibliogràfiques. Aquesta comparació pretenia avaluar les particularitats del ressalt hidràulic al vas esmorteïdor

de grans preses, així com la influència al flux dels elements dissipadors d'energia. L'anàlisi inclogué la forma del ressalt, perfils de velocitat, pressions i distribució de la fracció de buit. Els resultats van revelar similituds amb el RHC, però també la influència dels elements dissipadors d'energia que formen part del vas esmorteïdor. D'aquesta manera, els resultats es situaren en la línia d'investigacions d'altes autors, més enllà de les lleugeres diferències reportades. En conseqüència, la metodologia desenvolupada mostra la seua utilitat per abordar l'estudi del flux en estructures de dissipació d'energia.

En general, la investigació ací presentada recolza l'ús d'una metodologia de modelització basada en la doble perspectiva física i numèrica, per estudiar fluxos d'elevada complexitat i la seua interacció amb estructures hidràuliques. En particular, els resultats contribueixen a expandir el coneixement relatiu al RHC i al flux en un vas esmorteïdor tipificat USBR II. Així, aquests resultats poden ser utilitzats per millorar el disseny de les estructures de dissipació d'energia de grans preses. Durant els últims anys, l'adaptació de vasos esmorteïdors a cabals superiors als considerats en la seua fase de disseny ha guanyat especial rellevància. Aquesta adaptació resulta crucial pels efectes del canvi climàtic i les creixents demandes de la societat en matèria de seguretat i protecció front a inundacions. En definitiva, tota contribució a la modelització de ressalts hidràulics, com la que ací es presenta, és de gran importància per afrontar el repte de l'adaptació d'estructures hidràuliques dissipadores d'energia.

Graphical Abstract

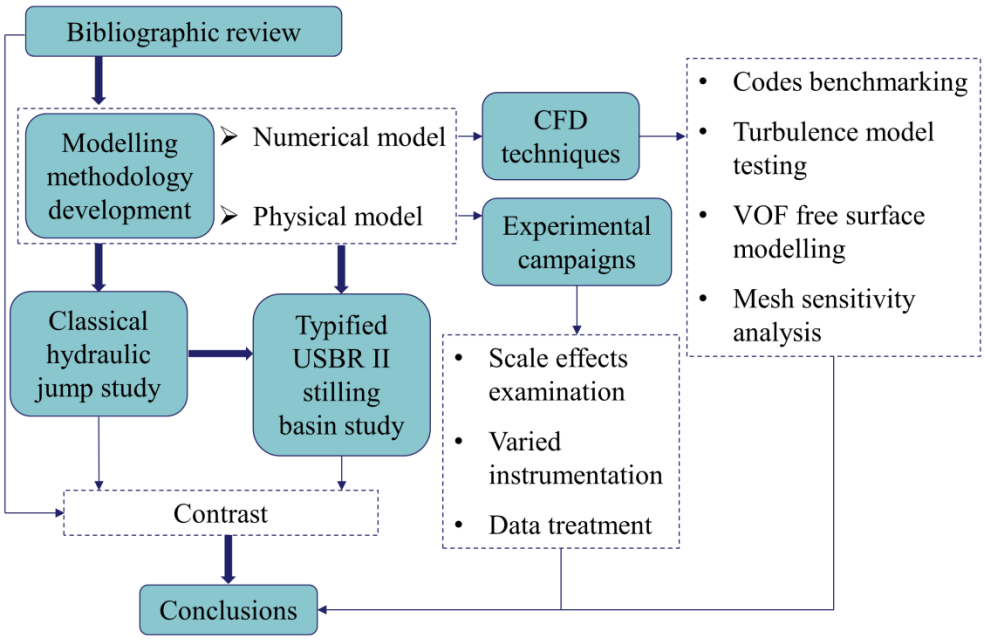

Keywords

Hydraulic jump; USBR II stilling basin; Physical model; Numerical model; CFD; FLOW-3D®

Table of Contents

List of Figures

List of Tables

Nomenclature

Roman Symbols

A	Constant for the maximum void fraction trend
A_P	Cross-sectional area per unit volume of the dispersed phase
A_S	Free surface area in a cell
a	Constant for the calculation of streambed pressure fluctuations
b	Hydraulic jump width
C	Void fraction
C_{max}	Maximum void fraction
$C_{1\varepsilon}$	Parameter for the RNG $k-\varepsilon$ turbulence model
$C_{2\varepsilon}$	Parameter for the RNG $k-\varepsilon$ turbulence model
C_D	Drag coefficient for the drift-flux model
C_d	Drag coefficient for the energy dissipation devices
C_{dis}	Discharge coefficient
C_μ	Parameter for the RNG $k-\varepsilon$ turbulence model
Cr	Courant number
D	Diffusion coefficient
d_1	Chute blocks height
d_2	End sill height
e_2	End sill top width
F	Fraction of fluid
F_d	Drag force
f	Dominant frequency
f_b	Body forces
Fr_1	Inflow Froude number
g	Gravity acceleration
H_{01}	Supercritical specific energy head
H_{02}	Subcritical specific energy head
H_d	Water level in the reservoir
h	Dam height
I	Linear hydraulic head loss
K_P	Drag per unit volume

k	Turbulent kinetic energy
k_{air}	Air entrainment coefficient of proportionality
L_{II}	Typified USBR II stilling basin length
L_j	Hydraulic jump length
L_r	Hydraulic jump roller length
L_T	Turbulent length scale
n	Manning coefficient
P_d	Stabilising forces
P_k	Production of turbulent kinetic energy
P_s	Destabilising forces
p	Pressure
$\bar{p}$	Mean pressure value
p'	Pressure instant fluctuating component
Q	Discharge
q	Unit discharge
R^2	Coefficient of determination
R_H	Hydraulic radius
R_m	Richardson-Zaki coefficient multiplier
R_P	Average particle radius
R_z	Richardson-Zaki coefficient
Re_1	Inflow Reynolds number
S	Submergence factor
s_1	Spacing between chute blocks
s_2	Spacing between blocks in the end sill
St	Strouhal number
T	Return period
t	Time
U	Dimensionless velocity
U_{max}	Dimensionless maximum velocity
U_R	Magnitude of relative velocity
U_S	Dimensionless maximum backwards velocity
u	Velocity
u^*	Shear velocity
u^+	Dimensionless velocity for the wall function
u_∞	Horizontal component of the freestream velocity

u_1	Supercritical flow mean velocity
u_2	Subcritical flow mean velocity
u_i	Averaged flow velocity in a particular position
u_{max}	Maximum velocity
u_r	Relative velocity between phases
u_r'	Adjusted relative velocity between phases
u_S	Maximum backwards velocity
u_τ	Shear velocity for the wall function
w_1	Chute blocks width
w_2	Blocks width in the end sill
We_1	Inflow Weber number
X	Dimensionless coordinate in the longitudinal axis
x	Coordinate in the longitudinal axis
x_0	Hydraulic jump toe position
x_S	Distance between the hydraulic jump toe and the upstream face of the end sill
Y	Dimensionless flow depth
y^+	Wall coordinate
y_1	Supercritical flow depth
y_2	Subcritical flow depth
y_2^*	Bélanger subcritical flow depth
y_i	Flow depth in a particular position
Z	Dimensionless vertical coordinate
z	Vertical coordinate

Greek Symbols

α	Constant for the maximum void fraction trend
γ	Specific weight
γ_w	Water specific weight
δ	Height for the maximum velocity
δV	Volume of entrained air rate
ε	Turbulent kinetic energy dissipation rate
η	Hydraulic jump efficiency
θ	Spillway angle
λ	Ratio of blocked width to total basin width
μ	Dynamic viscosity
μ_t	Turbulent dynamic viscosity
ν	Kinematic viscosity
ν_a	Air kinematic viscosity
ν_w	Water kinematic viscosity
ξ	Normalised vertical position
ξ_*	Normalised vertical position for the boundary between regions
ξ_{C50}	Normalised vertical position for the void fraction value of 0.5
ξ_{C95}	Normalised vertical position for the void fraction value of 0.95
ξ_{Cmax}	Normalised vertical position for the maximum void fraction in the lower region
ρ	Density
ρ_a	Air density
ρ_m	Fluid mixture density
ρ_w	Water density
σ	Surface tension coefficient
σ_k	Parameter for the RNG $k-\varepsilon$ turbulence model
σ_ε	Parameter for the RNG $k-\varepsilon$ turbulence model
τ_0	Wall shear stress
ϕ	Variable whose accuracy is under assessment
ϕ_{ref}	Reference variable to assess the accuracy
ω	Specific dissipation rate of the turbulent kinetic energy

Abbreviations

ADV	Acoustic Doppler Velocimeter
ASME	American Society of Mechanical Engineers
CFD	Computational Fluid Dynamics
CHJ	Classical Hydraulic Jump
DES	Detached Eddy Simulation
DIP	Digital Image Processing
DNS	Direct Numerical Simulation
FFT	Fast Fourier Transform
FVM	Finite Volume Method
ICOLD	International Commission On Large Dams
LES	Large Eddy Simulation
LIDAR	Light Detection and Ranging
NTS	Spanish Technical and Safety Standards for Dams and Reservoirs
PSD	Power Spectrum Density
RANS	Reynolds Averaged Navier-Stokes
RNG	Renormalisation-Group
SAF	Saint Anthony Falls
SST	Shear Stress Transport
TUWien	Technische Universität Wien
USBR	United States Bureau of Reclamation
USCE	United States Corp of Engineers
UPV	Universitat Politècnica de València
VNIIG	Institute of Hydrotechnics Vedeneev
VOF	Volume OF Fluid

Chapter 1. Introduction

1.1. Background

The crucial role played by dams in civil engineering can only be understood due to its significant economic and social importance, which leads to high safety requirements, as a result of the critical consequences derived from a possible failure. This singularity, bound to the important growth in the number of dams built all around the world during the last decades, brings the importance of dam engineering into the spotlight [1], [2].

Nowadays, new considerations arise at a global scale, derived from climate change effects and new society demands in terms of security and flood protection. This situation leads to new scenarios, challenging the structural and hydraulic design of existing dams. The challenge hence posed must be understood as a global issue, and Spain is not an exception (Figure 1). The database form the International Commission On Large Dams (ICOLD) [3] places Spain as one of the top countries regarding the total number of dams, as well as for the dam per capita ratio. Furthermore, according to data from the Spanish Ministry for Ecological Transition, more than 80% of these dams were built before 1990, many of them under the design regulations established in 1967. New legal frameworks and considerations, gathered together in the Spanish Technical and Safety Standards for Dams and Reservoirs (NTS) [4], lead to requirements for existing structures that were not considered in their design phase. While most of the dams built in the Spanish territory only considered for their design the flood event associated to the 500 years return period (T), the requirements described in the NTS pose more restrictive scenarios.


(a)


(b)

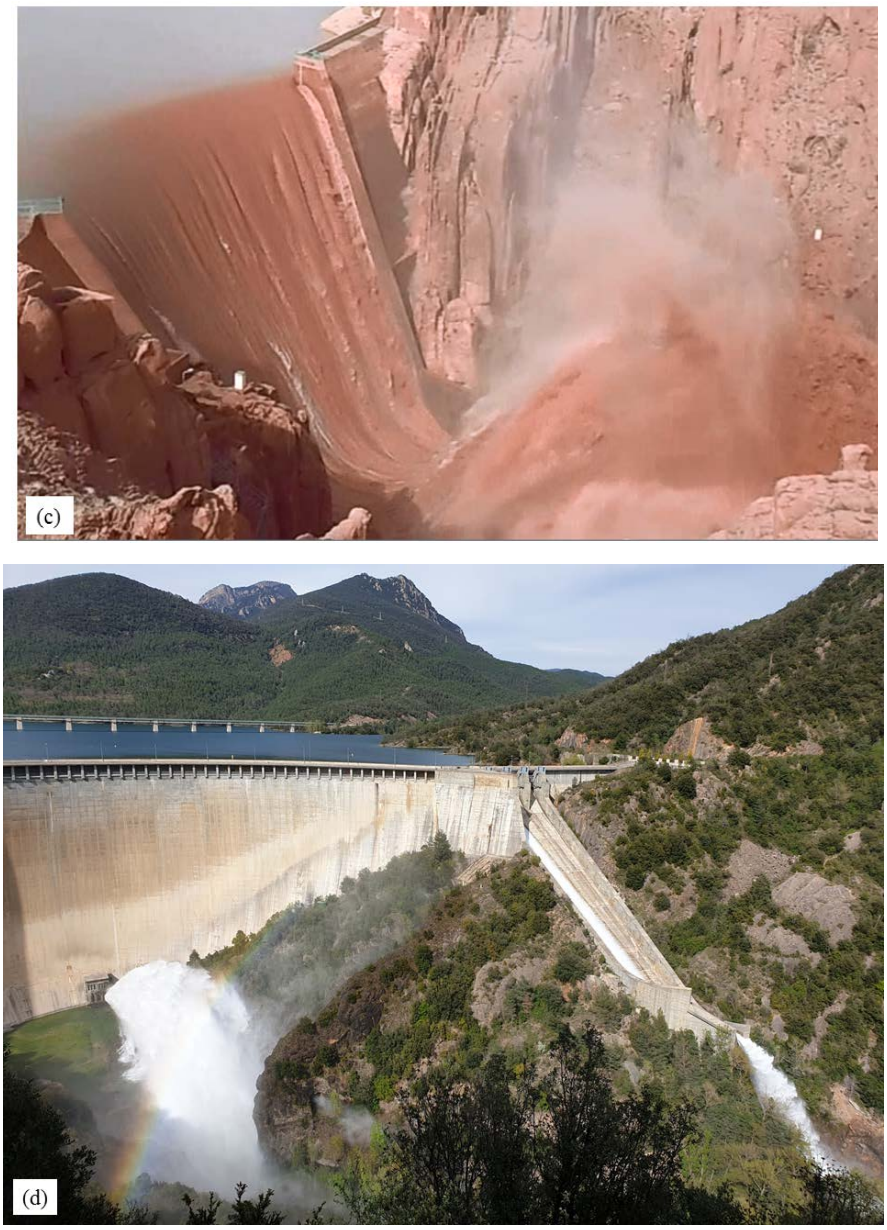

Figure 1. Discharge in large-dam spillways (courtesy of Dr. Gómez de Membrillera and Carlos Barbero): (a) Aguilar dam (Palencia, Spain), (b) Camporredondo dam (Palencia, Spain), (c) Brezina dam (El Bayadh, Algeria), (d) la Baells dam (Barcelona, Spain).

Thus, the first step to apply the new technical guidelines is to define the type of dam to be designed. The Spanish legal framework considers large dams those with height above 15 m or those that, with height between 10 a 15 m, have a reservoir capacity over 1 hm^3. Furthermore, dams are classified into three categories (A, B or C) according to the potential risk derived from the malfunctioning of the dam or a possible failure of the structure:

- Type A: Important affection to urban areas or essential services. Severe material or environmental damages.
- Type B: Affection to a reduced number of households. Important material or environmental damages.
- Type C: Moderate material or environmental damages.

Once the dam is classified into one of these three categories, different flood events must be considered for its design. On the one hand, the project flood event is the one that must be considered for the design of the spillways and the energy dissipation structures in large dams. On the other hand, the extreme flood event, understood as the largest event that the dam has to manage without overtopping, must be taken into account too. Table 1 shows the return periods associated to the described flood events that must be considered in the design phase, according to the NTS.

Table 1. Return period (in years) associated to the different flood events that must be considered for large dams design phase, according to the Spanish legislation [4].

Dam Type	Project Flood Event	Extreme Flood Event	
		Gravity or Arch Dam	Embankment Dam
A	1000	5000	10000
B	500	1000	5000
C	100	500	1000

The values displayed in Table 1 show that the return period considered in the design of a majority of the dams built in Spain underestimates the requirements stated in the new legal frameworks. Hence, the adaptation of existing dams means that these structures will need to successfully cope with larger discharges than those considered for their design.

When increasing the dam discharge capacity, the most challenging part from a technical and economical point of view is usually the energy dissipation structure [5].

The most extended energy dissipation structures in large dams are the stilling basins. In these structures a hydraulic jump is forced to occur [2], [6]. Consequently, energy is dissipated due to the hydraulic jump own nature and characteristics and the excess water coming from the dam is restituted to the river with the appropriate energy conditions. Despite being part of a dam, stilling basins can be considered as a hydraulic structure by themselves. According to Hager [2], stilling basins were developed in the 1930s, with significant progress during the 1960s. Stilling basins are not the only option to dissipate energy in dams, however, according to Murthy and Divatia [7], they are the most effective mechanism and also the safer from an erosive and cavitation perspective. In addition, there is a considerable amount of knowledge and experience developed for their use [2].

The design of these structures is very strict and must adjust to a precise discharge in order to ensure an optimal performance [6]. Hence, stilling basins show important limitations to perform under discharges out of the range considered for their design. Therefore, the adaptation of existing stilling basins must be carefully studied. This adaptation is necessarily bound to the knowledge of the hydraulic jump developed within these structures. The deep complexity of the hydraulic jump places the current knowledge far from a full understanding of the phenomenon [8]. In these terms, a thorough study of the hydraulic jump is crucial to improve the performance of stilling basins and to address their adaptation.

1.2. State-of-the-Art

The present research was developed with the aim of contributing to the application of hydraulic jumps for energy dissipation purposes in large dams. To do so, a complete characterisation of the classical hydraulic jump was made, as an unavoidable previous step to study hydraulic jumps in stilling basins. Then, particular cases of stilling basins were addressed in order to analyse its behaviour and try to improve their performance. In this process, the double physical and numerical modelling approach was the methodology used. Consequently, the bibliographic review presented in this section includes references strictly focused on the relevant aspects of the hydraulic jump modelling itself. Further sections of the document, introducing methodologies, numerical modelling routines, laboratory techniques and measuring devices will

conveniently introduce references to related previous research, and thus, its own state-of-the-art.

The hydraulic jump can be defined as the sudden transition from supercritical to subcritical regime in open-channel flows. This transition, from a supercritical regime with relatively high velocity and small flow depth to a subcritical regime, characterised by bigger depths and lower velocities, takes place through a rough and discontinuous increase in the free surface elevation. The phenomenon is characterised by its high complexity, with large turbulent fluctuations in velocity and pressure, intense air entrainment and significant energy dissipation [9]. As a basis for the hydraulic jump definition, it is important to introduce the concept of Classical Hydraulic Jump (CHJ). The CHJ is the hydraulic jump that occurs in a horizontal, rectangular, prismatic, smooth channel. This hydraulic jump has been widely studied, due to its relative simplicity when compared to hydraulic jumps occurring under different conditions. The vast knowledge hence developed is of paramount importance for energy dissipation applications in hydraulic engineering [2]. Figure 2 shows a sketch of a CHJ and its flow structure. A series of basic dimensions, such as the supercritical (y_1) and the subcritical (y_2) flow depths, the hydraulic jump roller length (L_r) and the hydraulic jump length (L_j), are also displayed in this figure.

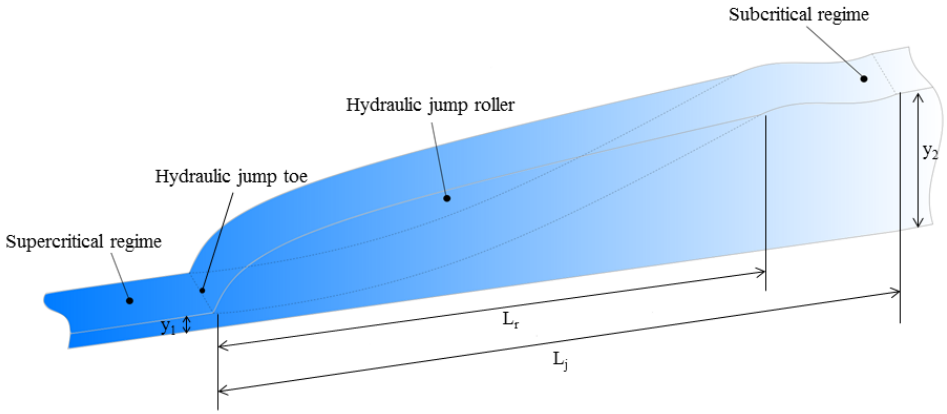

Figure 2. Classical Hydraulic Jump sketch with basic dimensions.

Figure 2, with the flow from left to right, shows the above mentioned discontinuous free surface profile of the hydraulic jump. The discontinuity point is known as the hydraulic jump toe or impingement point. The hydraulic jump roller is developed immediately downstream of the hydraulic jump toe. This roller region is characterised

by a turbulent flow with intense air entrainment. In addition, y_1 and y_2 , associated to the supercritical and to the subcritical flow regime respectively, are known as the conjugate or sequent flow depths.

According to Wang [9], the hydraulic jump is not a stationary phenomenon, due to a series of fluctuations existing in its characteristics, with different time and length scales. However, it can be treated as a steady phenomenon from a statistical point of view. With this perspective, it is possible to analyse time-averaged properties of the flow, such as the dimensions displayed in Figure 2.

Despite the chaotic nature of hydraulic jumps, they are frequently classified according to their approaching or inflow Froude number (Fr_1). This dimensionless number establishes a relationship between flow inertial and gravity forces:

$$Fr_i = \frac{u_i}{\sqrt{g y_i}} \tag{1}$$

where u_i is the depth-averaged velocity, g the gravity acceleration and y_i the water depth. According to Hager [2], hydraulic jumps are considered to be steady or stable for Fr_1 values ranging from 4.5 to 9.0. This range of inflow Froude numbers leads to a stable and compact appearance, with an optimal performance for energy dissipation purposes. Higher Fr_1 values produce unstable and choppy jumps, prone to flow detachment and bubble and spray formation, whereas lower Fr_1 values lead to undular jumps, characterised by lower efficiencies and formation of waves [10], [11].

The hydraulic jump phenomenon has plenty of applications, such as fluid mixing, flow reaeration, raising water levels for irrigation, reducing pumping heads or decreasing the uplift pressure for protection of hydraulic structures [9]. However, the energy dissipation associated to the hydraulic jump phenomenon is its most interesting feature for civil engineering applications [12]. This energy dissipating feature may be amplified by the use of structures with energy dissipation devices. In regards with the presence of these energy dissipation devices, different types of stilling basins can be distinguished [2]. On the one hand, in simple jump basins, the hydraulic jump takes place without any appurtenance obstructing the flow. On the other hand, in baffle basins, a series of energy dissipation devices are displayed to increase the turbulence and help to stabilise and shorten the hydraulic jump. This effect may reduce the costs of the stilling basin, but also, the existing appurtenances can lead to cavitation damages in the structure.

When choosing a particular type of stilling basin for a dam, many factors must be considered based on hydraulic, geological, operational and economic conditions. Many times, the particular conditions of the dam lead to an *ad hoc* design of the stilling basin. However, for many other cases, standardised or typified stilling basins can be considered. Some of the most extended standardised stilling basins are [2], [12]:

- The Saint Anthony Falls (SAF) stilling basin [13], characterised by the use of combined chute blocks at the entrance of the basin, baffles blocks and an end sill to reduce the size of the basin.
- The United States Bureau of Reclamation (USBR) stilling basins [6]. Based on experimental studies, ten different stilling basins were designed by the USBR. Each of these designs is intended for a particular scope of application. The present research has widely studied the USBR II stilling basin. This basin was designed for high dams, with large unit discharges and approaching velocities. Its design is characterised by the use of chute blocks and a dentated sill to reduce the length of the jump.
- The United States Corp of Engineers (USCE) stilling basin [2], which includes two rows of baffle blocks and an end sill.
- Bahvani-type stilling basin. This basin was described by Kuttiaammu and Rao [14] and is characterised by a depressed apron and the presence of T-shaped blocks.
- The Institute of Hydrotechnics Vedeneev (VNIIG, in Saint Petersburg, Russia) stilling basins. Four different designs of standardised stilling basin were developed by the Institute [15], [16]. The VNIIG type I is similar to the USBR I [6], hence involving a classical hydraulic jump. The remaining types present baffle blocks or sills but the available information on their performance is relatively short when compared to other standardised basins [17].

At this stage, it seems clear that the design, construction, and eventual adaptation of stilling basins to larger flow discharges, are all extremely challenging engineering goals. It is not only the consideration of multiple external factors, such as the budget, the geological or the environmental conditions, that adds complexity to the process. Besides, the previously mentioned nature of the hydraulic jump makes it difficult to completely predict its behaviour and therefore, a thorough study of each particular case is required. In order to tackle the hydraulic jump modelling with maximum rigour and reliability, a double modelling approach was considered in the present research. Hence

both, the CHJ and the hydraulic jumps taking place in stilling basins, were studied from a physical and numerical perspective.

The use of reduced scale physical models and the corresponding experimental campaigns constitutes the traditional approach to the study of the hydraulic jump and the design of large-dam stilling basins [5]. Despite the appearance of new modelling techniques, physical modelling remains indispensable for a rigorous study of complex flows such as the hydraulic jump, where the support of experimental data is crucial [12], [18], [19]. Furthermore, according to Hager [2], the design of stilling basins in large dams, or when the failure of the structure would mean considerable losses, should always be supported by a hydraulic physical model. Even for the previously mentioned typified stilling basins, despite their standardised design, the use of physical models must be considered as a useful tool, due to their obvious practical interest [5], [12].

Regarding the hydraulic jump physical modelling process, it is important to define more dimensionless numbers, apart from the Froude number. On the one hand, the Reynolds number, relating flow inertial and viscous forces, plays a crucial role when modelling flows at laboratory scale [20], [21]. In fact, this non-dimensional number affects significantly the validity of the extrapolation of laboratory results to large size prototype hydraulic structures, due to the possible occurrence of scale effects. Consequently, the inflow or approaching Reynolds number must be high enough in order to ensure model-prototype similarity [22], [23]:

$$Re_i = \frac{u_i y_i}{\nu} \tag{2}$$

where ν is the kinematic viscosity. On the other hand, the Weber number, proportional to the ratio of the inertial to surface tension forces, is defined as [24]:

$$We_i = \frac{\rho u_i^2 y_i}{\sigma} \tag{3}$$

where ρ is the fluid density and σ the surface tension coefficient. Heller [22] established a series of recommendations regarding these dimensionless numbers and other geometrical considerations. Among these guidelines, those affecting the phenomena modelled in the present research were considered. These recommendations, showed in Table 2, were proposed in order to avoid the appearance of significant scale effects in hydraulic engineering physical modelling.

Table 2. Considerations to avoid significant scale effects according to Heller [22].

Model	Affected Phenomenon	Criteria
Broad-crested weir	Discharge coefficient	Overfall height ≥ 0.07 m Still water depth ≥ 0.30 m
Hydraulic jump	Sequent depths ratio (y_2/y_1)	Re_1 > 100,000 for Fr_1 < 10 and $y_1/width$ < 0.1
Hydraulic jump	Void fraction distribution	Re_1 > 100,000
Spillway	Amount of air entrainment from aerator	$\sqrt{We_1}$ > 110

Despite the undeniable utility of hydraulic physical modelling some remarks can be made. A significant number of the available physical modelling investigations focus on the measurement of external macroscopic variables, although some of them use intrusive techniques to obtain more detailed experimental data sets [25], [26]. Furthermore, reduced scale physical models introduce some unavoidable scale effects, in spite of the research conducted to minimise their affection [22], [23]. These scale effects may influence some aspects of the flow such as the aeration [20]. Alternatively, numerical methods, and in particular Computational Fluid Dynamics (CFD) techniques, arise as advanced tools providing a detailed analysis of the flow at the prototype scale. This approach is gaining more and more importance in the modelling process of hydraulic structures, especially those where aeration needs to be considered [27]. Hence, CFD techniques have proved to constitute a useful approach to fill the gap in the modelling process of hydraulic jumps [25], [28], [29].

In spite of the multiple advantages of CFD techniques, they still present some limitations to accurately reproduce certain complex hydraulic phenomena [30]. These accuracy issues are particularly important for the numerical modelling process of the hydraulic jump. The fluctuating boundaries and the air-water flow involved in this phenomenon imply an increasing uncertainty in the use of CFD techniques [28]. In addition, they require a number of hypotheses and theoretical simplifications, and thus, calibration and validation using physical models remain indispensable [8], [30]. It is this complementary nature of numerical and experimental techniques that motivates the double modelling approach carried out in the present research (Figure 3).

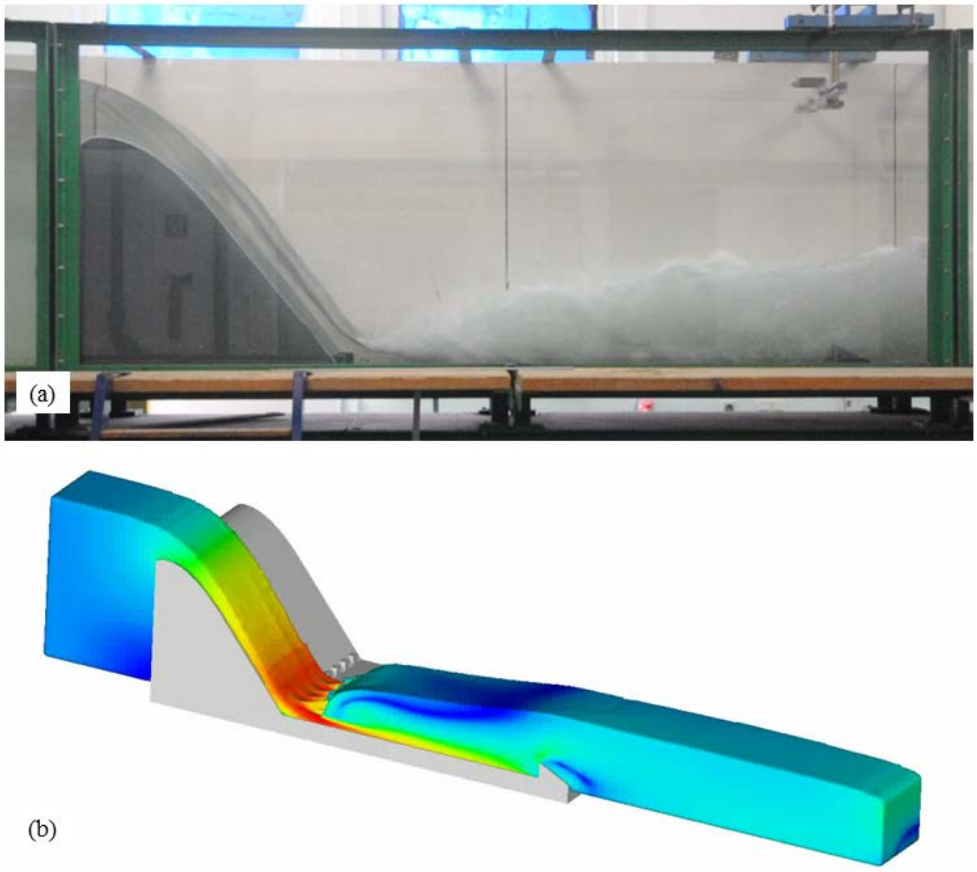

Figure 3. Double approach to the modelling of a typified USBR II stilling basin: (a) Reduced scale physical model in the Hydraulics Laboratory of the Institute of Hydraulic Engineering and Water Resources Management, at the Technische Universität Wien (TUWien, Austria), (b) Numerical CFD model developed using the commercial code FLOW-3D®.

The hydraulic jump phenomenon has been widely studied throughout the history. The research dedicated to this phenomenon has been not only devoted to characterise its nature and understand its internal structure, but also to take advantage of its potential engineering applications. The complexity and interest of the phenomenon is bound to a prolific research that has not ceased to increase in the recent years. Hence, an important part of the investigation regarding hydraulic jumps is out of the scope of the present research. However, there are a series of key works including bibliographic reviews on the topic, which can help to complete and improve this state-of-the-art.

In these terms, Hager [2] conducted a deep review addressing both, the classical hydraulic jump and the performance of stilling basins. For the CHJ, Hager studied a series of basic dimensions such as the sequent depths or the roller and hydraulic jump lengths, together with the velocity and pressure distributions and the air entrainment process. Actually, this author presented analytical expressions for the maximum forward velocity decay and the maximum backwards velocities, together with a theoretical vertical velocity profile for the diffusion portion in the hydraulic jump roller region that were used for comparison purposes in sections 4.4.1 and 5.4.1. Furthermore, Hager [2] proposed an expression for the hydraulic jump efficiency that was included in the analysis conducted in sections 4.2 and 5.2. Regarding the stilling basins study, Hager investigated a series of energy dissipation devices and collected the characteristics of an important number of standardised stilling basins.

Moreover, the research conducted by Wang [9] included an extended bibliographic review of historical hydraulic jump studies, complemented with a review on numerical modelling and recent physical modelling studies, paying special attention to the experimental instrumentation. In addition, Chanson [31] developed a monograph on energy dissipation in hydraulic structures, covering a wide range of strategies. Finally, Valero, Viti and Gualtieri conducted a recent review on the modelling process of the hydraulic jump, with a first part collecting experimental data and references [12] and a second part devoted to create a state-of-the-art of the hydraulic jump numerical simulations [28]. From this review conducted by Valero et al. [12], different techniques to address the hydraulic jump length were discussed in section 4.4.2.

Once a series of essential reviews have been highlighted, the bibliographic review presented herein is focused both, on the classical hydraulic jump and on the stilling basins. The physical or numerical perspective of the studies reviewed was considered and indicated. It is also important to remark that the complexity of the hydraulic jump lies in the interaction between the physical processes involved in the phenomenon. Therefore, although a chronological order, organised according to a particular hydraulic jump characteristic was intended for the review, some of the studies referred could have appeared in a different order.

1.2.1. Classical Hydraulic Jump Review

Several authors agree that the first descriptions of the hydraulic jump phenomenon date back to Leonardo da Vinci in the 16th century [2], [9]. Hundreds of years later, the first

experimental and analytical studies were undertaken by Bidone [32] and Bélanger [33] during the 19th century, focusing on basic hydraulic jump dimensions. Hence, Bidone approached the ratio of sequent depths and the hydraulic jump length for relatively low Froude numbers, whereas Bélanger successfully predicted the sequent depths ratio by using the flow momentum equation. This theoretical solution proposed by Bélanger is used up to date. In fact, this expression was considered in the analysis developed in section 5.1.1. Further experimental studies were reported by Darcy and Bazin [34], regarding undular hydraulic jumps. In addition, other studies with a theoretical perspective can be highlighted in this century, such as the one by Boussinesq [35].

In the 20th century, following the line of the study of basic CHJ dimensions, Safranez [36] conducted a systematic experimental study, including bibliographic data and a deep investigation on the extent of the hydraulic jump roller. This work by Safranez also included an insight to energy dissipation in the hydraulic jump phenomenon, attributing this energy dissipation feature to the rotational movement in the roller region. Bakhmeteff contributed to these first steps towards the development of the hydraulic jump knowledge with his discussion on open channel flows [37]. The work conducted by Rouse [38] on the use of dimensionless numbers was also of paramount importance. Among these dimensionless parameters, Rouse addressed the Froude number, which is of particular relevance for hydraulic jumps, as explained before. Furthermore, Bakhmeteff and Matzke [39] published their experimental results regarding conjugate depths and hydraulic jump length, and presented dimensionless free surface profiles too. This dimensionless free surface profile was used to contrast the results of this research developed in sections 4.1.2 and 5.1.2.

Years later, in the second part of the 20th century, Rouse et al. [40] first approached the turbulence characteristics of the hydraulic jump through hot wire measurements of turbulence in an air flow model of a hydraulic jump for Froude numbers of 2, 4, and 6. Moreover, Rajaratnam [41] focused on the internal flow features of the phenomenon with the wall jet analogy. In this work, Rajaratnam carried out extensive measures regarding the pressure field, velocity distribution, and the boundary shear stress in the jump, for nine inflow Froude numbers ranging from 2.68 to 9.78. Among the remarkable results of this study, a more accurate form of the momentum equation for the jump was developed. Schröder [42] and Resch and Leutheusser [43] also made important contributions to this first approach to the turbulent structure of the hydraulic jump, whereas Abdul Khader and Elango [44] undertook an statistical characterisation

of the pressure field beneath a hydraulic jump, including the analysis of pressure fluctuations. The procedure to obtain pressure fluctuations by Abdul Khader and Elango was followed in this research (section 4.5). In addition, the results by these authors were used to compare the trend followed by the fluctuations along the hydraulic jump longitudinal axis and to contrast the location for the peak pressure fluctuations.

Parallel to the generally experimental and observational approach, the first computational models on hydraulic jumps were developed in the decade of the 1970s by Rouse [45] and Narayanan [46]. In this line, McCorquodale and Khalifa [47] developed a mathematical model in the early 1980s to study the internal flow in hydraulic jumps. This model used a Gaussian velocity distribution in the mixing zone and the power law in the inner layer. Focusing on the results, the model was able to provide a good prediction for the hydraulic jump length, roller length, velocity distribution, free surface profile and pressure at the bed. The vertical velocity profile presented by McCorquodale and Khalifa completely covers the hydraulic jump flow depth in the roller region, from the channel streambed until the free surface, and was used to adjust the velocity results obtained in the models here presented (section 4.4.1).

During the last decades, numerous experimental and numerical studies were developed. These studies addressed not only those properties of the hydraulic jump already treated, such as the basic dimensions, but also new features like the aeration or the inflow properties affection. Thus, Hager, Bremen and Kawagoshi deepened in the study of the hydraulic jump sequent depths and roller length, using experimental data [23], [48]. On the one hand, Hager and Bremen [23] accounted for the effect of wall friction on the sequent depths ratio of CHJ, concluding that it is not only influenced by the inflow Froude number, but also by the inflow Reynolds number, and the inflow aspect ratio. Hence, their expression to obtain the sequent depths ratio is based on Bélanger's equation [33], and was included in the analyses developed in sections 4.1.1 and 5.1.1. On the other hand, Hager et al. [48], provided a precise definition of the CHJ roller length, distinguishing between the developed and the non-developed roller flow. These authors established their own theoretical expression for the determination of the hydraulic jump roller length, based on an extensive review regarding previous studies. The expression by Hager et al. [48] was compared in sections 4.3 and 5.3 with results coming from the models developed in this research. Furthermore, Toso and Bowers [49] and Mossa [50] studied the relationship between turbulence structure and pressure and velocity fluctuations in hydraulic jumps, also on the basis of experimental

observations. Toso and Bowers focused on extreme pressures, whereas Mossa experimented with several hydraulic jumps to investigate their oscillating characteristics and cyclic mechanisms. The average relative pressures values collected by Toso and Bowers along the hydraulic jump longitudinal axis were included in the analysis conducted in section 4.5.

Regarding the aeration of the hydraulic jump, a series of relevant studies can be highlighted from the beginning of the 21st century. Chanson and Brattberg [51] initiated the systematic experimental study of air-water flow properties in the hydraulic jump. These authors presented distributions of air concentration, mean air–water velocity and bubble frequency, concluding with the existence of an advective diffusion of air in the shear layer. This experimental work was followed by Murzyn et al. [52] to obtain measurements of void fractions, bubble frequencies and bubbles sizes in hydraulic jumps, using an optical fibre probe. Murzyn et al. covered a range of inflow Froude numbers from 2.0 to 4.8. They found that across the lower part of the flow, void fractions follow a Gaussian distribution whereas for the upper region, the void fraction follows the form of an error function. The analytical expression and normalisation process presented by Murzyn et al. [52] were adapted and followed for the void fraction distribution analysis presented in section 5.6. In this same section, data from these same authors and from Chanson and Brattberg [51] was used for comparison purposes.

Gualtieri and Chanson [53] conducted an experimental study on the effect of the inflow Froude number on air entrainment in the hydraulic jump. Hence, they recorded data covering Froude numbers from 5.2 to 14.3 demonstrating that, at a fixed distance from the jump toe, the maximum void fraction increases with the increasing inflow Froude number. They also presented an empirical correlation between the upper boundary of the air diffusion layer and the distance from the impingement point. These same authors complemented their research with a study on similitude and scale effects of the air entrainment process in hydraulic jumps [21]. Results from this study were included in the frequency analysis conducted in section 4.6. The influence of the inflow Froude number on the air entrainment characteristics of the hydraulic jump was also studied by Witt et al. [54], using CFD techniques. In this study, three different Froude numbers were tested to record velocity profiles, average void fractions and mean bubble diameters. Xiang et al. [55] also used numerical modelling techniques to study bubble entrainment and dispersion in hydraulic jumps.

In regards with the turbulence, as the most remarkable feature of the hydraulic jump nature, Wang and Chanson conducted experimental studies to quantify the fluctuating characteristics of the phenomenon for a wide range of Froude numbers [8]. Hence, they tested Froude numbers from 3.8 to 8.5 finding self-similarity for the time-averaged free surface profile and both, fast and slow fluctuations for the longitudinal movements of the jump. The dimensionless free surface profile presented by these authors was considered for the analysis in sections 4.1.2 and 5.1.2. Wang and Chanson [8] also established an expression to obtain the hydraulic jump roller length, which was employed in sections 4.3 and 5.3. These same authors also used the physical modelling support to discuss the relationship between the rate of air entrainment and turbulent fluctuations, for a wide range of Froude numbers (from 3.8 to 10.0) [19]. At this stage, it is important to remark that large-scale turbulence is found inside the roller and also at the hydraulic jump free surface, but also microscopic turbulent fluctuations take place within the body of the hydraulic jump. Therefore, information regarding length and time scales of the turbulent structures is crucial. Wang and Murzyn [56] investigated these turbulent scales for hydraulic jumps on an experimental basis. Their study covered the length and time scales of turbulent flow structures in bubbly flow, on the free surface and at the impingement point. They found that the large turbulent scales are related to the unsteady motion of the flow in the upper part of the roller, while the high-frequency velocity turbulence dominates in the lower part of the roller. The hydraulic jump turbulence characteristics were also studied through a CFD approach by Jesudhas et al. [57]. For this research, an inflow Froude number of 8.5 was considered to resolve the internal turbulent structure of the CHJ.

Based on the advances accomplished in the first years of the 21st century regarding turbulence and aeration, a series of hydraulic jump characteristics were reviewed. Chachereau and Chanson [58] and Zhang et al. [26] physically investigated the free surface fluctuations. On the one hand, all of these authors focused on the free-surface profile. Chachereau and Chanson worked with Froude numbers from 2.4 to 5.1 to define the shape of the mean free surface profile as well as the turbulent fluctuation profiles, finding some characteristic frequencies for these fluctuations and their length and time scale. In addition, Zhang et al. highlighted the fluctuating nature of the impingement perimeter in terms of both longitudinal and transverse locations. On the other hand, Wang and Chanson [8] analysed the position of the jump toe and its fast and slow fluctuations. The inflow conditions, and particularly the inflow Froude number, were paid special attention in the research of both, the free surface profile and the jump toe position. Furthermore, Montano et al. applied new experimental

techniques, based on light detection and ranging (LIDAR) technology, to measure the free surface characteristics of the jump, focusing on both, free surface fluctuations and jump toe oscillations [59], [60]. These authors found that jump toe oscillations increased for increasing Froude numbers. They also obtained continuous free surface time and length scales along the hydraulic jumps. They found that the largest free surface scales were observed close to the jump toe, linked with longitudinal oscillations of the hydraulic jumps, and that the dimensionless free surface scales increased with the Froude number. The basis established by Montano et al. was used to apply this innovative technique in the presented experimental campaign (section 3.2.2). Bayón et al. [29] also studied the free surface profile of a CHJ, in this case using a numerical modelling approach. These same authors also analysed the averaged velocity field as well as the maximum velocity decay and the maximum backwards velocities in the hydraulic jump roller. Several contribution by Bayón et al. [29], such as the benchmarking between different CFD codes (section 2) or the use of Digital Image Processing techniques (section 3.2.1) were employed in this research. Velocity distributions within the hydraulic jump for a range of different Froude numbers were also measured by Cheng et al. [61] using nonintrusive Particle Image Velocimetry (PIV) techniques. These authors also addressed the problem with a numerical model, finding a good agreement not only with their experimental measurements, but also with bibliographic data.

Despite a majority of the works previously referred constitute an experimental approach to the study of the classical hydraulic jump, CFD techniques have been crucial to investigate this phenomenon, especially from the beginning of the 21st century. Hence, Caisley et al. [62] successfully modelled a hydraulic jump in a canoe chute using the commercial CFD code FLOW-3D® in 1999. Years later, Gonzalez and Bombardelli [63] used numerical models to characterise the mean flow, turbulence and aeration in hydraulic jumps. These authors obtained a satisfactory agreement with experimental data. In the recent years, Romagnoli et al. [64] and Bayón and López-Jiménez [25] modelled a hydraulic jump, using the free source CFD code OpenFOAM. These models approached a series of CHJ variables such as the sequent depths ratio, the hydraulic jump efficiency, the roller length and the free surface profile, obtaining good results in terms of accuracy when compared with previous studies. Witt et al. [54] also used this open source code to study the aeration in the hydraulic jump. In addition, Bayon et al. [29] used both of the previously mentioned CFD codes, namely FLOW-

3D® and OpenFOAM, to make a detailed characterisation of a classical hydraulic jump.

Apart from the computational code employed, the research on hydraulic jumps has been undertaken under different CFD approaches in the recent years. Thus, Ma et al. [65] used both, a Reynolds-Averaged Navier-Stokes equations (RANS) model and a Detached Eddy Simulation (DES) model to simulate a hydraulic jump. Both methods were capable to provide the void fraction profiles in the lower shear layer region, which contains the air bubbles entrained at the jump toe of the hydraulic jump. In contrast, the authors found that in the upper roller region behind the toe, the averaged results of the DES model gave accurate predictions whereas the RANS model did not. Langhi and Hosoda [66] modelled a hydraulic jump with an unsteady RANS approach, obtaining results for the free surface profile, velocity distributions and turbulence. In addition, Lubin et al. conducted a numerical simulation of turbulence and aeration in a hydraulic jump under a Large Eddy Simulation (LES) approach [67], whereas Mortazavi et al. [68] achieved the Direct Numerical Simulation (DNS) of a low Froude and Reynolds number hydraulic jump. Mortazavi et al. compared their results to experimental data of void fraction and interfacial scales, finding reasonable agreement despite a Reynolds number mismatch. Moreover, Zhao et al. [69] used two different turbulence models to study the mean flow motions in a hydraulic jump with a RANS approach. In these terms, Bayon et al. [25], [70] tested three different turbulence models under a RANS approach to simulate a classical hydraulic jump comparing their performance through the analysis of several variables such as the sequent depths ratio, the hydraulic jump efficiency or the free surface profile. The conclusions derived from the bibliographic review of the presented CFD modelling approaches, were considered in the setup process of the numerical models developed for this research (section 2).

1.2.2. Stilling Basins Review

According to Valero et al. [12], the research on stilling basin hydraulic jumps has not been as prolific as for the classical hydraulic jump, despite the undeniable practical interest of this energy dissipation structures. Nevertheless, some relevant studies can be highlighted.

In the beginning of the 20th century, Riegel and Beebe [71] conducted an experimental study to assess the performance of different stilling basin configurations and energy dissipation devices, involving sloping bottoms, blocks and some expansion angle.

Important contributions were also made by Rehbock [72], who introduced the design of the dentated sill. However, the generalised study of the hydraulic jump in stilling basins took place in the middle of the century, with the development of the previously mentioned standardised stilling basins. A comparison of several of these standardised designs conducted by Chitale [73] concluded that the USBR typified basins were highly efficient when compared to other designs. This research used experimental data to establish a relationship between the length and the height of the hydraulic jump. Focusing on these designs proposed by the USBR, Peterka made significant contributions [6], including guidelines and recommendations for the design of the stilling basins. These guidelines were followed in the design of the research case study (section 3.1.2). The design safety factors considered by Peterka in his monograph lead to a conservative design of the typified USBR stilling basins. Hence, this work is particularly useful for preliminary or rough estimates of basin and energy dissipation devices sizes and dimensions.

In the last decades of the century, Lopardo et al. [74] investigated the pressure fluctuations in a stilling basin through field studies at prototype scale. As reported by Wang [9], the work by Lopardo et al. addressed the mean square values for pressure fluctuations, pressure amplitudes, peak frequencies and cavitation tendencies. In these terms, the research by Toso and Bowers [49], mentioned in the classical hydraulic jump review, also accounted for hydraulic jumps in stilling basins. Hence, these authors provided information on extreme pressures for hydraulic jumps in stilling basins, for a wide range of Froude numbers and for different basin configurations, including chute blocks, intermediate blocks and end sills. This information was used to contrast the results presented in section 5.5. In addition, Rahmeyer [75] proposed alternate designs for the USBR II stilling basin, based on two physical modelling studies. In particular, the research by Rahmeyer discussed several alternate designs to replace the full height sidewalls of the basin. Ohtsu et al. [76] conducted an experimental study to determine the drag force on stilling basin sills. On the basis of their observations, these authors proposed an expression to obtain the drag coefficient, which was used to contrast the results of this research (section 5.5). Furthermore, Hager and Li [77] analysed the effect of continuous transverse sills on the hydraulic jump in a rectangular basin, paying special attention to flow patterns.

In the 21st century, the study of the hydraulic jump developed in stilling basins continued. Carvalho et al. [78] analysed the formation of a hydraulic jump in a stilling

basin with a continuous square baffle, using both, a physical and a numerical modelling approach. In this study, conducted for a Froude number of 6, the authors found a satisfactory agreement for velocity and pressure values, not only between the numerical and the physical model, but also in the comparison with formulae available in the literature. Wang et al. [79] developed the model of a stilling basin hydraulic jump using the CFD code FLOW-3D® and compared the results with experimental data. This comparison was focused on flow velocity distributions and the water free surface profile as well as the energy dissipation ratio. Tajabadi et al. [80] also employed numerical techniques to model the standardised USBR types I, II and III stilling basins, with validation coming from physical modelling data. They analysed hydrodynamic parameters such as pressure, velocity, vorticity and turbulence in the three typified basins. The authors found a better performance of the Type II basin when compared to the others, regarding energy dissipation purposes. This results, together with the research by Chitale [73], were considered in the selection of the typified USBR II stilling basin case study. Apart from this, Valero et al. [81] investigated the energy dissipation in a USBR type III stilling basin using experimental data and CFD techniques, They tested Froude numbers ranging from 3.1 to 9.5 and different turbulence models for the numerical modelling approach. In addition, Wu et al. [82] developed an experimental campaign to study the inflow conditions and their affection to the air entrainment in a hydraulic jump aeration basin. These authors found that the air concentration in the hydraulic jump is function of the dimensionless discharge as well as the length and the end sill height of the stilling basin.

The present research approached the study of the typified USBR II stilling basin. This structure has proved its efficiency for energy dissipation purposes when compared to other designs [73], [80]. In addition, there is an important knowledge built on its performance as its use is widely spread all around the world [5]. Apart from the already mentioned research by Rahmeyer and Tajabadi et al., Padulano et al. [83] conducted an experimental campaign to study the behaviour of the USBR II basin under different hydraulic conditions. These authors covered a wide range of Froude numbers to study hydraulic jump features such as the sequent depths ratio, the energy dissipation efficiency or the pressure regime. All of these results were included in the analysis presented in sections 5.1.1, 5.2 and 5.5. In addition, Fecarotta et al. [84] studied the affection of the energy dissipation devices on the pressure fluctuations, also using a USBR II basin physical model. The results by these authors were used in section 5.5 to contrast the presented models. Moreover, a series of works directly related with the

present research, were carried out to analyse the flow developed in this basin, from a physical and a numerical perspective [5], [85].

The state-of-the-art here presented shows that the hydraulic jump phenomenon has been widely studied. However, there are multiple physical processes involved in the phenomenon, resulting in an important number of features. Therefore, the presented review also reveals the difficulty to perform a complete and detailed analysis of the hydraulic jump, gathering together crucial characteristics of the phenomenon such as the hydraulic jump shape, velocity and pressure fields, and void fraction distribution. In addition, the numerical and experimental contrast of the obtained results often remains limited due to the wide range of existing methodologies. It is the humble intention of this research to develop a complete and detailed study of the hydraulic jump, approaching the phenomenon on the basis of a wide variety of numerical and experimental techniques. The efforts devoted to perform this detailed study become essential in regards with the complexity of the phenomenon, which lies in the interaction between the physical processes involved. Consequently, the present research aims at enhancing the knowledge of the hydraulic jump by studying together the most relevant features involved in the phenomenon, with the support of varied methodology and an extended bibliographic review to provide contrast and reliability.

The global vision of the hydraulic jump phenomenon achieved in the present research can be considered as an important advantage regarding the more specific studies found in the bibliography. As stated before, the interaction between the multiple physical processes involved brings the importance to the joint analysis of different features and characteristics, under one unique research. In addition, the deep analysis of the typified USBR II stilling basin constitutes one of the main novelties of this research. The use of CFD techniques and innovative instrumentation in experimental campaigns shed light on the performance of this energy dissipation structure. As the research on these typified stilling basins has been relatively limited in spite of their undeniable practical interest, the results here presented constitute a step forward to enhance the knowledge on these structures. In addition, these results help to establish an extended data base for comparison purposes regarding future research on the topic.

1.3. Motivation

The background situation and the state-of-the-art previously presented place the current knowledge on the hydraulic jump far from a full understanding of the phenomenon [9], despite the undeniable advances achieved during the last decades [12], [28]. In these terms, it is crucial to gain a better understanding of the hydraulic jump, not only to learn about the physical nature of the phenomenon itself, but also because of its valuable engineering applications. Hence, energy dissipation in large dams can be considered as one of the main applications of hydraulic jumps and, therefore, the performance of stilling basins must be placed in the spotlight of hydraulic engineering research. However, and despite a series of remarkable contributions [2], [6], the works devoted to the study of the hydraulic jump taking place in stilling basins are not as numerous as the importance of the issue would suggest [12].

Nowadays, the interest on improving the performance of large-dam stilling basins is constantly growing, as a result of the current situation and society demands. Climate change adaptation and increasing security requirements are reflected in the new legal frameworks concerning hydraulic structures design [4]. Consequently, a large number of existing dams must deal with larger discharges than those considered in their original design. The adaptation needed by these dams is particularly challenging for the energy dissipation structures both, from a technical and an economic point of view [5], [17]. It is under these circumstances that the research devoted to the study of the hydraulic jump and its performance in stilling basins becomes fundamental.

The presented situation constitutes the motivation that guided this research. In order to address the study of the hydraulic jump and its application in large-dam stilling basins, the complexity and magnitude of the matter must be considered. Hence, the present research started with the characterisation of a series of structural properties in a classical hydraulic jump, with similar characteristics to those used for energy dissipation purposes (Figure 4). This first step intended to shed light on the characteristics of such phenomenon and to establish a source of comparison for those other hydraulic jumps developed in stilling basins.

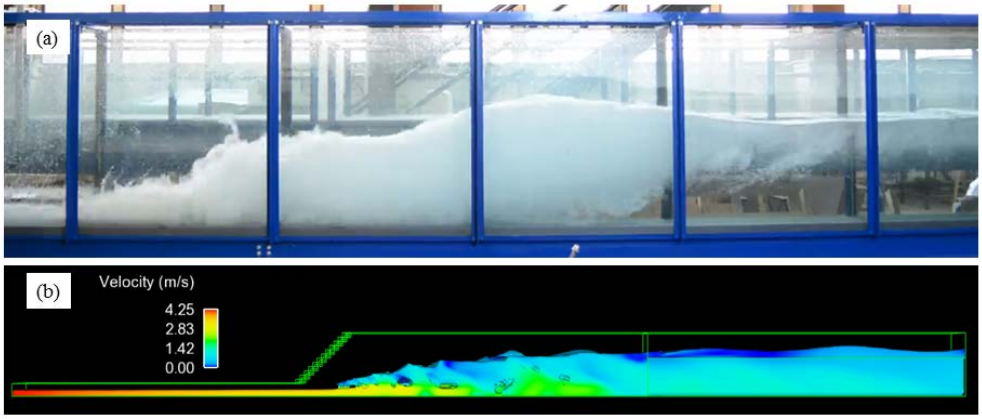

Figure 4. Double approach to the modelling of a classical hydraulic jump: (a) Physical model in the Hydraulics Laboratory of the Department of Hydraulic Engineering and Environment at the Universitat Politècnica de València (UPV, Spain), (b) Numerical CFD model developed using the commercial code FLOW-3D®.

Once the classical hydraulic jump was characterised, the research approached the practical use of the phenomenon. Among the numerous existing stilling basins, not only standardised but also *ad hoc* designs, the typified USBR II stilling basin was chosen as a case study (Figure 3 and Figure 5). This energy dissipation structure was considered since it has proven its efficiency when compared to others [73], [80] and has been widely used all around the world [5]. The study of the hydraulic jump in this stilling basin allowed gathering information on its performance. This information can be used to propose alternate designs or modifications. Hence, an improved design could be used to achieve the adaptation of the structure to more demanding requirements.

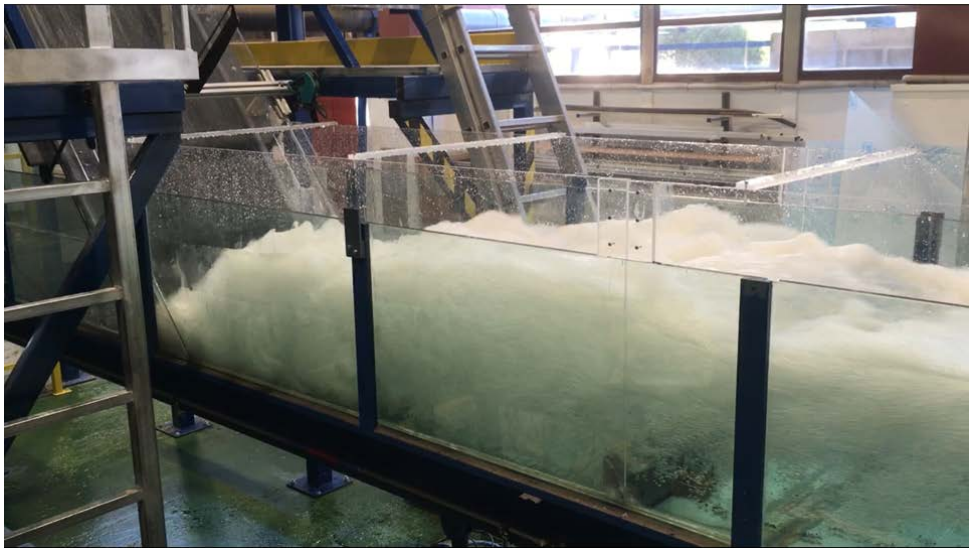

Figure 5. Physical model of a typified USBR II stilling basin in the Hydraulics Laboratory of the Department of Hydraulic Engineering and Environment at the Universitat Politècnica de València (UPV, Spain).

To carry out the presented research, a methodology involving a double modelling approach was developed. Thus, both, the classical hydraulic jump and the USBR II case study were simulated employing physical models and CFD techniques. The value of this double modelling perspective lies in the complementary character of physical and numerical modelling. In spite of its undeniable utility, reduced scale physical modelling presents some limitations such as the appearance of scale effects or the use of intrusive instrumentations for collecting data [9], [12], [22]. CFD modelling arises then as an excellent tool that can partially solve these issues. However, these computational techniques still present some difficulties to model complex hydraulic phenomena [28], [30]. Moreover, calibration and validation of numerical models remains necessary which in turn, makes the role of physical modelling essential [9], [12]. In these terms, the methodology involved the contrast of the results coming from the numerical and the physical models developed. Apart from this contrast, the work was improved through an extensive literature review. This review allowed using theoretical expressions and experimental data coming from other authors to complete the research.

1.4. Aim and Objectives

Given the aforementioned situation, the present research aims at contributing to the general knowledge of the hydraulic jump phenomenon and its application for energy dissipation purposes in large-dam stilling basins. This summarises the final goal of the works presented herein, which could be further developed through the following objectives:

- Bibliographic review to create a state-of-the-art of the hydraulic jump study and a source of comparison with experimental data and theoretical expressions.
- Development of a methodology to model hydraulic engineering phenomena through a double physical and numerical approach.
- Characterisation of the classical hydraulic jump through the double modelling approach developed.
- Case study: analysis of the typified USBR II stilling basin through the double modelling approach developed.

The fulfilment of the detailed objectives by the present research led to a series of remarkable contributions. Firstly, the bibliographic review conducted and the development of the double modelling approach established a straightforward methodology, useful for the analysis of a wide variety of hydraulic engineering problems. Moreover, the use of different CFD codes and experimental instrumentation, including innovative techniques, together with the multiple features considered led to a global analysis of the hydraulic jump. This extensive approach to the study of the phenomenon can be considered as an advantage regarding previous research more focused on particular characteristics or methodologies. Furthermore, the exhaustive analysis of the typified USBR II stilling basin carried out constituted one of the main novelties presented in this work. Despite the practical interest of the hydraulic jump developed in this energy dissipation structure, relatively little bibliographic information can be found about its particular characteristics. The results presented in this research led to some interesting conclusions regarding the influence of the energy dissipation devices on the flow. Besides, they constituted an important step forward to create an extensive data base for the study of the flow in stilling basins. Finally, the conclusions achieved have an undeniable interest for real-life engineering applications. The

characterisation of the hydraulic jump and the performance of the analysed stilling basin provided advantageous information to define new guidelines and recommendations for the design of energy dissipation structures and their adaptation to more demanding scenarios.

Chapter 2. Numerical Modelling

The three-dimensional numerical model of both, a Classical Hydraulic Jump (CHJ) and a hydraulic jump in a typified USBR II stilling basin were carried out. To do so, the version 11 of FLOW-3D®, a commercial software package developed by Flow Science, Inc. [86], was used. FLOW-3D® is based on the Finite Volume Method (FVM) [87] for the resolution of the flow governing equations. In addition, the code works with a number of different methods to model the free surface depending on the case, all of them derived from the Volume Of Fluid (VOF) as originally presented by Hirt and Nichols [88]. FLOW-3D® has been widely used in hydraulic engineering applications, achieving successful results since its release [5], [89]–[92].

This chapter is hence devoted to an in-depth explanation on how the different physical characteristics of the simulated phenomena were implemented in the numerical models specifically created with FLOW-3D®. Nevertheless, it is important to highlight that FLOW-3D® was not the only CFD code employed in the research. The numerical simulation of the CHJ was also approached using the free, open source software OpenFOAM version 6, in collaboration with the Hydraulics Laboratory of the Department of Hydraulic Engineering and Environment at the Universitat Politècnica de València (UPV, Spain) [70]. In particular, Dr. Bayón developed the CHJ numerical model using OpenFOAM. This tool constitutes a CFD open platform, which contains a number of C++ libraries and applications to achieve the numerical resolution of continuum mechanics problems [93]. OpenFOAM has also proven its efficiency to successfully model hydraulic engineering problems [25], [94], [95]. The opportunity of comparing the performance of different CFD codes was taken following the lines of previous studies [29]. According to Viti et al. [28] and Blocken and Gualtieri [30], the large application of benchmarking among different CFD techniques and methods is strongly recommended to approach environmental flows.

2.1. Flow Equations and General Settings

FLOW-3D® bases its results on the resolution of the flow governing equations, namely the continuity equation and the Navier–Stokes equations (Eqs. 4 and 5) which describe

the motion of an incompressible fluid in their general form. Due to the characteristics of the analysed flows, the Navier–Stokes equations for incompressible fluids were employed. According to Bayón et al. [29], this assumption can generally be done for flows with a Mach number under 0.3. It is important to remark that for the numerical resolution of the equations, FLOW-3D® uses the Finite Volume Method [87], in order to discretise the conservation laws in the case study spatial domain.

$$\nabla \overline{u} = 0 \tag{4}$$

$$\frac{\partial \overline{u}}{\partial t} + (\overline{u} \cdot \nabla)\overline{u} = -\frac{1}{\rho}\nabla p + \nabla \cdot (\nu \nabla \overline{u}) + \overline{f_b} \tag{5}$$

where u is the velocity, t is the time, ρ is the fluid density, p the pressure, ν the fluid kinematic viscosity and f_b accounts for the body forces (i.e., gravity and surface tension).

Regarding the time discretisation, the time-step size was automatically adjusted by the code, using a Courant-type stability criterion to improve model efficiency with a reduction of computational times and to minimise numerical divergence risk [86]. The Courant number is a dimensionless parameter that can be calculated as:

$$Cr = \frac{u \Delta t}{dx} \tag{6}$$

where u is the velocity of the flow in the cell, Δt is the time-step size and dx is the cell size.

2.2. Approaches to the Resolution of the Navier-Stokes Equations

The Direct Numerical Simulation (DNS) approach to the flow governing equations seeks for a resolution of all the essential turbulence scales. The results hence achieved constitute an accurate three-dimensional time-dependent solution of the equations [28]. However, this approach requires not only extremely short time-steps, but also a fine enough mesh. Consequently, the DNS approach is rather limited due to the available computer memory and processing time resources, and therefore, it is not a practical approach in a majority of hydraulic engineering applications.

Thus, the Reynolds Averaging of the Navier-Stokes equations (RANS) arises as the most widespread approach for engineering purposes [5], [28]. The RANS method constitutes a statistical approach to the equations through the time-averaging of velocity and pressure. Consequently, the instantaneous values of these variables are decomposed in the sum of a mean and a fluctuating component. The non-linear character of the Navier-Stokes equations leads to the appearance of unknown correlations between scalar quantities in the averaging procedure. These new terms are the so-called Reynolds stresses. However, there are no additional equations introduced in the procedure. Hence, the approach leads to a situation with more unknown terms than equations, which constitutes the well-known Closure Problem of the RANS equations [28]. To overcome the Closure Problem a turbulence model must be used. The present research employed a RANS approach to the resolution of the Navier-Stokes equations and hence, the turbulence model used will be addressed in forthcoming sections.

In between the DNS and the RANS equations, other approaches can be found. The Large Eddy Simulation (LES) method is based on the direct resolution of the largest turbulent structures and the modelling of those below a certain scale [96]. This approach carries out a space filtering of the Navier-Stokes equations, in contrast with the time-averaging RANS approach. However, although the LES approach generally constitutes an accurate approximation to reality, it is still unaffordable for most practical applications, form a computational point of view [29]. Apart from the previously mentioned approaches, the Detached Eddy Simulation (DES) can be highlighted too. It constitutes a hybrid of the RANS and LES approaches, trying to combine the advantages of both methods [97]. With this approach, the RANS method is employed for the resolution of the flow equations in the near-wall region, whereas the LES method is used to simulate the remaining domain [96].

2.3. Turbulence Modelling

Modelling turbulence is one of the key aspects of CFD applications. At high Reynolds numbers, the natural instabilities that occur within the flow lead to swirling structures of different scales. Ideally, velocity and pressure fluctuations derived from turbulence would be resolved to their lowest scales through the so-called DNS approach. However, as mentioned before, this is not a practical approach in most applied cases,

due to computer memory and processing time limitations. Therefore, the RANS approach was used in the present research. In order to overcome the Closure Problem thus emerged, a majority of CFD applications incorporate a turbulence model to describe and quantify the effects of turbulence on the mean flow characteristics.

Through these turbulence models, the closure is achieved by adding transport equations for a series of variables that reproduce the behaviour of the flow turbulence. Then, the turbulence scales are related to a turbulent dynamic viscosity (μ_t), which is in turn used to account for the Reynolds stresses derived from the RANS method application [29]. The relationship between the Reynolds stresses and the turbulent viscosity is established by the Boussinesq hypothesis, which states that the effect of turbulence can be accounted for as an increased viscosity in the flow.

There are different turbulence models according to the number of additional transport equations for variables related to the turbulent viscosity used to solve the Closure Problem. Two-equation models are the most frequent option, as they are able to provide a full description of turbulence in terms of time and length scales and hence reproduce a wide range of flows [98]. Among all of the existing models, there are plenty of two-equation turbulence models that have proven their efficiency to simulate hydraulic engineering phenomena.

For the numerical models developed in the present research, a comparison between different two-equation models was conducted, in collaboration with the Hydraulics Laboratory team from the Department of Hydraulic Engineering and Environment at the Universitat Politècnica de València (UPV, Spain) [70], [99]. In particular, three of the most widespread two-equation turbulence models were tested, both for the CHJ and for the typified USBR II stilling basin simulations.

Firstly, the $k-\varepsilon$ model was tested. This model involves two transport equations, one for the turbulent kinetic energy (k) and another one for its dissipation rate (ε) [100], [101]. This two-equation turbulence model has proven reasonably good performance for a wide range of flows with interest in hydraulic engineering applications [102]. The second model tested was the RNG (renormalisation-group) $k-\varepsilon$ [103]. This model applies statistical methods to derivate the averaged equations for the turbulence quantities employed by the $k-\varepsilon$ model, showing a better ability to represent flows in complex geometries and with strong shear effects [89]. Finally, the $k-\omega$ turbulence model, where ω is the specific dissipation rate of the turbulent kinetic energy, was

employed [104]. Under certain conditions, this model is able to achieve reliable approximations for particular flow conditions, such as flow near wall boundaries or with streamwise pressure gradients [86]. In order to overcome the high sensitivity of this last model to boundary conditions, the $k-\omega$ Shear Stress Transport (SST) model [105] uses a $k-\omega$ approach in the boundary layer region and is able to switch to a $k-\varepsilon$ model in the freestream areas.

The comparison between the aforementioned two-equation turbulence models for the CHJ numerical model was conducted by Bayón et al. [70]. The results showed that the hydraulic jump was successfully simulated, regardless the turbulence model chosen, being all of them able to reproduce the physics of the phenomenon under study (Figure 6). A deeper quantitative analysis of a series of hydraulic jump representative variables was also performed, comparing the results with experimental and bibliographic data. In particular, the sequent depths ratio, the hydraulic jump efficiency and the free surface profile were studied. The conclusions reached by the study confirmed the capability of all of the turbulence models to successfully simulate the CHJ, with few differences in the results. However, the RNG $k-\varepsilon$ achieved slightly better accuracies for the analysed variables when compared to literature data.

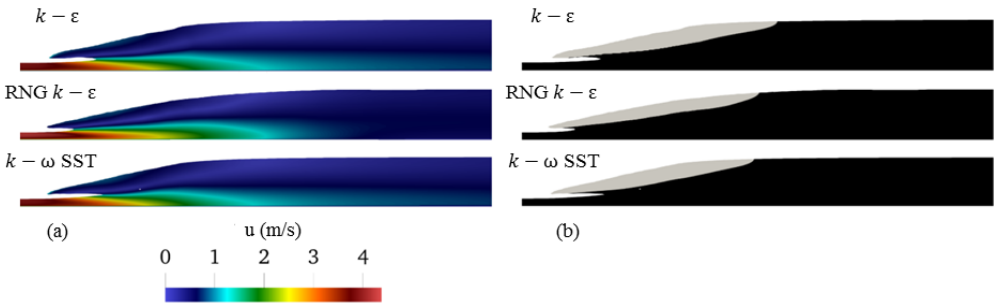

Figure 6. Longitudinal section of the CHJ simulated with the three turbulence models tested: (a) Velocity field, (b) Hydraulic jump roller region. For this comparison the numerical CFD model was developed using OpenFOAM [70].

For the typified USBR II stilling basin numerical CFD model, the comparison between turbulence models can be found in Macián-Pérez et al. [99]. The results of the numerical simulations allowed quantifying and describing in detail certain relevant hydraulic jump characteristics, such as the sequent depths ratio, the hydraulic jump efficiency and the free surface profile. All of these variables were analysed and compared with previous results coming from a literature review. This contrast showed

that the three turbulence models were able to reliably reproduce the case study in terms of the chosen variables (Figure 7). Nevertheless, and despite the similar overall performance of the three turbulence models, the RNG $k-\varepsilon$ led to results closer to those previously documented for a typified USBR II stilling basin [83].

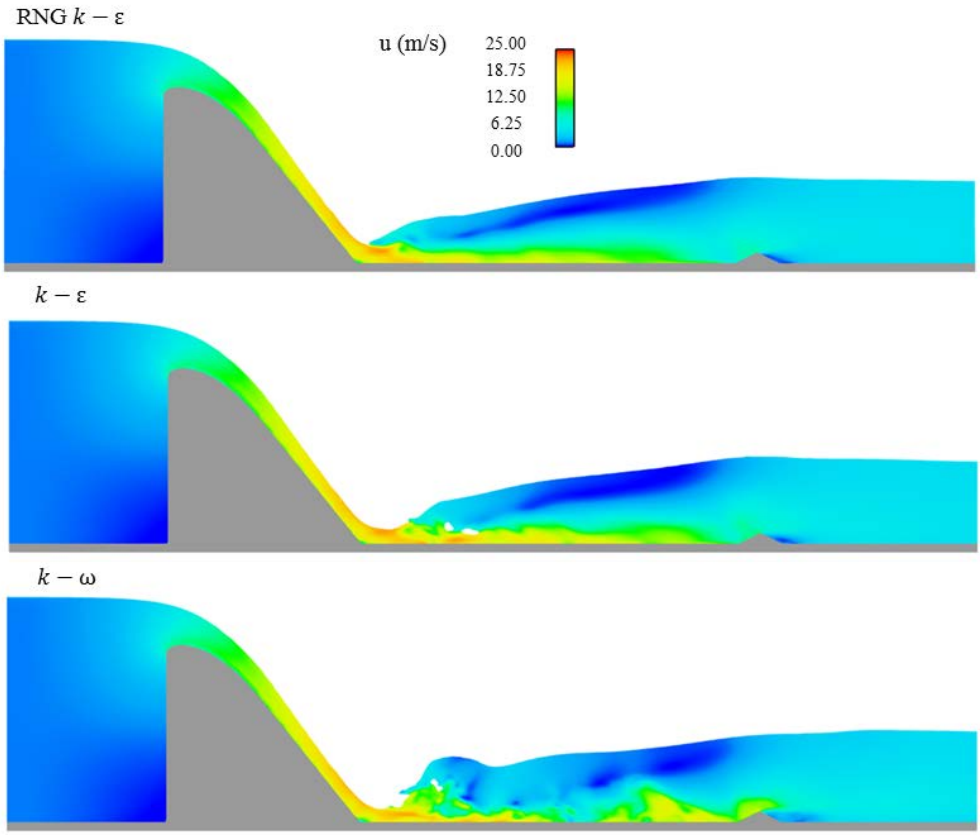

Figure 7. Longitudinal section of the Creager spillway and the typified USBR II stilling basin simulated with the three turbulence models tested displaying the velocity field. For this comparison the numerical CFD model was developed using FLOW-3D® [99].

According to the results presented, the RNG $k-\varepsilon$ was the turbulence model chosen for the research. This model has been widely used to simulate the turbulence properties [9] and, particularly, for hydraulic engineering applications [89], [106], [107]. Furthermore, for the simulation of hydraulic jumps, previous authors had already found a better performance of the RNG $k-\varepsilon$ turbulence model when compared to others

[25]. In this two-equation turbulence model, the transport of k and ε is modelled through the following equations:

$$\frac{\partial}{\partial t}(\rho k) + \frac{\partial}{\partial x_i}(\rho k u_i) = \frac{\partial}{\partial x_j}\left[\left(\mu + \frac{\mu_t}{\sigma_k}\right)\frac{\partial k}{\partial x_j}\right] + P_k - \rho\varepsilon \tag{7}$$

$$\frac{\partial}{\partial t}(\rho \varepsilon) + \frac{\partial}{\partial x_i}(\rho \varepsilon u_i) = \frac{\partial}{\partial x_j}\left[\left(\mu + \frac{\mu_t}{\sigma_\varepsilon}\right)\frac{\partial \varepsilon}{\partial x_j}\right] + C_{1\varepsilon}\frac{\varepsilon}{k}P_k - C_{2\varepsilon}\rho\frac{\varepsilon^2}{k} \tag{8}$$

where x_i is the coordinate in the i axis, μ is the dynamic viscosity, μ_t is the turbulent dynamic viscosity and P_k is the production of turbulent kinetic energy. In addition, the terms σ_k, σ_ε, $C_{1\varepsilon}$ and $C_{2\varepsilon}$, are parameters whose values are given in Yakhot et al. [103]. Finally, and according to Bayon et al. [29], the relation between the turbulent kinetic energy, its dissipation rate and the turbulent dynamic viscosity can be computed with the parameter $C_\mu = 0.085$:

$$\mu_t = \rho C_\mu \frac{k^2}{\varepsilon} \tag{9}$$

2.4. Free Surface Modelling

Accurately modelling the free surface constitutes one of the key issues to allow a generalised use of CFD techniques for hydraulic engineering applications. In the case of highly turbulent flows, with intense air entrainment, such as the ones analysed in the present research, this issue becomes even more important [28], [29]. FLOW-3D® bases its strategy to model and track the free surface on the Volume Of Fluid (VOF) method by Hirt and Nichols [88]. Hence, a variable named Fraction of Fluid (F) is used to determine the fractional volume of the main fluid (i.e., water for the present research). This variable reaches a value of 1 when the corresponding cell is completely filled with water and a value of 0 when it is empty. Moreover, cells with F values between 0 and 1 contain free surface. In order to track the evolution of the Fraction of Fluid throughout the meshed domain an appropriate advection numerical method must be used. The following expression allows obtaining F at each time-step:

$$\frac{\partial F}{\partial t} + \nabla \cdot (\overline{u}F) = 0 \tag{10}$$

It is also important to highlight that, in the treatment of hydraulic problems involving a free surface between air and water, FLOW-3D® allows a one-fluid approach for the resolution of the flow governing equations. With this approach, the boundary conditions are applied to the free surface in order to solve the equations only for the water phase, whereas the gas is assumed to have negligible inertia and only applies normal pressure on the free surface [108]. Consequently, a significant reduction in computing times is achieved. This one-fluid approach was used for the simulation of the typified USBR II stilling basin, as recommended by FLOW-3D® [86]. However, for the numerical model of the CHJ, the standard two-fluid approach was chosen, modelling both the air and the water phases. The reason to apply this two-fluid approach for the CHJ case is the contrast carried out using OpenFOAM. The one-fluid approach is exclusive of FLOW-3D® and therefore, achieving the most similar set up for both models was prioritised, trying to avoid bias in the comparison process.

In these terms, for the simulations concerning the CHJ, with the two-fluid approach, an entirely Eulerian method with two fluids was used to model flow aeration, as explained in Bayón et al. [29]. This approach allows the mixture of both fluids in the same cell, but locating the free surface where $F = 0.5$. Nevertheless, no additional equations were used for droplet and bubble dynamics. For the typified USBR II stilling basin simulations, the explanation on how the air entrainment process was modelled is presented in the following section.

Finally, FLOW-3D® allowed applying a series of routines to improve the modelling and refinement of the free surface. For fluids greatly differing in their densities and separated by a thin interface, such as the ones presented in this research, a free-slip velocity condition at the interface is recommended. By adding this condition, the momentum coupling can be improved. Furthermore, a mechanism was added to help close up partial voids and add interface sharpening in order to preserve the free surface and improve its tracking. This so-called *F*-packing mechanism works by creating small negative divergences in internal fluid cells [86].

2.5. Air Entrainment Modelling

Aeration is a phenomenon of paramount importance in highly turbulent air-water flows. Eddies and free surface fluctuations cause air entrapment, thus forming bubbles in the hydraulic jump body [55]. The presence of air affects the momentum transfer as

it modifies the flow macroscopic density, adds compressibility, increases its depth and induces volume bulking [27], [109]. Consequently, an accurate approximation to the air entrainment phenomena becomes a crucial issue when modelling both, a classical hydraulic jump and the flow in a stilling basin.

Nevertheless, it is important to remark that there is still a lack of understanding about the fluid mechanics of aeration [110]. In this respect, the presence of water droplets and air bubbles, which may present a characteristic length scale below the cell size of the chosen mesh, adds considerable complexity to the simulation of the phenomenon [29], [111].

As it can be found in Macián-Pérez et al. [5], the air entrainment process in FLOW-3D® is modelled by establishing a balance between stabilising forces (gravity and surface tension) and destabilising forces (turbulent kinetic energy). This allows a continuous estimation of the rate at which air enters the flow. In these terms, the volume of entrained air rate (δV) is obtained as [89]:

$$\delta V = k_{air} A_S \left[\frac{2(P_t - P_d)}{\rho}\right]^{1/2} if\ P_t > P_d\ ;\ \delta V = 0\ if\ P_t < P_d \tag{11}$$

$$P_t = \rho k\ ;\ P_d = \rho g L_T + \frac{\sigma}{L_T} \tag{12}$$

$$L_T = \frac{C_\mu^{3/4} k^{3/2}}{\varepsilon} \tag{13}$$

where P_t and P_d are respectively the destabilising and stabilising forces, and L_T is the turbulent length scale. This length scale is an approximation to the perturbations length scale [111]. The parameter C_μ has, as mentioned in the explanation of the parameters for the RNG $k-\varepsilon$ turbulence model, a constant value of 0.085. Furthermore, ρ is the water density, g the gravity component perpendicular to the free surface, σ the surface tension coefficient and k_{air} is a coefficient of proportionality that must be specifically calibrated for each case, for instance with physical modelling data. Generally, 0.5 is commonly accepted as a first guess for k_{air} [108]. In addition, A_S is the free surface area for each cell. Moreover, for cases in which aeration constitutes an important feature, affecting the behaviour of the flow, such as the ones studied herein, it is of paramount importance to consider additional physical processes of the air transport in

water [89]. To do so, FLOW-3D® takes into account bulking and buoyancy effects by using the models presented hereafter [86].

On the one hand, the density evaluation model accounts for the varying density on the flow resulting from the air entrainment process. To do so, the fluid mixture density (ρ_m) in each cell is computed as a linear relationship of the two fluid densities, namely, the water density (ρ) and the air density (ρ_a). The Fraction of Fluid function (F) defined for the free surface modelling is used to this end:

$$\rho_m = F\rho + (1 - F)\rho_a \tag{14}$$

On the other hand, the drift-flux model reflects the interaction between the two phases, with the air bubbles moving within the fluid as a result of the difference in densities and thus, affecting the fluid motion. Hence, in the calculation of the drag between phases, the drift-flux model obtains the drag per unit volume (K_P) as:

$$K_P = \frac{1}{2} A_P \rho \left(C_D U_R + 12 \frac{\mu}{\rho R_P} \right) \tag{15}$$

where A_P is the cross-sectional area per unit volume of the dispersed phase (i.e., air), C_D is a drag coefficient defined by the user, being 0.5 the general default value for spheres, U_R is the magnitude of the relative/slip velocity, μ the water dynamic viscosity and R_P the average particle radius. In addition to this, the minimum and maximum volume fraction values for water were established as 0.1 and 1 respectively, being the gas escape at the free surface enabled. This implies that the free surface was identified with an air concentration of 90%, as commonly indicated in experimental research [89]. Regarding the volume fraction threshold that controls when the dispersed phase turns into a continuous fluid, it was set so that water always remains as the continuous phase, following the guidelines of the FLOW-3D® [86] manual. More information regarding the FLOW-3D® drift-flux model can be found in Brethour and Hirt [112].

Furthermore, the potential affection of high air fractions to the relative velocity between phases (u_r) is taken into account adopting the Richardson and Zaki approach [113], which introduces an adjusted relative velocity (u'_r):

$$u'_r = u_r \cdot max(0.5; F)^{R_m R_z} \tag{16}$$

where R_m is the Richardson–Zaki coefficient multiplier, which was kept as the default value of 1, and R_z the Richardson–Zaki coefficient, determined from the bubble Reynolds number [86].

2.6. Meshing Information

An appropriate meshing of the spatial domain under study is crucial to achieve an accurate numerical model, saving as many computational resources as possible. The spatial domain subject of the present study both, for the CHJ and for the typified USBR II stilling basin, as well as the corresponding geometry were relatively simple, which favours the use of a structured mesh. This kind of meshes is identified by the existence of regular connectivity. According to Biswas and Strawn [114] and Hirsch [115], models using these meshes generally provide a better accuracy than those employing unstructured meshes. Furthermore, their generation algorithms are faster, presenting a lower complexity degree. In addition, a more regular access to memory is associated to structured meshes and, consequently, the latency during simulations is lower [116]. Finally, Bayon and López-Jiménez [25] stated that numerical diffusivity for free surface modelling tends to decrease if the multiphase flows are simulated using topologically orthogonal meshes.

In regards with unstructured meshes, characterised by irregular connectivity, show multiple advantages too. For instance, they are able to refine particular regions. The utility of this approach is highlighted by Kim and Boysan [117], especially for regions where important gradients of the flow variables are expected. Besides, the arbitrary topology presented by unstructured meshes is able to adapt better to complex geometries, also producing fewer closure issues [114]. However, and given the above mentioned simplicity of the domain and geometries involved in the present research, none of the advantages presented for unstructured meshes constitutes a significant improvement. Consequently, a structured rectangular hexahedral mesh was used for the study of both the CHJ and the typified USBR II stilling basin.

For the CHJ numerical model, the spatial domain consisted in a horizontal rectangular channel, where the classical hydraulic jump takes place. In the meshing process, domain volumes without flow were cropped. Moreover, a cell refinement was carried out for those other regions where potentially higher flow gradients were expected. This

was done so that the efficiency in the simulation process was increased, without affecting the results (Figure 8).

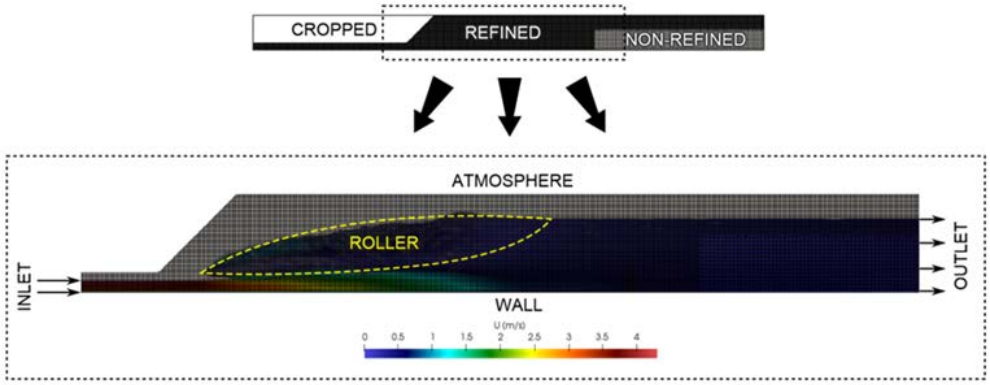

Figure 8. Longitudinal section of the CHJ showing the meshed spatial domain and the boundary conditions [70].

Regarding the typified USBR II stilling basin, a similar procedure was followed [5]. A containing mesh block was created for the entire spatial domain, including the spillway, the reservoir and the stilling basin. Then, a nested mesh block was built, with refined cells for the area of interest, in which the hydraulic jump takes place. Again, regions where flow was not expected were cropped in the procedure to save computational resources without affection to the results (Figure 9).

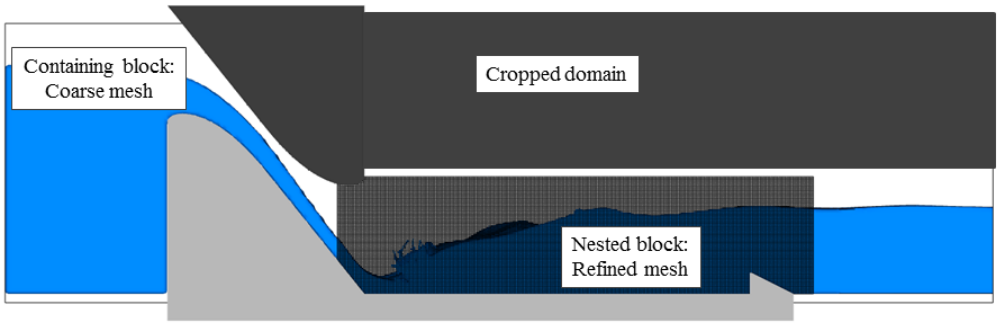

Figure 9. Longitudinal section of the Creager spillway and the typified USBR II stilling basin showing the meshed spatial domain [5].

Hence both numerical models were meshed with a coarse and a refined mesh block and consequently, two different cell sizes were used to build the final mesh. The cell size

relation between them was 1:2 in every case, for the three spatial coordinates (i.e. 1:2 relations for Δx, Δy and Δz). This was done considering that aggressive size relations between cells must be avoided in the refinement process to ensure an adequate performance of the model. As previously mentioned, the refined cells were used to mesh the regions where higher flow gradients were expected, whereas for the rest of the domain the coarse cells were employed.

2.6.1. Mesh Convergence Analysis

The mesh element size for the CFD simulations was determined through a mesh convergence analysis. This kind of analyses seeks for the independence of the model results from the imposed cell size. The analysis was developed following the American Society of Mechanical Engineers (ASME) extrapolation method presented by Celik et al. [118]. To do so, four different meshes were tested, choosing a series of basic variables (i.e., streamwise flow velocities and pressures) per mesh simulation as indicators. Each mesh had different cell sizes, considering the minimum refinement ratio of 1.3 recommended by Celik et al. [118]. Table 3 shows the cell sizes chosen for the different meshes analysed in the present research.

Table 3. Cell sizes tested for the mesh convergence analysis in the CHJ and in the typified USBR II stilling basin numerical models.

Model	Mesh	Refined block cell size	Non-refined block cell size
Classical Hydraulic Jump	1	1.667 cm	3.333 cm
	2	1.250 cm	2.500 cm
	3	1.000 cm	2.000 cm
	4	0.714 cm	1.429 cm
Typified USBR II Stilling Basin	1	0.400 m	0.800 m
	2	0.250 m	0.500 m
	3	0.180 m	0.360 m
	4	0.135 m	0.270 m

In regards with the mesh convergence analysis for the CHJ, it was conducted for both of the CFD codes used in the numerical modelling study. The resulting data for FLOW-3D® showed a limited influence of the cell size on the results compared to OpenFOAM, as previously observed by Bayón et al. [29]. This smaller sensitivity

made the model converge faster, with coarser meshes, so the best results were achieved by the mesh with cell size of 0.714 cm, with a mesh apparent order of 2.26, close to the model formal order, and a grid convergence index of 27.9%. The latter value indicates a large numerical uncertainty, in coherence with the reduced sensitivity to mesh refinement. In contrast, OpenFOAM showed a clearer convergence process, but that makes more refined meshes necessary to achieve reliable results. Coherently, the best results were yielded by mesh sizes below the four presented in the analysis [70]. However, the results obtained for a cell size of 0.714 cm already reflected a clear path to convergence and relatively small levels of numerical uncertainty, accomplishing the requirements of the convergence analysis. Consequently, the mesh labeled as the number 4 in Table 3 was chosen for both CFD codes. Hence, a similar mesh in both numerical models was ensured for the comparison process.

For the typified USBR II stilling basin, the mesh consisting of a containing block with a cell size of 0.36 m and a nested block of 0.18 m (mesh number 3) was chosen. In this case, the resulting model apparent order was 2.78, slightly above the model formal order. Besides, the grid convergence index was around 6%, which can be considered as an acceptable value for cases involving complex flows such as the hydraulic jump taking place in a stilling basin [29].

It is also important to remark that the difference in the magnitude order for the cell sizes showed in Table 3 has to do with the different models under analysis (CHJ or typified USBR II stilling basin). The particular conditions and dimensions of the cases studied will be addressed and developed in forthcoming sections. However, it can be highlighted that the chosen meshes provide a relatively similar total number of cells for both cases. In particular the CHJ model was meshed with 2,855,475 cells, whereas the for the typified USBR II stilling basin the mesh was formed by 3,147,040 cells, as reported by the FLOW-3D® user interface information.

2.7. Boundary Conditions

In practice, the numerical solution of the flow governing equations requires to know the solution at the initial time and at the boundaries. This apparent paradox is addressed by assuming the solution at the boundaries (setting up the boundary conditions) and then, using these assumed values to solve the equations within the spatial domain. This means that the solution of the problem is bound to the assumptions at the boundaries.

Consequently it is crucial to achieve good approximations for these boundary conditions [86].

The boundary conditions were set up specifically for each of the numerical models studied. For the CHJ these conditions ensured that the hydraulic jump occurred within the modelled channel stretch. To do so, a supercritical flow inlet and a subcritical flow outlet were imposed. The appropriate value of Fr_1 was ensured by displaying a constant flow depth at the inlet (y_1) with the corresponding velocity value computed according to Eq. 1. A subcritical boundary condition was imposed to the outlet, varying its flow depth (y_2) iteratively in order to place the hydraulic jump on the desired position. An atmospheric pressure boundary condition was set for the upper boundary of the domain. Regarding the inlet parameters for the RANS model, namely k and ε, they were set to small values arbitrarily so that they developed as the simulation advanced, since their initial value was unknown for the analysed case. In addition, the wall roughness was neglected in consistence with the small roughness of the materials involved in the case study, which were those of the experimental device (glass and PVC, for walls and streambed respectively). For the solid contours a wall non-slip condition was set. Special considerations are necessary for these boundaries because numerical resolution is usually too coarse to resolve details in the vicinity of solid walls [86]. Hence, a high Reynolds number wall function was assumed, thus allowing a significant saving in computational costs. In order to achieve a successful operation for the function, it must be ensured that the y^+ coordinate of the elements in contact with solid boundaries falls between 12 and 300 (buffer sublayer). However, this range is empirical and must be taken as a recommendation, being the final cell size dictated by the mesh convergence analysis [70]. The computation of y^+ is based on the non-dimensional velocity profiles incorporating the shear velocity (u_τ) proposed by von Kármán's [119] law-of-the-wall:

$$y^+ = y\frac{u_\tau}{\nu} \tag{17}$$

$$u^+ = \frac{u}{u_\tau} \tag{18}$$

Regarding the boundary conditions for the typified USBR II stilling basin numerical model, at the upstream boundary, a volume flow rate with the corresponding fluid elevation in the reservoir was set, according to the case study conditions. At the downstream boundary, fluid leaves the domain with an imposed flow depth, whose

value was obtained through an iterative process to ensure the correct hydraulic jump location, as previously explained. For the top boundary of the domain, atmospheric pressure was set. The treatment of the RANS model inlet variable was similar to the one previously explained for the CHJ. Furthermore, and also following the line of the CHJ numerical model, a wall non-slip condition with a high Reynolds number wall function was imposed to the solid contours [5].

2.8. Stability of the Numerical Model

Given the chaotic nature of the highly turbulent flow studied in the present research, the variables describing the phenomena were averaged in time windows long enough to ensure stationarity. To this end, it is important to reach the quasi-stationary state by running enough simulations, thus allowing a realistic representative statistical average. Reaching such conditions under the CFD modelling approach is not a straightforward process [5]. In these terms, the numerical modelling process carried out for the classical hydraulic jump and for the typified USBR II stilling basin required a sequence of successive simulations, each of them reproducing a non-stationary flow. Finally, simulations that satisfactorily represented the desired situation of a stable CHJ and a hydraulic jump in the stilling basin were obtained, with the pre-selected conditions and an adequate mesh resolution.

This final simulation was considered to achieve a steady state for the flow by presenting a variation of the fluid fraction in the spatial domain under 3.5% for the CHJ and below the 2.0% for the typified USBR II stilling basin. Once such condition was reached, additional 10 seconds of simulation were used to collect and average the variables, which are analysed in the forthcoming sections. This criterion was previously used by other authors to numerically model similar phenomena. According to Wang [9], the hydraulic jump phenomenon can be treated as steady from a statistical perspective and, consequently, properties such as the jump toe position, the free-surface profile and air bubble distributions can be time-averaged for their study. Furthermore, Bayón et al. [29], in their numerical study of the CHJ, observed that a 10 second sampling period captured several characteristic oscillation periods of the studied variables, so avoiding bias in the averaging process. To assume the stability of the solution these authors controlled the total water content in the modelled domain. Dong et al. also collected and averaged, in the last 10 seconds of a FLOW-3D®

simulation, the parameters for their study of the air-water flow on a stepped spillway, taking the variation of fluid fraction in the domain as an indicator of stability [89].

Chapter 3. Physical Modelling and Experimental Setup

The physical models developed for the study of the classical hydraulic jump and the typified USBR II stilling basin are treated in this chapter. For each of these physical models, the case study considered in their construction is addressed. Then, the characteristics of the model are detailed, followed by a description of the experimental campaign carried out in the devices. Finally, an in-depth explanation of the instrumentation used in the experimental campaigns is made.

First of all, it is important to highlight three relevant factors to be taken into account in the definition process of the practical cases analysed. The first factor is undoubtedly the scientific and engineering relevance of both, the flow phenomenon itself and the involved hydraulic structures. The second one concerns the literature guidelines in order to avoid significant scale effects on the experiments, as presented by Heller [22], which were previously approached in Table 2. Finally, the third factor to consider concerns the resources in the hydraulic laboratory in terms of available space, budget of the project, materials and laboratory instrumentation, all of them implying restrictions of different nature. The three factors are affecting in different senses to the adequate selection and definition of the case study to be analysed, in such a way that every one of them finally resulted from a compromise among the explained factors.

3.1. Case Study and Experimental Devices

3.1.1. Classical Hydraulic Jump

The case study posed for the classical hydraulic jump analysis was designed in terms of the inflow Froude (Fr_1) and Reynolds (Re_1) numbers, so that the results could be extrapolated to real-life hydraulic design applications. More specifically, the application to energy dissipation structures in large dams was addressed. The first parameter (Fr_1) was set considering the USBR [6] recommendations regarding flow energy dissipation in stilling basins. Hence, the USBR guidelines state that hydraulic jumps with Fr_1 numbers between 4.5 and 9 (i.e. stable hydraulic jumps) provide the

most efficient energy dissipation, although values up to 13 are acceptable. For the research presented herein, a value of $Fr_1 = 6$ was adopted, which falls in this range of optimal performance. In regards with the second non-dimensional number (Re_1), its choice is also very relevant as a result of the well-known limitations of physical modelling concerning scale effects. Although such scale effects depend on several factors, modelling the hydraulic jump with a high Reynolds number minimises them [22], [23], thus providing a more reliable extrapolation of experimental results and conclusions. To this end, the case study analysed herein was set up to ensure a high Reynolds number ($Re_1 = 210{,}000$). This condition, which can be stated in such a straight forward way, has actually represented an extremely challenging aspect of the whole research presented herein, involving an enormous laboratory work effort. However, it was certainly critical for the goals of the research, meant to go beyond actual knowledge and understanding of the hydraulic jump flow taking place in large-dam stilling basins.

This case study was physically modelled in an open channel, installed at the Hydraulics Laboratory of the Department of Hydraulic Engineering and Environment at the Universitat Politècnica de València (UPV, Spain). This rectangular-section channel was built with a PVC streambed and glass walls, and its dimensions were 10.00 m long, 0.30 m wide and 1.00 m high. The inlet to the system consisted in a pressure flow, with a transition between pressure and free surface flow right before the entrance of the channel. The channel pump allowed discharges up to 120 l/s, enough to reproduce a wide range of Froude numbers. The channel was also equipped with both, upstream and downstream sluice gates, which could be manoeuvred to control the supercritical and subcritical flow depths and place the hydraulic jump in the desired position (Figure 10). An electromagnetic flow meter by SIEMENS© (SITRANS MAG 5100 W) able to measure flow rates between 1 m^3/h and 2500 m^3/h, with an uncertainty < 0.1%, controlled the flow rate in this experimental device.

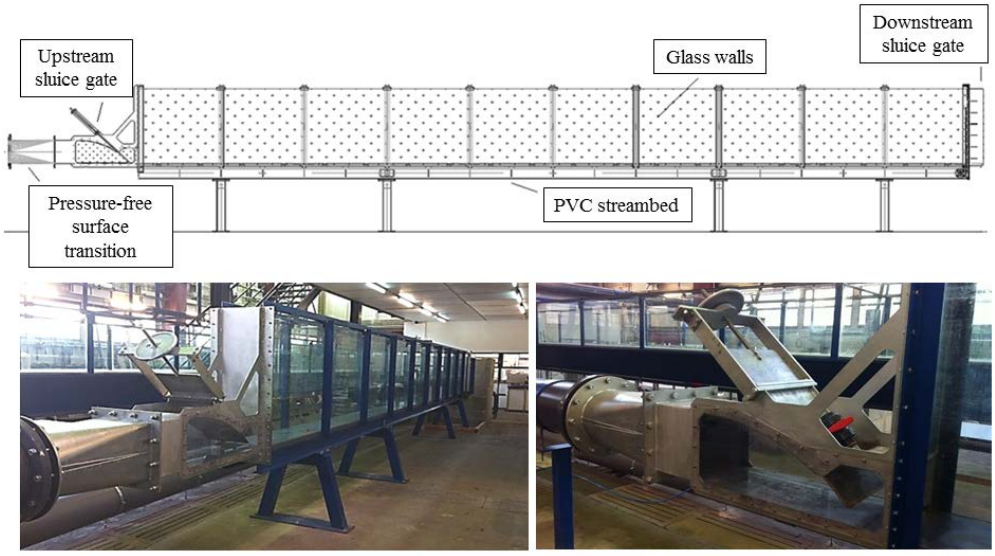

Figure 10. Open flow channel for the classical hydraulic jump model in the Hydraulics Laboratory of the Department of Hydraulic Engineering and Environment at the Universitat Politècnica de València (UPV, Spain).

In order to achieve the inflow Froude and Reynolds numbers of the case study, the discharge in the channel was set to $Q = 0.063$ m^3/s (discharge per unit width: $q = 0.21$ m^2/s). The acceleration of gravity value adopted was the standard $g = 9.81$ m/s^2. The imposed supercritical flow depth was $y_1 = 0.05$ m, which results in a supercritical flow mean velocity of $u_1 = 4.2$ m/s. Furthermore, the properties of the fluids involved in the experiments were controlled so that the following values were assumed. For water, the density and kinematic viscosity were respectively $\rho_w = 998$ kg/m^3 and $\nu_w = 10^{-6}$ m^2/s, whereas for air $\rho_a = 1.184$ kg/m^3 and $\nu_a = 1.781^{-5}$ m^2/s were used. The surface tension coefficient was $\sigma = 0.073$ N/m. These values led to an inflow Weber number of $We_1 = 12{,}058$. All of the above referred characteristics and parameters concerning the case study were also assumed in the numerical model set up. It is important to highlight that numerically modelling the flow problem with the same geometry of the experimental study, for validation purposes, may overcome issues related to scale effects or boundary conditions [12]. Table 4 summarises the most relevant flow properties for the physical model.

Table 4. Classical hydraulic jump case study physical model conditions.

	Water	**Air**
ρ **(kg/m^3)**	998	1.184
ν **(m^2/s)**	$1.002 \cdot 10^{-6}$	$1.781 \cdot 10^{-5}$
σ **(N/m)**	0.073	
u_1 **(m/s)**	4.20	--
y_1 **(m)**	0.050	--
Q **(m^3/s)**	0.063	--
q **(m^2/s)**	0.210	--
Fr_1	6.00	--
Re_1	210,000	--
We_1	12,058	--

The experimental campaign carried out in the model was intended to comprise not only the hydraulic jump roller, but also the upstream supercritical flow and the downstream subcritical flow. This was done to achieve a characterisation of the hydraulic jump as complete and accurate as possible. Hence, the free surface profile was measured employing different techniques. Due to the complex geometry arising at the hydraulic jump profile, the use of several techniques is recommended, in order to obtain a deeper contrast and a more reliable free surface profile characterisation [120]. Thus, the instant and average free-surface profiles throughout the hydraulic jump were obtained from the experimental channel using Digital Image Processing (DIP) techniques. Moreover, the free-surface position was also recorded at several points along the hydraulic jump using ultrasound distance meters. Finally, point gauge measurements using limnimeters were taken throughout the channel in order to contrast the DIP and ultrasound sensor results. The free surface profile results hence obtained also provided information about other classical hydraulic jump features such as the sequent depths ratio or the hydraulic jump efficiency.

Velocities were also measured using different instrumentation depending on the analysed hydraulic jump region. An Acoustic Doppler Velocimeter (ADV) was used to measure velocity distributions downstream the hydraulic jump roller, while for the roller flow and the supercritical flow upstream the roller, a back-flush Pitot tube was employed. Velocity measures in the roller region using the Pitot tube also allowed the indirect estimation the roller length, through the stagnation point criterion. Following

this criterion, a series of streamwise velocity vertical profiles were measured throughout the hydraulic jump roller. Then, the point where velocity tends to zero (stagnation point) was identified for each of these profiles. Finally, the intersection between the line joining the stagnation points and the average free surface indicated the end of the roller position [48]. The hydraulic jump roller length was then estimated as the measured distance from the hydraulic jump toe to this roller end position.

Pressure and temperature transmitters were also used. There were holes located every 50 cm along the channel streambed longitudinal axis. These holes could host the transmitters. They remained blocked when they were not in use, in order to ensure the water tightness of the channel. Hence, pressure transmitters could be adequately located in multiple positions all along the experimental device.

3.1.2. Typified USBR II Stilling Basin

The experimental analysis of the typified USBR II stilling basin was conducted through a reduced scale physical model with Froude similarity. This physical model was built form a prototype scale case study consisting of a spillway and a stilling basin [5]. The design of the case study was based on the analysis of a series of existing dams in the Júcar River Basin (Spain), prioritising the creation of a general and representative case. From this analysis, the design of the structure was established and the dimensions and discharge of the spillway and stilling basin were determined (Figure 11). Regarding the spillway, a Creager profile was chosen [121]. In addition, the reservoir water level that leads to the established discharge was obtained through the corresponding calculations [1], [121]–[123]. To do so, the expression proposed by the USBR to assess the discharge over an uncontrolled overflow ogee crest was employed [122]:

$$q = C_{dis}(H_d - h)^{3/2} \tag{19}$$

where q is the unit discharge, H_d is the water level in the reservoir and h is the dam height. The value of the discharge coefficient (C_{dis}) was obtained in accordance with Senturk [121] and Vischer and Hager [1]. Finally, the coordinates of the Creager spillway profile were determined through the analytical expression presented by Senturk [121]:

$$\frac{y}{H_d} = 0.47\left(\frac{x}{H_d}\right)^{1.80} \tag{20}$$

For the energy dissipation structure, as mentioned before, a typified USBR II stilling basin was designed, following the recommendations and patterns of the United States Bureau of Reclamation (USBR) [6]. These guidelines allowed obtaining not only the dimensions of the basin but also the size and distribution of the energy dissipation devices, namely chute blocks and end sill. The Creager profile spillway and the typified USBR II stilling basin have been widely used and studied all around the world [49], [83], [124] and thus, were considered to constitute a representative case study.

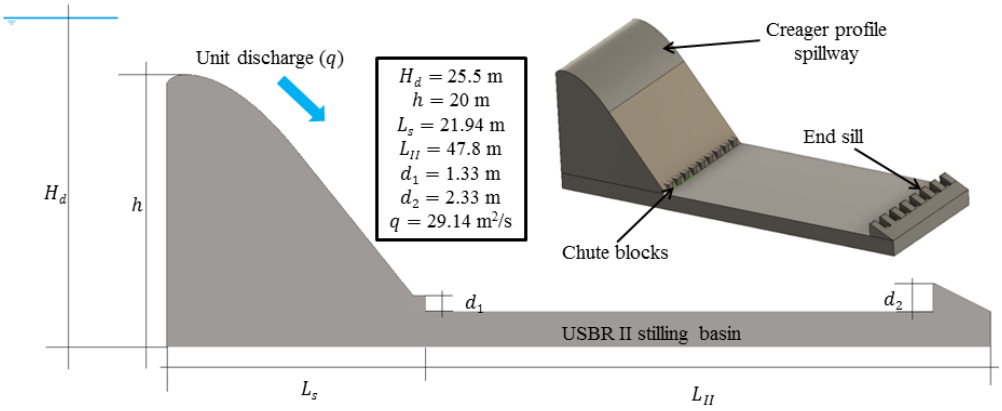

Figure 11. Creager profile spillway and typified USBR II stilling basin with the basic information regarding flow conditions and dimensions of the prototype case study (TUWien, Austria) [5].

Apart from the dimensions showed in Figure 11, it is important to remark that the width and spacing of the chute blocks equaled its height ($w_1 = s_1 = d_1 = 1.33$ m) whereas, for the end sill, the width and spacing of the blocks was $w_2 = s_2 = 1.67$ m. This dimensions were also obtained following the recommendations in the USBR design guidelines [6].

On the one hand, the numerical model for the analysis of the typified USBR II stilling basin, addressed in previous sections, was set considering the presented prototype case study conditions and dimensions. On the other hand, a reduced scale physical model of the case study was built in the Hydraulics Laboratory of the Institute of Hydraulic Engineering and Water Resources Management, at the Technische Universität Wien (TUWien, Austria) [5]. The construction of the physical model was made considering the scale effects limiting criteria stated by Heller [22], together with the available resources at the Hydraulics Laboratory. Consequently, a scale factor of 1:25 was adopted, with regards to the dimensions for the prototype case study displayed in

Figure 11. A rectangular section open flow channel was used to locate the spillway and the stilling basin, in order to build the physical model. The dimensions of the channel were 10.00 m long, 0.49 m wide and 1.10 m high. This channel was equipped with a downstream gate, that could be operated to achieve the hydraulic jump desired position and a glass wall in the area of interest (Figure 12).

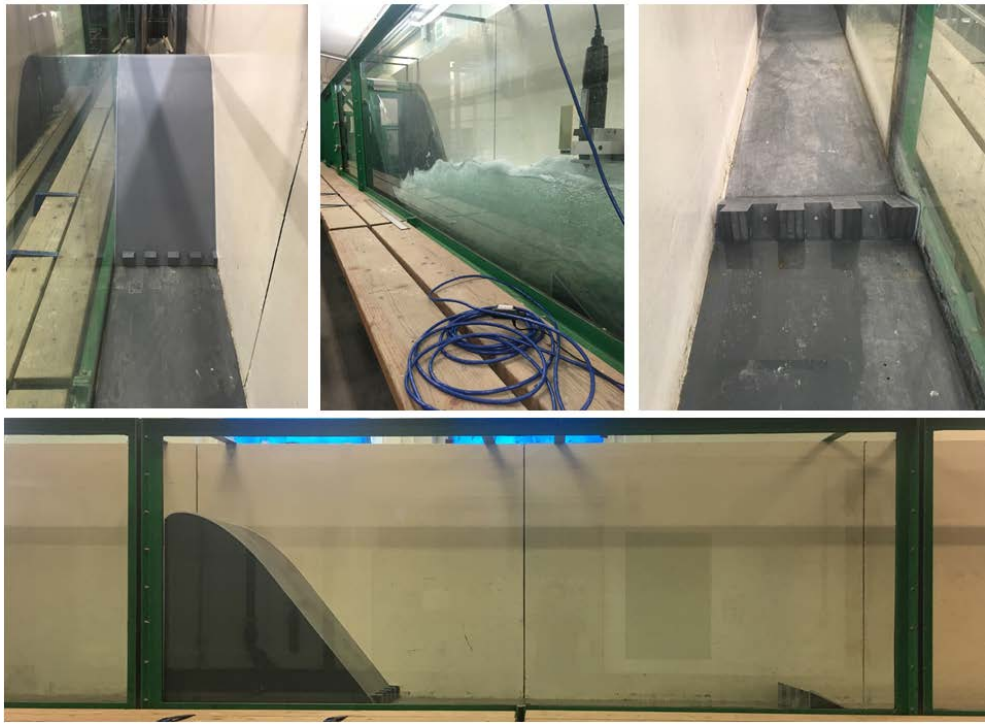

Figure 12. Open flow channel with the typified USBR II stilling basin reduced scale physical model in the Hydraulics Laboratory of the Institute of Hydraulic Engineering and Water Resources Management, at the Technische Universität Wien (TUWien, Austria).

In this case, the inflow Froude number was not directly imposed, like it was done for the CHJ study. In contrast, the spillway and the reservoir were designed with the appropriate dimensions and hydraulic conditions, according to the previously referred revision of a series of Spanish dams. The corresponding discharge calculations (Eq. 19) [1], [121]–[123], together with the involved fluid properties led to the theoretical physical model conditions displayed in Table 5 which, in turn, were used for the design of the basin [6]. It is important to remark that the reduced scale physical model was designed with Froude similarity. This implied that the inflow Froude number in this

model remained similar to the one in the numerical model, which was developed at the prototype scale.

Table 5. Typified USBR II stilling basin theoretical physical model conditions (TUWien, Austria).

	Water	**Air**
ρ **(kg/m^3)**	1000	1.225
ν **(m^2/s)**	10^{-6}	$1.470 \cdot 10^{-5}$
σ **(N/m)**	0.073	
u_1 **(m/s)**	4.47	--
y_1 **(m)**	0.052	--
Q **(m^3/s)**	0.114	--
q **(m^2/s)**	0.233	--
Fr_1	6.26	--
Re_1	233,000	--
We_1	14,287	--

Once both, the numerical and the physical model were developed, the results showed that the inflow Froude number was lower than the one obtained in the theoretical design of the case study. Hence, as discussed in forthcoming sections, the Froude number for the incoming flow to the stilling basin reached a value close to 5, with good agreement between the physical and the numerical models. The value achieved for the inflow Froude number fell in the range of optimal performance for energy dissipation purposes proposed by the USBR [6]. Furthermore, and according to Fernández-Bono and Vallés-Morán [17], the obtained Froude number, together with the unit discharge and the reservoir water level, constituted an adequate case for the use of a typified USBR II stilling basin. Hence, the case study was analysed without compromising the potential conclusions of the research.

Nevertheless, another typified USBR II stilling basin physical model was developed in the Hydraulics Laboratory of the Department of Hydraulic Engineering and Environment at the Universitat Politècnica de València (UPV, Spain), aiming to test higher values for the inflow Froude number. This model was built in a horizontal rectangular section open flow channel. Its dimensions were 8.00 m long, 0.77 m wide and 0.64 m high, with glass streambed and methacrylate walls (Figure 13). The channel was equipped with a downstream sluice gate that could be manoeuvred to place the

hydraulic jump in the appropriate position. In addition, its entrance was connected to another rectangular section channel, which formed an angle of 53.80° with the horizontal, in order to model the spillway. In terms of the pumping system, the inlet was made through a pressure flow, with a transition to free surface flow right before the entrance of the sloping channel. The device pumping system allowed discharges up to 120 l/s, enough to achieve the design conditions needed to reach a higher Froude number.

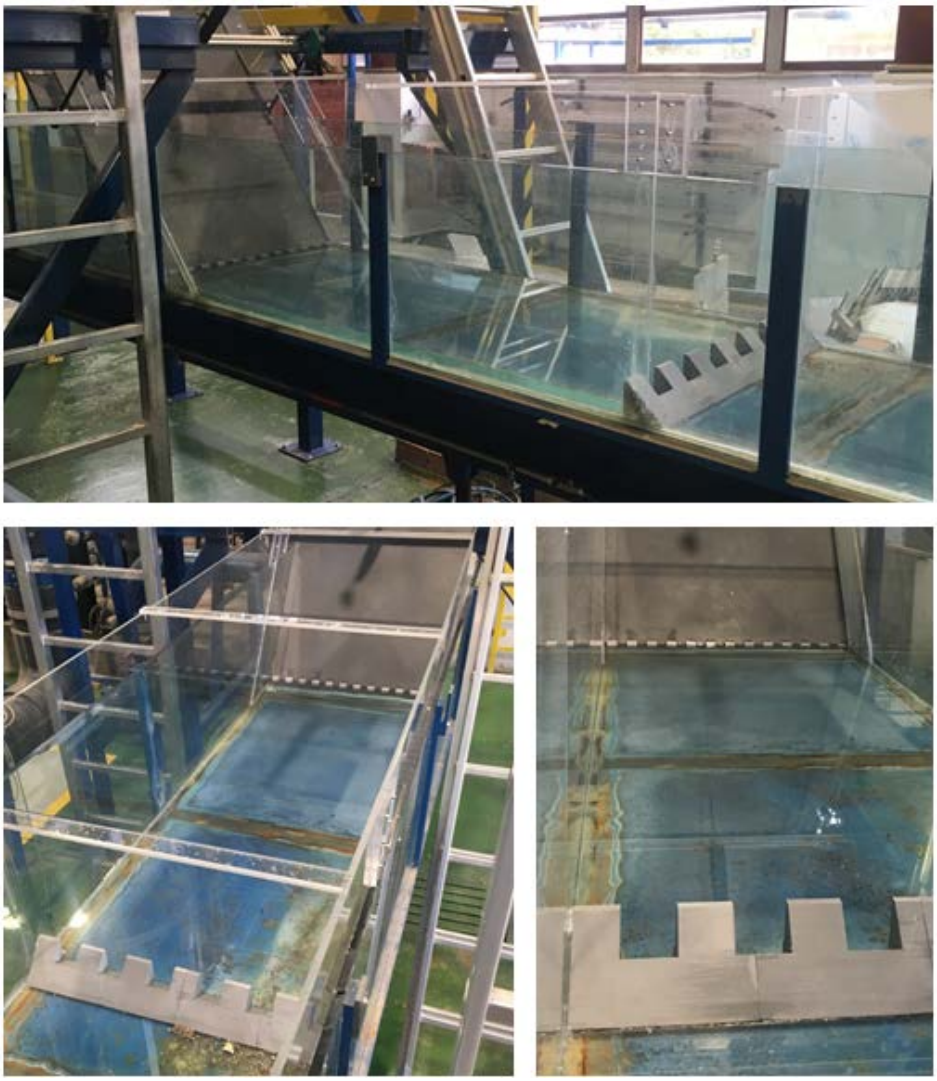

Figure 13. Open flow channel with the typified USBR II stilling basin physical model in the Hydraulics Laboratory of the Department of Hydraulic Engineering and Environment at the Universitat Politècnica de València (UPV, Spain).

The experimental device showed in Figure 13 allowed controlling the discharge and the flow depth in the sloping channel. Consequently, the inflow Froude number to the

stilling basin was imposed, taking into account the properties of the involved fluids. Table 6 summarises the conditions posed for the physical model.

Table 6. Typified USBR II stilling basin physical model conditions (UPV, Spain).

	Water	**Air**
ρ **(kg/m^3)**	1000	1.225
ν **(m^2/s)**	10^{-6}	$1.470 \cdot 10^{-5}$
σ **(N/m)**	0.073	
u_1 **(m/s)**	4.89	--
y_1 **(m)**	0.030	--
Q **(m^3/s)**	0.113	--
q **(m^2/s)**	0.147	--
Fr_1	9.02	--
Re_1	147,000	--
We_1	9,834	--

These physical model conditions, which again considered the recommendations made by Heller [22] to avoid significant scale effects, were used in the design of the typified USBR II stilling basin. Hence the guidelines presented by the USBR [6] were followed to obtain the dimensions of the basin displayed in Figure 14, which constitute the physical model analysed. In regards with the energy dissipation devices that can be observed in Figure 13, they were built through a 3D printing process in which a Prusa MK3 3D printer by Prusa Research© was used. The material in which the pieces were printed was the thermoplastic known as polylactide (PLA), derived from renewable resources such as the corn.

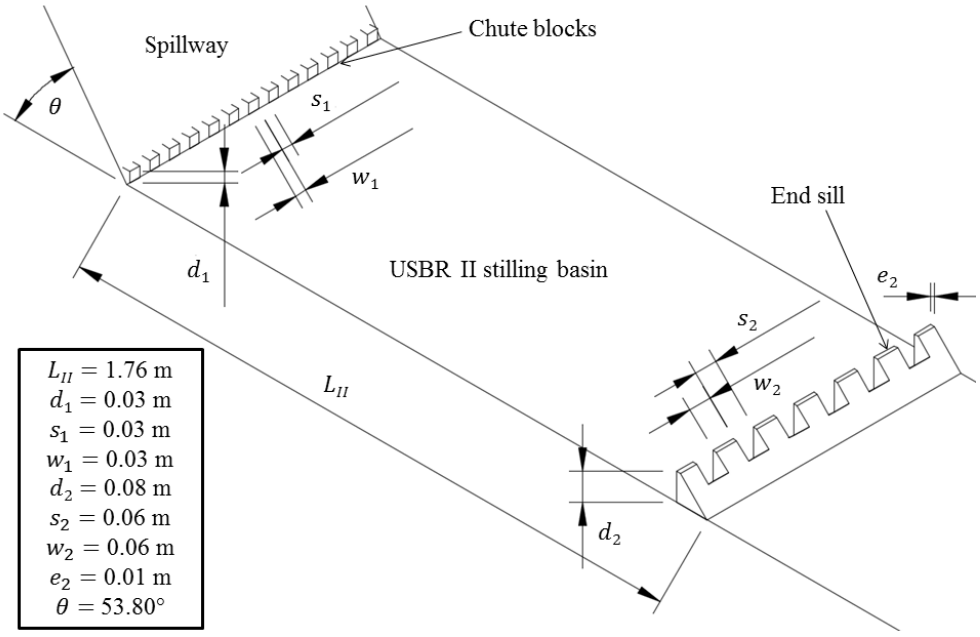

Figure 14. Typified USBR II stilling basin with the basic information regarding the dimensions of the physical model case study (UPV, Spain).

The experimental campaign carried out in the two typified USBR II stilling basin physical models largely depended on the available instrumentation in each of the laboratories. For the model at the TUWien, the free surface profile was measured throughout the hydraulic jump using Digital Image Processing (DIP) techniques, together with local measures using limnimeters to contrast the results. This flow depth data also allowed obtaining the sequent depths ratio and the hydraulic jump efficiency. Moreover, velocities in a series of vertical profiles in the supercritical and the subcritical regime were measured using a turbine velocity meter. In addition, pressures in the end sill of the stilling basin were measured employing pressure transmitters. Finally, the void fraction distribution within the hydraulic jump was obtained. To do so, several vertical profiles along the hydraulic jump longitudinal axis were measured using an optical fibre probe.

Regarding the model at the UPV, the experimental campaign was mainly focused on the determination of the free surface profile and the velocity field within the hydraulic jump. A method using a time-of-flight camera, based on a light detection and ranging

(LIDAR) technique was used to measure the free surface profile, the sequent depths ratio and the hydraulic jump efficiency. Furthermore, a series of streamwise velocity vertical profiles were measured along the basin longitudinal axis using a back-flush Pitot tube. These velocity profiles also allowed estimating the hydraulic jump roller length, by using the previously explained stagnation point criterion [48].

A summary of the experimental campaigns carried out in the presented models is displayed in Table 7.

Table 7. Instrumentation used in the experimental campaign for each of the physical models developed.

Hydraulic Jump Feature	Instrumentation	Classical Hydraulic Jump	USBR II stilling basin (TUWien)	USBR II stilling basin (UPV)
Free surface profile	Digital Image Processing	x	x	
	Ultrasound distance meter	x		
	Limnimeters	x	x	x
	LIDAR			x
Velocity distribution	Pitot tube	x		x
	Acoustic Doppler Velocimeter (ADV)	x		
	Turbine velocity meter		x	
Pressure distribution	Pressure transmitters	x	x	
Void fraction distribution	Optical fibre probe		x	

3.2. Instrumentation

Before undertaking a deep description of the experimental instrumentation used for the present research, it is important to emphasise that the flow under study is extremely complex. It is this circumstance that makes it recommendable to tackle the measuring problem by means of several combined techniques, in order to achieve an optimal representation of the flow under study. According to Wang [9], the experimental measures are restricted by the severely turbulent and highly aerated nature of hydraulic jumps. The flow pattern is sensitive to any large size intrusive equipment, whereas the bubbly flow tends to prevent from the use of many non-intrusive instruments. In this

regard, obtaining reliable measures of certain variables remains a challenging goal, given the available measuring devices and experimental limitations [5], [12]. According to Valero et al. [12], even a perfectly sampled data series could still present uncertainties related to the limitations on the measuring time or the data acquisition rate. Consequently, there was an unavoidable degree of uncertainty associated with the parameters studied in the experimental campaigns carried out. However, the design of these campaigns was made trying to reduce as much as possible this uncertainty, choosing appropriate measuring times and locations. Furthermore, the corresponding preliminary analyses of the data were conducted, in order to discard anomalous measures or those other values lacking of physical sense.

3.2.1. Digital Image Processing

Digital Image Processing (DIP) techniques were used to determine the free surface profile for the classical hydraulic jump as well as for the typified USBR II stilling basin (TUWien) case study. This method has been previously used to provide information regarding the hydraulic jump free surface profile [5], [29], showing satisfactory results. Both, the instant and average free-surface profiles throughout the hydraulic jump were captured from the experimental devices employing DIP. To this end, an edge detection method based on a light intensity threshold allowed identifying air-water interfaces in videos of the hydraulic jump profile recorded at 50 Hz with a resolution of 1280 x 720 pixels. These videos were recorded from one of the channel sides, with adequate illumination conditions (Figure 15). In order to improve the quality of the recorded results, perspective effect correction and filtering algorithms to remove the bias caused by reflections, droplets and others were applied. This process was developed and applied by Dr. Bayón.

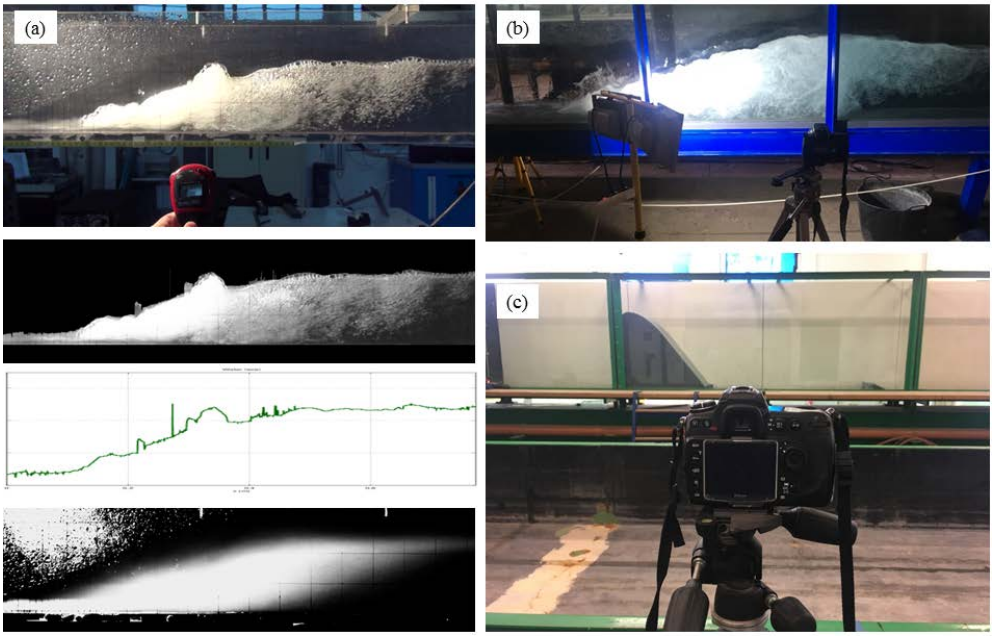

Figure 15. Digital Image Processing (DIP) technique for free surface profile determination: (a) DIP procedure [29], (b) DIP for the classical hydraulic jump model in the Hydraulics Laboratory of the Department of Hydraulic Engineering and Environment at the Universitat Politècnica de València (UPV, Spain), (c) DIP for the typified USBR II stilling basin model in the Hydraulics Laboratory of the Institute of Hydraulic Engineering and Water Resources Management, at the Technische Universität Wien (TUWien, Austria).

The information obtained with DIP techniques regarding the free surface profile was contrasted by using a HC-SR04 ultrasound distance meter. With this device, connected to a Raspberry Pi 3 B+, the flow depth was recorded at several points along the hydraulic jump. Its working principle is based on creating an echo that propagates in the air until it reaches the water surface and then, measuring the time it takes to be received back. Hence, it allows a dynamic estimation of the free surface [12]. The ultrasonic distance meter was capable of measuring at sampling rates larger than 5 Hz, way above that of the roller region free surface fluctuations and the wave formation phenomena in the subcritical regime [70].

Finally, point gauge measurements using limnimeters were also conducted throughout the channels to support the information provided by the DIP techniques and the ultrasound distance meter. According to Valero et al. [12], the accuracy of classic point

gauges is often referred to be in the order of 0.1 mm for hydraulic jump flow depth measurements. In addition, they can only provide information on static water levels.

3.2.2 LIDAR

A time-of-flight camera was used to measure the free surface position of the hydraulic jump in the typified USBR II stilling basin physical model at UPV, in collaboration with colleagues from the Instituto Universitario de Restauración del Patrimonio. This technology, based in the development of light detection and ranging (LIDAR) techniques, is increasingly gaining importance for a wide range of applications, including the hydraulic engineering field [59], [60]. The working principle provides the distance between the sensor and the subject (the hydraulic jump free surface in this particular case) by measuring the trip time of the signal emitted. It is precisely the intense aeration of the hydraulic jump free surface that allows reflecting the signal [59], [60]. Hence, the time-of-flight camera is able to locate the surface and generate the corresponding 3D model. The camera output consists in a series of frames composed of point clouds, as showed in Figure 16. It is important to highlight that the distance between the camera and the subject affects the density of these point clouds, with larger number of points for positions closer to the camera.

The information collected using this technology was processed to obtain the hydraulic jump free surface longitudinal profile. Firstly, it was necessary to establish a series of references in the channel structure to adequately locate and dimension the output point clouds. Then, for each frame, the points in the surroundings of the longitudinal axis were collapsed to obtain the 2D information that was used for the analysis here presented. Furthermore, the anomalous data coming from droplets or channel structure interferences was filtered. Finally, for each of these profiles a series of bands containing a particular percentage of the collected points were established. From these bands the mean free surface profile was obtained, as explained in forthcoming sections.

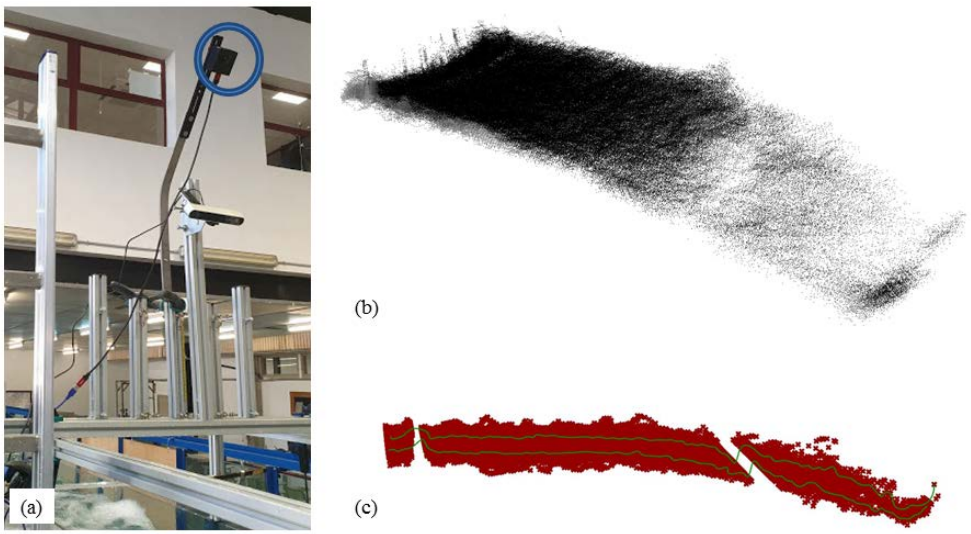

Figure 16. Light Detection and Ranging (LIDAR) techniques in the Hydraulics Laboratory of the Department of Hydraulic Engineering and Environment at the Universitat Politècnica de València (UPV, Spain): (a) Time-of-flight camera, (b) Cloud of points obtained measuring the hydraulic jump in the typified USBR II stilling basin physical model, (c) Band containing the 80% of the points collected.

Some limitations of this technology are similar to those of other distance detection methodologies. Important reflections or completely transparent surfaces can prevent from using LIDAR techniques. Therefore, the aeration of the hydraulic jump surface was crucial. Furthermore, the control of certain parameters in the process, such as the collection time, allowed generating a large number of measurements and thus averaging a less biased point cloud.

3.2.3. Pitot Tube

A Pitot tube, based on differential pressure measures, was used to obtain streamwise velocity values in the studied physical models. In particular, the device used was a Pitot tube connected to a General Flow Sensor by PASCO©, which allowed obtaining flow velocities up to 10 m/s. With this device, flow velocity was obtained by measuring the difference in pressure between the two input tubes connected to the

sensor. The Pitot tube data acquisition frequency was 50 Hz for all the presented experimental campaigns.

This device was available for its use in the Hydraulics Laboratory of the Department of Hydraulic Engineering and Environment at the Universitat Politècnica de València (UPV, Spain). Hence it was employed to measure streamwise velocity vertical profiles in the classical hydraulic jump and in the typified USBR II stilling basin (UPV) physical models (Figure 17). On the one hand, for the CHJ experimental campaign, 5 different vertical profiles were measured in the roller region along the channel longitudinal axis, with around 15 points per profile and 60 s of acquisition time per point. A couple of profiles were also measured in the supercritical regime upstream the hydraulic jump toe. On the other hand, for the stilling basin campaign, 7 streamwise velocity vertical profiles were characterised, maintaining the number of points and acquisition times already mentioned for the CHJ.

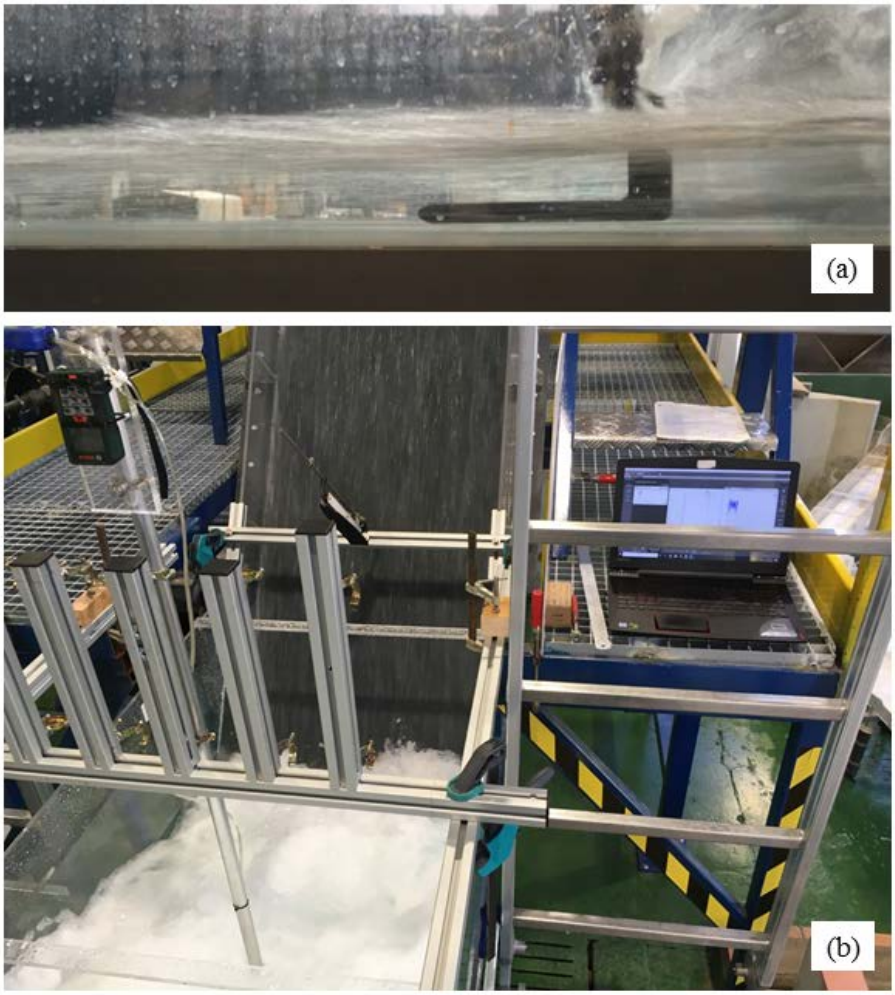

Figure 17. Pitot tube in the Hydraulics Laboratory of the Department of Hydraulic Engineering and Environment at the Universitat Politècnica de València (UPV, Spain): (a) Measures in the supercritical regime upstream the classical hydraulic jump, (b) Measures in the hydraulic jump roller of the typified USBR II stilling basin model.

In terms of the uncertainty regarding the values obtained with this device, it has been traditionally used for measuring velocities in hydraulic jumps [41]. However, as stated by Wang [9], the results could be affected by the presence of bubbles in highly aerated flows. This affection is further developed, regarding the results, in forthcoming sections.

3.2.4. Acoustic Doppler Velocimeter

The experimental campaign conducted on the CHJ was expanded to the subcritical regime downstream the hydraulic jump roller by measuring streamwise velocity vertical profiles using an Acoustic Doppler Velocimeter (ADV) (Figure 18). The ADV employed in the study was a Vectrino by Nortek©. This device allowed measuring the three components of the velocity vector in a point by the means of a working principle based on the Doppler Effect. To this end, the ADV, with its receivers remaining in a given position, uses the velocity of the particles carried by the flow to measure the flow velocity. However, it is precisely this working principle that prevents from using the device if there are flow elements such as bubbles which could potentially affect the signal [9], [12]. Therefore, the ADV was used in the present research only to measure velocities downstream the hydraulic jump roller.

Figure 18. ADV Vectrino by Nortek©, with detail of the receivers, in the classical hydraulic jump experimental device in the Hydraulics Laboratory of the Department of Hydraulic Engineering and Environment at the Universitat Politècnica de València (UPV, Spain).

The Vectrino by Nortek© offered data collection rates up to 200 Hz, and was designed to cover a range of velocities from 3 cm/s to 4 m/s. For the experimental campaign in the classical hydraulic jump, two vertical profiles were measured in the longitudinal axis of the channel. For each of these profiles, data was collected in five points during 60 s. In regards with the acquisition frequency the profiles were measured at 100 and

200 Hz. However, no significant differences were found and hence, the data obtained at 100 Hz, which was easier to handle, was analysed.

3.2.5. Turbine Velocity Meter

Velocity data was obtained in the typified USBR II stilling basin physical model in the Hydraulics Laboratory of the Institute of Hydraulic Engineering and Water Resources Management, at the Technische Universität Wien (TUWien, Austria), using a turbine velocity meter (Figure 19). Hence, streamwise velocity profiles were measured in different positions within the physical model employing a Schiltknecht (MiniWater20®) turbine velocity meter, which could measure velocities up to 5 m/s. The working principle of this device is based on the rotation frequency of a turbine. This rotation frequency, which depends on the water velocity, is then converted into an analogical output that gives a measure of the flow velocity. The experimental campaign conducted in this physical model, regarding velocity data acquisition, covered the following positions: the flow in the spillway, right before the beginning of the stilling basin, the flow in the stilling basin, close to the end sill, and the flow downstream of the end sill [5].

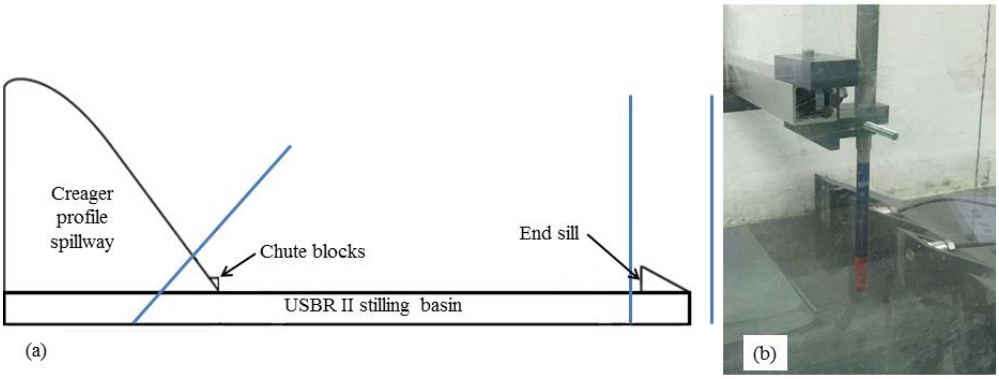

Figure 19. Turbine velocity meter in the typified USBR II stilling basin model in the Hydraulics Laboratory of the Institute of Hydraulic Engineering and Water Resources Management, at the Technische Universität Wien (TUWien, Austria): (a) Cross-sectional positions where profiles were measured, (b) Turbine velocity meter placed in front of the end sill.

In particular, two profiles were measured for the supercritical flow in the spillway, in the same cross-sectional position of the channel. The characteristics of the instrumentation and the relatively low flow depths in the spillway led to measuring

only 2 points per profile. For the measures conducted upstream and downstream the end sill of the stilling basin, also two profiles were taken for each cross-sectional position. In this case, the profiles consisted of 5 points. The reason to measure two profiles per cross-sectional position was to analyse the influence of the energy dissipation devices of the model in the three-dimensional structure of the flow.

For each of the points forming the referred profiles, data was collected during 180 s, with an acquisition frequency of 2 Hz. It was precisely this relatively low acquisition frequency of the device that prevented from taking velocity measures in the hydraulic jump roller, where turbulence and velocity fluctuations are more intense.

3.2.6. Pressure Transmitters

Pressure values were collected in the streambed of the classical hydraulic jump physical model and also in the end sill of the typified USBR II stilling basin in the Hydraulics Laboratory of the Institute of Hydraulic Engineering and Water Resources Management, at the Technische Universität Wien (TUWien, Austria). To this end, a series of KELLER AG© pressure transmitters were used. These devices, with the corresponding software, allowed recording quick and precise pressure measurements through their piezoresistive transducer and microprocessor with a converter (Figure 20).

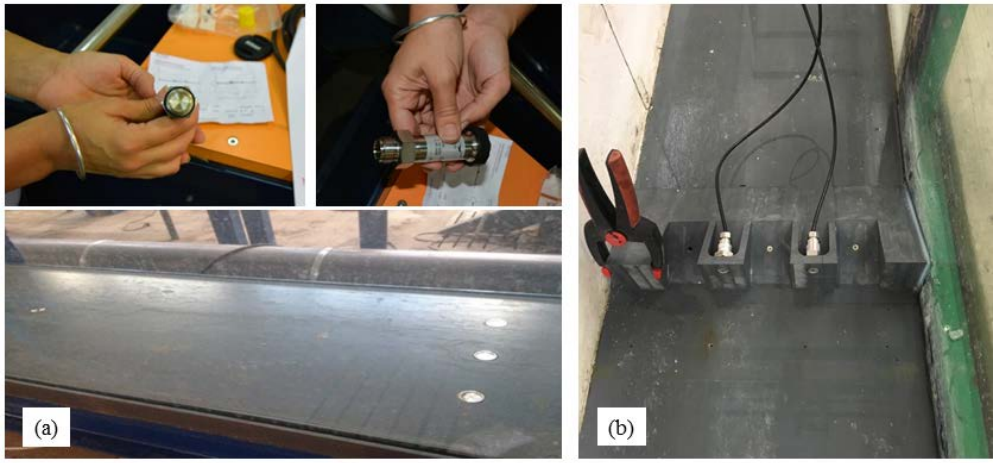

Figure 20. (a) Pressure transmitters and holes to place them in the streambed channel for the classical hydraulic jump in the Hydraulics Laboratory of the Department of Hydraulic Engineering and Environment at the Universitat Politècnica de València (UPV, Spain), (b) Pressure transmitters in the end sill of the typified USBR II stilling basin model in the Hydraulics Laboratory of the Institute of Hydraulic Engineering and Water Resources Management, at the Technische Universität Wien (TUWien, Austria).

On the one hand, for the CHJ, the transmitters were located along the channel streambed longitudinal axis. On the other hand, for the stilling basin physical model, pressure values were measured in two different positions on the front side of the blocks forming the end sill. The acquisition time was 60 s for every sensor. Furthermore, two acquisition frequencies were tested (50 and 200 Hz). The analysis of the resulting data showed that the first of these frequencies was sufficient to ensure stable results [5]. It is important to highlight that these pressure transmitters are highly sensitive to the presence of solid particles in the flow, which can even disable the devices.

3.2.7. Optical Fibre Probe

The void fraction distribution within the typified USBR II stilling basin physical model in the Hydraulics Laboratory of the Institute of Hydraulic Engineering and Water Resources Management, at the Technische Universität Wien (TUWien, Austria) was obtained. Data was collected measuring with a dual-tip optical fibre probe at 6 different vertical profiles along the hydraulic jump longitudinal axis. For each of these profiles, displayed in Figure 21, 9 to 12 points were measured. The collection data time for each

of the points was 200 s, due to the characteristics and expected velocities in the model [5], [52].

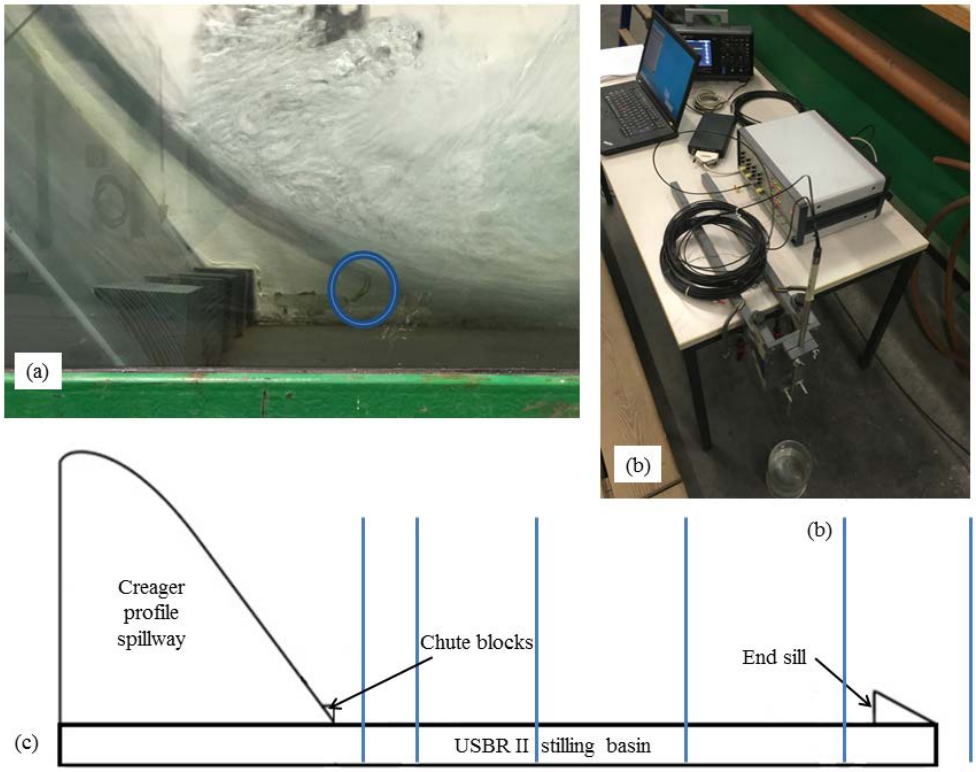

Figure 21. Optical fibre probe in the Hydraulics Laboratory of the Institute of Hydraulic Engineering and Water Resources Management, at the Technische Universität Wien (TUWien, Austria): (a) Dual-tip close to the chute blocks in the stilling basin physical model, (b) Optical fibre probe equipment, including probe, opto-electronic unit, oscilloscope, acquisition box and software [85], (c) Cross-sectional positions where profiles were measured.

Particularly, the optical fibre probe employed in the experimental campaign was an RBI Instrumentation© dual-tip optical phase detection device. The working principle of this instrument was presented by Cartellier and Archard [125], Cartellier and Barrau [126] and Boyer et al. [127]. In this respect, the discrete variation of refraction indexes between flow components (i.e., air and water) allows phase discrimination. The physical basis of the process is that, at a given emission of light, the amount reflected by the wall of an optical probe sensitive tip depends exclusively on the refraction index

of the medium that surrounds the wall. Hence, the quantity of light reflected is received by the device as an optical signal, which is then converted into an electrical signal by a photo-sensitive element. Once this is done, the void fraction can be obtained as the portion of time in which the gas phase is contacting the sensitive tip of the optical fibre probe, in relation with the full observation time.

These phase-detection probes constitute the preferred instrumentation for experimental campaigns in flows with important air concentrations such as the hydraulic jump [9], [12]. However, it must be taken into account that this is a highly fragile device. In addition, the performance of the device can be affected by the oblique impact of bubbles with the tips, as a result of cross velocities [12]. Finally, in its condition of intrusive device, the scale effect due to the probe size is difficult to identify [9].

Chapter 4. Classical Hydraulic Jump Characterisation

In this chapter, the results obtained in the study of the classical hydraulic jump are presented, analysed and discussed. Hence, a detailed characterisation is conducted, addressing the most relevant features of the phenomenon, including sequent depths ratio, hydraulic jump efficiency, roller length, free surface profile, distributions of velocity and pressure and fluctuating variables. A thorough analysis of these classical hydraulic jump features is approached hereunder.

Before starting the detailed analysis, a first qualitative assessment is made. The observation of the numerical simulations performed with CFD techniques, in comparison with the physical model, showed that they were able to reproduce the studied phenomenon in a physically-consistent way (Figure 22). Hence, the hydraulic jump occurred in the desired position. Furthermore, some relevant macroscopic qualitative characteristics, such as the subcritical and supercritical flow, the high vorticity in the roller region, the gradual air detrainment downstream of the hydraulic jump toe, etc. were in good agreement with those expected for a classical hydraulic jump [2].

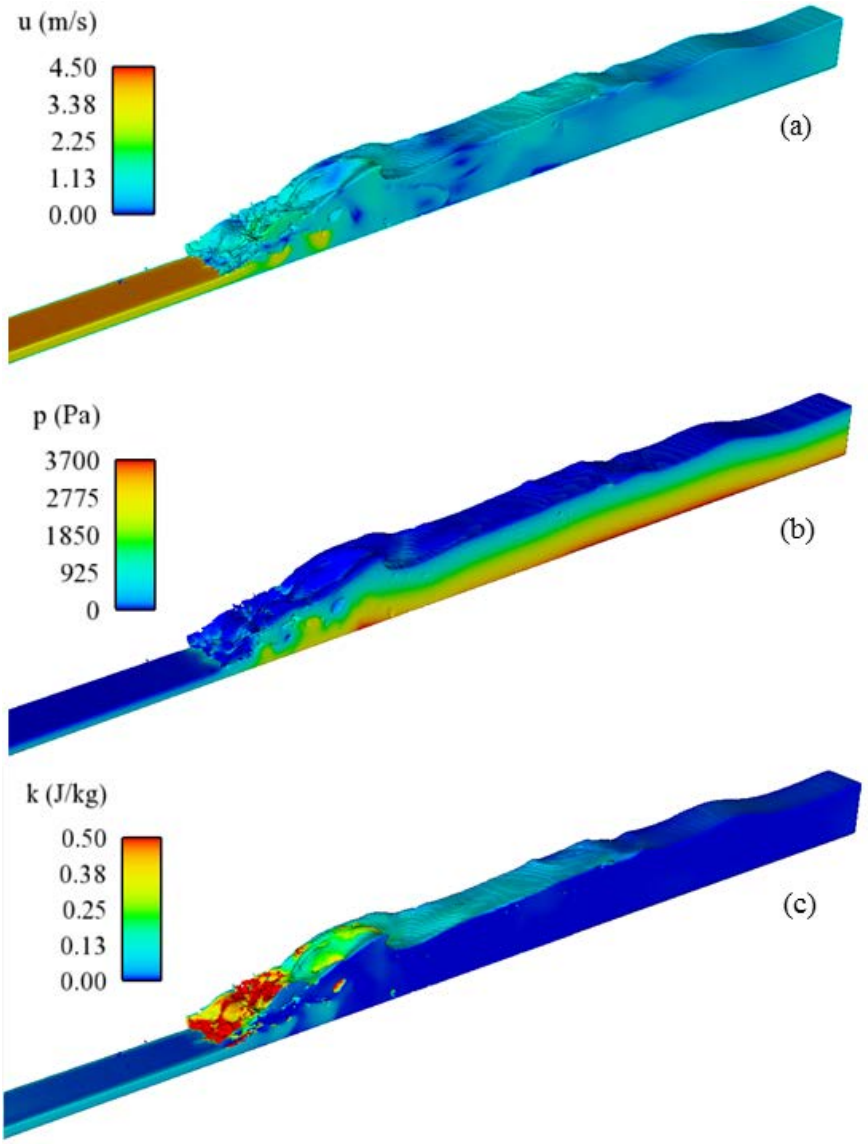

Figure 22. Classical hydraulic jump numerical model using FLOW-3D®: (a) Velocity field, (b) Pressure field, (c) Turbulent kinetic energy.

4.1. Free Surface Profile

4.1.1. Sequent Depths Ratio

Regarding the classical hydraulic jump free surface profile, the first information analysed in the numerical and physical models was the sequent depths ratio. Hence the value obtained with the two CFD codes used to simulate the hydraulic jump, namely FLOW-3D® and OpenFOAM, was compared with the one obtained in the physical model using the different experimental techniques previously presented. Furthermore, the results were compared with the expression proposed by Hager and Bremen [23]. This expression, which is based on the theoretical solution presented by Bélanger [33], also accounts for the effect of wall friction on the sequent depths ratio of the CHJ. Consequently, the influence of the inflow Froude number is considered, but also the one caused by the inflow Reynolds number, and the inflow aspect ratio:

$$y_2/y_1 = \frac{1}{2}\left(\sqrt{1+8Fr_1^2}-1\right)\cdot\left(1-0.7[(logRe_1)^{-2.5}]^{Fr_1/8}\right)\cdot\left(1-\frac{3.25y_1}{b^{Fr_1/7}}\cdot(logRe_1)^{-3}\right) \quad (21)$$

where b accounts for the hydraulic jump width. The comparison, showed in Table 8, was made in terms of accuracy. Considering ϕ as the analysed variable and ϕ_{ref} as the value used for the comparison, the expression used in the present research to obtain the percentage of accuracy was:

$$Accuracy = \left(1-\frac{|\phi-\phi_{ref}|}{\phi_{ref}}\right)\cdot 100 \quad (22)$$

Table 8. Accuracy of the sequent depths ratio for the CHJ obtained with the numerical models when compared to the physical model and theoretical expressions.

	Sequent depths ratio	**DIP**	**Ultrasound distance meter**	**Limnimeters**	**Hager & Bremen** [23]
FLOW-3D®	7.46	94.2%	96.4%	96.4%	96.5%
OpenFOAM	7.50	94.7%	96.9%	96.9%	97.0%

As it can be observed, the numerical models developed with both codes provided similar results with high accuracies in the comparison with experimental and bibliographic results. The FLOW-3D® model provided slightly lower accuracies but

still in the line of good agreement with the other sources. In addition, the sequent depths ratio values obtained in the experimental campaign with the different techniques employed were in good agreement with the theoretical value by Hager and Bremen [23]. Hence, all of the models developed for the study of the classical hydraulic jump were able to satisfactorily reproduce its sequent depths ratio.

4.1.2. Dimensionless Free Surface Profile

For the analysis of the hydraulic jump free surface profile obtained from the numerical and physical models, a contrast with data from the bibliographic review was conducted. This contrast implied working with dimensionless profiles so that the comparison could be made. The dimensionless free surface profile was obtained from the output models' data, following the procedure presented by Hager [2]:

$$X = \frac{x - x_0}{L_r} \tag{25}$$

$$Y = \frac{y - y_1}{y_2 - y_1} \tag{26}$$

where X and Y are the dimensionless free surface profile coordinates and x_0 is the hydraulic jump toe position. The hydraulic jump roller length (L_r) value for each particular model is discussed in forthcoming sections. Once the dimensionless free surface profiles were calculated, they were represented in Figure 23, for their comparison with the CHJ dimensionless profiles presented by Bakhmeteff and Matzke [39] and Wang and Chanson [8].

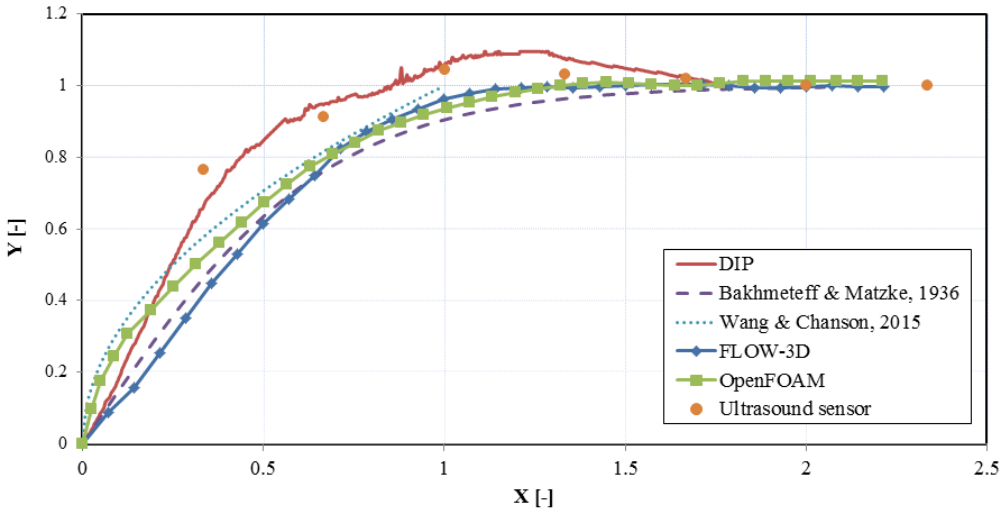

Figure 23. Classical hydraulic jump dimensionless free surface profile comparison. Profiles obtained in the numerical models (FLOW-3D® and OpenFOAM), in the physical model (DIP and ultrasound distance meter) and in the bibliographic review (Bakhmeteff and Matzke [39] and Wang and Chanson [8]).

The comparison presented in Figure 23 showed that both numerical models were able to accurately reproduce the classical hydraulic jump free surface profile, as their data mostly fell between the profiles obtained by Bakhmeteff and Matzke [39] and Wang and Chanson [8]. A deeper analysis of the profiles showed a slight overestimation of Y for $X > 1$ in the presented models, when compared to Bakhmeteff and Matzke [39]. However, this is in good agreement with previous results reported by Hager [2] and Bayón et al. [29]. The particular comparison between the two CFD codes showed similar free surface profile results. For low X values the free surface profile obtained with OpenFOAM increased faster than the one from FLOW-3D®. In these terms, the FLOW-3D® profile followed a similar trend to the one by Bakhmeteff and Matzke [39], whereas the one from OpenFOAM was closer to the profile by Wang and Chanson [8]. However, these differences were relatively small and, for $X > 0.7$ values, they almost disappeared and the profile from both CFD codes became almost coincident.

In regards with the dimensionless free surface profile resulting from the physical model, DIP techniques showed good agreement with the rest of the results despite, in general, this method tended to overestimate the flow depths. There are some reasons

that can explain the observed overestimation. On the one hand, the analysed phenomenon is characterised by free surface turbulences and air entrapment playing a significant role, with droplets and bubbles being continuously expelled. These elements could have influenced the digital image treatment causing bias, in spite of the filtering algorithms applied. On the other hand, whereas numerical models allowed determining the free surface profile along the longitudinal axis of the hydraulic jump, the characteristics of the DIP techniques forced to take images from the side of the experimental channel. Consequently, the free surface instant rotation around the X axis could have affected the results. In these terms, Bayón et al. [70] stated that the emergence of large bubbles through the surface and the formation of droplets in the roller region can affect the performance of DIP techniques in the determination of the hydraulic jump free surface profile. This happens since, in the image treatment process, the change of light intensity caused by droplets and bursting air pockets can be interpreted as the free surface position.

Regarding the results obtained with the ultrasound distance meter, they improved with the distance from the hydraulic jump toe, until achieving a high level of accuracy for the subcritical flow regime. Hence, it seems that high velocities, together with intense free surface turbulence, the presence of bubbles and droplet ejection also affected the performance of this device. In this case, masses of water expelled above the free surface position could have been captured by the acoustic signal sent from the device. Consequently, the ultrasound distance meter would have collected shorter distances between the sensor and the free surface, hence overestimating its position [70], [128]. Further research must be conducted to minimise the uncertainties observed for DIP techniques and the ultrasound sensor when measuring the hydraulic jump free surface profile.

In order to assess in detail the accuracy of the presented models in the determination of the free surface profile, the coefficient of determination R^2 [129] was calculated. In these terms, Table 9 shows the coefficient of determination for the profiles obtained with both numerical models in comparison with experimental results using DIP and with bibliographic results from Bakhmeteff and Matzke [39] and Wang and Chanson [8].

Table 9. Coefficient of determination ($\boldsymbol{R^2}$) for the dimensionless free surface profile obtained with the numerical models when compared to the physical model and theoretical expressions.

	DIP	**Bakhmeteff & Matzke** [39]	**Wang & Chanson** [8]
FLOW-3D®	0.943	0.991	0.956
OpenFOAM	0.961	0.996	0.996

Considering that $R^2 = 1$ indicates a perfect agreement, the results showed that the developed models were able to accurately reproduce the free surface profile of a classical hydraulic jump. The lowest values of R^2 were obtained in the comparison with the DIP profile which, as stated before, tended to overestimate the flow depths in the roller region. For the comparison with bibliographic data, OpenFOAM showed slightly higher R^2 values. Nevertheless, the differences were relatively small and the results obtained with both models can be considered satisfactory.

4.2. Hydraulic Jump Efficiency

The hydraulic jump efficiency (η) gives a measure of the amount of energy dissipated in the hydraulic jump. Consequently, it constitutes a feature of paramount importance regarding energy dissipation purposes in large-dam stilling basins. This efficiency was calculated for the numerical and physical models as:

$$\eta = \frac{H_{01} - H_{02}}{H_{01}} \tag{23}$$

where H_{01} and H_{02} are the specific energy heads upstream and downstream of the hydraulic jump respectively. As the supercritical and subcritical flow depths are directly involved in the calculation of the efficiency, different values were obtained for the physical model, depending on the experimental technique applied. In addition, the hydraulic jump efficiency was obtained with the expression proposed by Hager [2]:

$$\eta = \left(1 - \frac{\sqrt{2}}{Fr_1}\right)^2 \tag{24}$$

Table 10 shows the results of the comparison for hydraulic jump efficiency values, in terms of accuracy (Eq. 22).

Table 10. Accuracy of the CHJ efficiency obtained with the numerical models when compared to the physical model and theoretical expressions.

	η	**DIP**	**Ultrasound distance meter**	**Limnimeters**	**Hager** [2]
FLOW-3D®	0.590	96.1%	97.7%	97.7%	99.0%
OpenFOAM	0.588	96.4%	98.0%	98.0%	99.3%

The observed accuracies were very similar to the ones discussed for the sequent depths ratio. This was expectable since the hydraulic jump efficiency is strongly correlated with the sequent depths ratio. Therefore, the numerical models provided efficiency values similar to those of the physical model and the theoretical expression. Hence, for the numerical models, high levels of accuracy are obtained in general, although slightly lower values were observed for FLOW-3D®. Furthermore, the different experimental techniques used showed a good agreement among them and with the expression by Hager [2].

4.3. Roller Length

According to Hager et al. [48], the hydraulic jump roller determines the boundary between backward and forward flow, starting at the toe of the jump and ending at the surface stagnation point. Hence, this region encloses the biggest velocity and pressure fluctuations, together with the largest energy dissipation. Therefore, correct hydraulic jump roller length estimation is of utmost importance when designing energy dissipation structures. For the determination of the hydraulic jump roller length in the presented models, the stagnation point criterion, described in previous sections, was employed.

The resulting roller length values were compared with those obtained using different theoretical expressions. Hence, Hager et al. [48] carried out a detailed bibliographic review concerning hydraulic jump roller lengths, studied under different conditions. These authors proposed the following expression to calculate the roller length:

$$\begin{aligned} L_r &= y_1\left[-12 + 160\,tanh\left({Fr_1}/{20}\right)\right]\ for\ {y_1}/{b} < 0.10 \\ L_r &= y_1\left[-12 + 100\,tanh\left({Fr_1}/{12.5}\right)\right]\ for\ 0.10 < {y_1}/{b} < 0.70 \end{aligned} \quad (27)$$

More recently, Wang and Chanson [8] proposed an expression based on their observations for hydraulic jumps with a value of the inflow Froude number between 1.5 and 8.5. This range includes the hydraulic jump reproduced in the presented numerical and physical models ($Fr_1 = 6$):

$$L_r = y_1[6(Fr_1 - 1)] \tag{28}$$

The hydraulic jump roller length resulting values were 1.40 m, 1.59 m and 1.57 m for FLOW-3D®, OpenFOAM and the physical model respectively, whereas values of 1.63 m and 1.50 m were obtained using Eqs. (27) and (28). Table 11 displays these results in terms of accuracy (Eq. 22).

Table 11. Accuracy of the CHJ roller length obtained with the numerical models when compared to the physical model and theoretical expressions.

	Physical model	**Hager et al.** [48]	**Wang & Chanson** [8]
FLOW-3D®	89.2%	85.9%	93.3%
OpenFOAM	98.7%	97.5%	94.0%

The observation of the results showed that the model developed with FLOW-3D® slightly underestimated the hydraulic jump roller length. Consequently, OpenFOAM yielded generally higher accuracies. However, both models achieve an acceptable accuracy for this parameter. For the physical model, the roller length value is in the line of both, the numerical models and the theoretical expressions. Hence, the stagnation point criterion applied using DIP and Pitot tube data seems to be adequate.

4.4. Velocity Profiles

4.4.1. Velocity Distribution in the Roller Region

The analysis of the velocity field in the classical hydraulic jump roller region constitutes a complex task, as a result of the intense turbulent fluctuations and the interference of aeration, particularly relevant in this zone. The analysis was conducted in the present research through a series of streamwise velocity vertical profiles obtained in the numerical FLOW-3D® and OpenFOAM models, as well as in the physical model.

It is important to highlight that, despite the large number of points measured for each profile in the physical model, the results provided a discrete and not a continuous profile. Furthermore, several tests conducted in the experimental channel, with the Pitot tube placed in a reverse position, showed that this device was not able to capture backwards velocities in the roller. Other instrumentation available, such as the ADV, could not be used to replace the Pitot tube in this task, since the intense air entrainment in the roller had a severe affection on the results. However, the backwards velocities could not be excluded from the analysis of the velocity profiles in the roller region. For the numerical models, these issues were not as relevant as for the physical model. Nevertheless, it was still not possible to obtain completely continuous velocity profiles. This would have implied very refined meshes and large volumes of data, which exceeded the available computational capacities.

Hence, in order to overcome the presented issues and to achieve continuous velocity profiles, the analytical expression proposed by McCorquodale and Khalifa [47] was adjusted to the information obtained from the physical and the numerical models. This expression represents the mean velocity distribution within a classical hydraulic jump roller by using two different functions, which distinguish between the inner and the outer layer:

$$u = u_{max}\left(\frac{z}{\delta}\right)^{1/7} \; ; \; 0 \leq z \leq \delta \tag{29}$$

$$u = u_{\infty} + u_t e^{2.772(z-\delta/y-\delta)^2} \; ; \; \delta < z < y \tag{30}$$

where u is the streamwise velocity, u_{max} is the maximum streamwise velocity, which takes place at a height $z = \delta$, u_{∞} is the horizontal component of the freestream velocity and $u_t = u_{max} - u_{\infty}$. Figure 24 exemplifies the results of the adjustment process described.

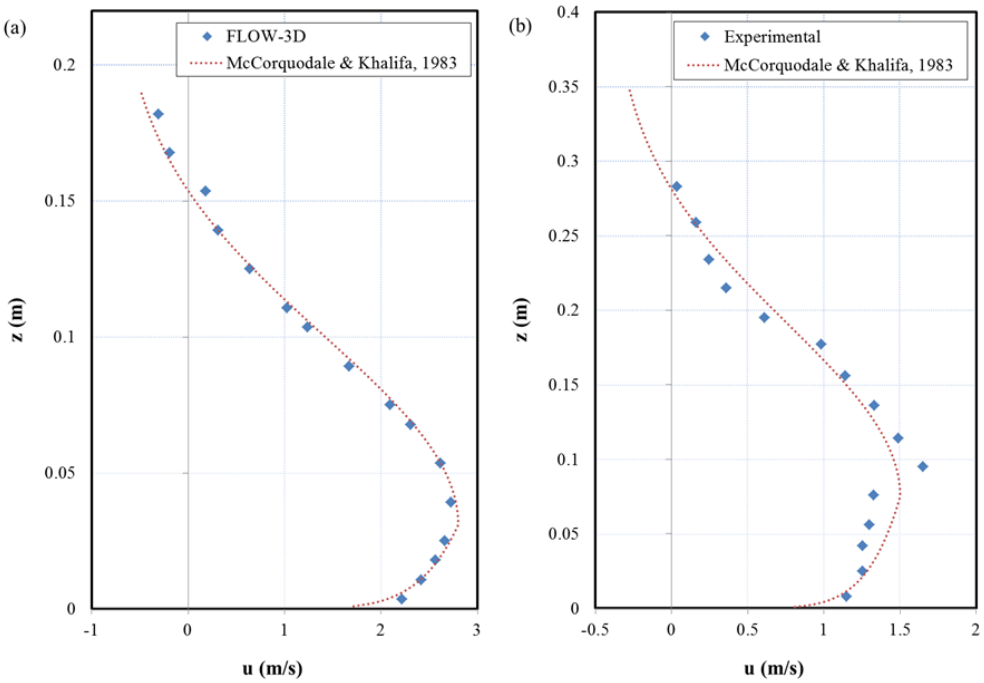

Figure 24. Vertical velocity profiles within the hydraulic jump roller region. Adjustment with the expression by McCorquodale & Khalifa [47]: (a) FLOW-3D® profile at $\boldsymbol{X} = 0.46$, (b) Experimental profile at $\boldsymbol{X} = 0.76$.

This process, applied to the different velocity profiles extracted for the numerical and physical models along the roller region, allowed obtaining the maximum forward velocity decay from the hydraulic jump toe (Figure 25 (a)) together with the maximum backwards velocities (Figure 25 (b)). In order to compare this information with the results presented by Hager [2], dimensionless values were obtained as:

$$U_{max} = \frac{u_{max} - u_2}{u_1 - u_2} \tag{31}$$

$$U_S = \frac{u_s}{u_2} \tag{32}$$

where u_{max} and u_s are the maximum and the maximum backwards velocities for each profile, whereas u_1 and u_2 are the supercritical and subcritical mean flow velocities.

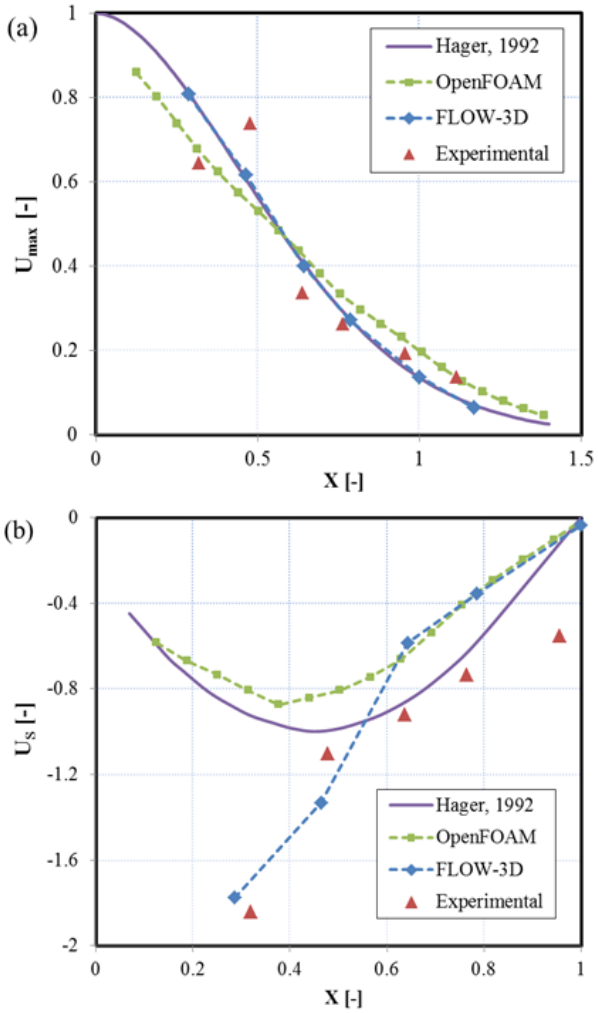

Figure 25. Velocity analysis in the hydraulic jump roller region comparing results from FLOW-3D®, OpenFOAM, physical model and Hager [2]: (a) Maximum forward velocity decay, (b) Maximum backwards velocities.

The results displayed in Figure 25 (a) show that the maximum velocity decay from the hydraulic jump toe followed a similar trend in OpenFOAM and FLOW-3D®, which was in good agreement with the expression proposed by Hager [2]. In particular the velocity decay obtained with FLOW-3D® was almost coincident with the bibliographic data, showing a faster decrease in the maximum velocity values as the profile moves

downstream the hydraulic jump toe. The coefficient of determination (R^2) was 0.999 for FLOW-3D® and 0.992 for OpenFOAM, when compared to Hager [2]. In regards with the results obtained from the experimental device, the general trend was in the line of the numerical and the bibliographic data. However, the results showed a higher degree of variability, especially for positions close to the jump toe. This variability was likely due to the possible bias suffered by the Pitot tube in the swirling region of the hydraulic jump.

For the maximum backwards velocities, the differences between the models and the results reported by Hager increased (Figure 25 (b)), probably as a consequence of the complex flow taking place in the area with recirculation. The coefficient R^2 was 0.928 for OpenFOAM and 0.618 for FLOW-3D® in comparison with Hager's results [2]. In these terms, FLOW-3D® followed a trend closer to that observed for the experimental results, with bigger magnitudes of backwards velocities close to the hydraulic jump toe. For $X > 0.5$, the differences among models and bibliographic results decreased and they started to share similar trends.

The vertical velocity profiles obtained with the numerical and the physical models were also analysed separately and compared to the expression presented by Hager [2] for the diffusion portion of velocity profiles in the hydraulic jump roller region:

$$U = [cos(100Z)]^2 \tag{33}$$

To do so, dimensionless values were calculated following the process proposed by Hager [2]:

$$Z = \frac{z-\delta}{y-\delta} \tag{34}$$

$$U = \frac{u-u_s}{u_{max}-u_s} \tag{35}$$

where, for each particular vertical profile, z is the position, y is the flow depth, u_{max} and u_s are the maximum and the maximum backwards velocity and δ is the position at which $u = u_{max}$. Figure 26 shows the results of this analysis.

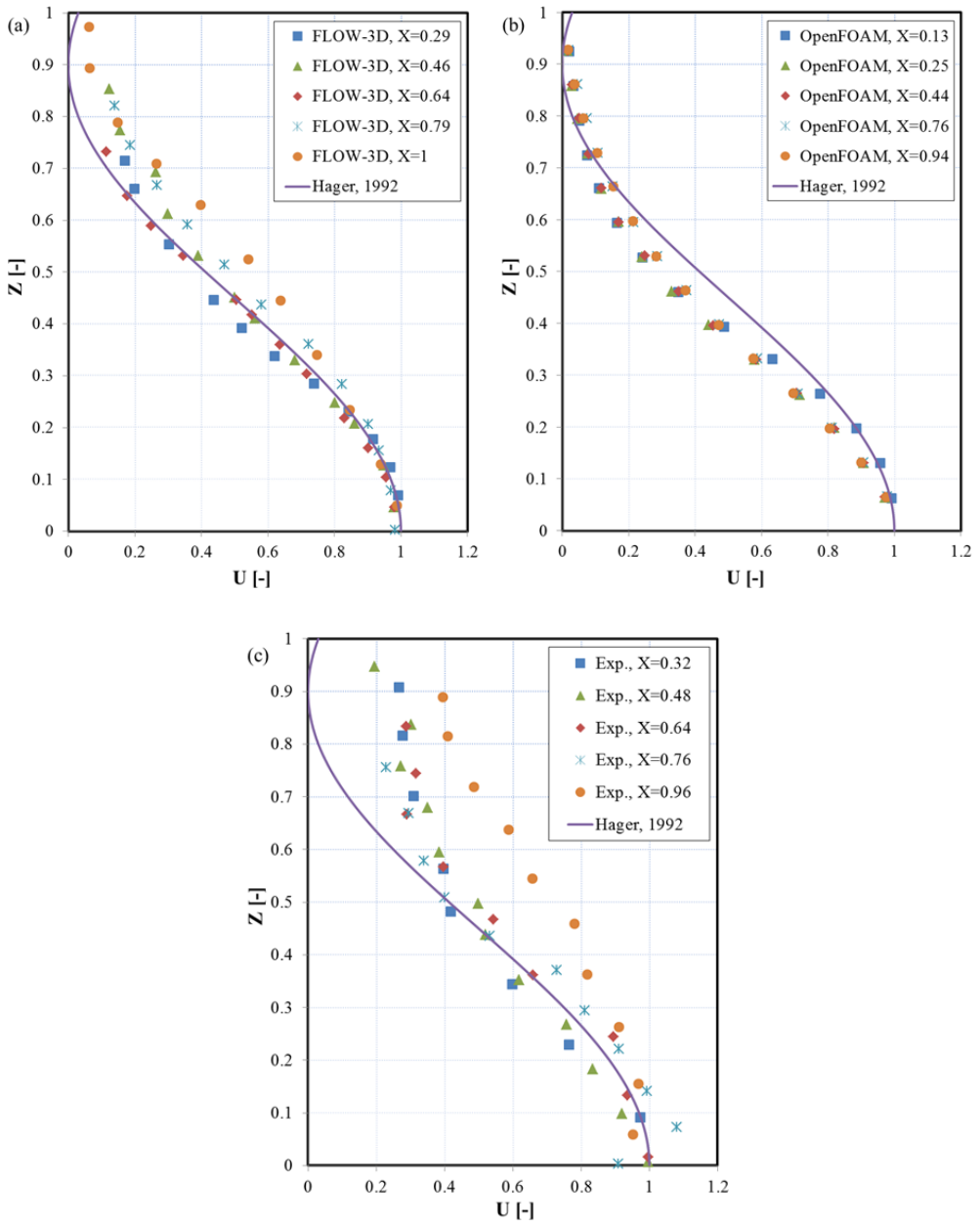

Figure 26. Vertical velocity profiles obtained along the hydraulic jump roller region longitudinal axis and comparison with the expression proposed by Hager [2]: (a) FLOW-3D®, (b) OpenFOAM, (c) Experimental.

A general observation of the results displayed in Figure 26 shows that both CFD models (Figure 26 (a) and (b)) were able to reproduce the velocity profiles within the classical hydraulic jump roller in good agreement with the expression proposed by Hager [2]. A deeper insight showed that, for FLOW-3D® (Figure 26 (a)), profiles increased their differences with the theoretical expression as they approached the end of the hydraulic jump roller ($X = 1$), where the velocity distribution proposed by Hager (Eq. 33) [2] may not be strictly followed, due to the proximity of the subcritical flow. In spite of this, a high level of accuracy was observed, with results almost coincident with the bibliographic expression, at least until $Z = 0.6$. For larger Z values, although the results still showed a satisfactory agreement with the expression by Hager [2], the differences slightly increased. This result implies that the ability showed by FLOW-3D® to accurately reproduce the velocity field within the jump roller, diminished as the profiles approached the free surface. This is precisely the zone where backwards velocities gain importance, a fact that basically explains the differences found in Figure 25 (b) between FLOW-3D®, OpenFOAM and the bibliographic results. The analysis of the OpenFOAM results (Figure 26 (b)) shows that there was a good agreement among all of the analysed profiles, regardless of their position along the roller. However, OpenFOAM provided slightly steeper decay for the velocity values, as they approached the free surface, in comparison with the bibliographic results [2]. A quantitative assessment of the accuracy provided by both models, using the coefficient of determination R^2, was conducted. To do so, the coefficient R^2 was calculated for each profile and the mean value for each code was then obtained. The results showed that both models were capable to successfully reproduce the velocity field within the jump roller. In particular, FLOW-3D® achieved the highest R^2 value (0.988), closely followed by OpenFOAM (0.978).

In regards with the experimental values (Figure 26 (c)), higher differences in the comparison with the expression by Hager [2] were observed. Firstly, as explained for FLOW-3D®, the profile with the highest X value did not strictly follow the expression presented in Eq. 33, probably because of its proximity to the end of the roller region. For the rest of the profiles, in spite of the general good agreement observed for low Z values, the differences increased for $Z > 0.5$. The most probable explanation to such observed differences mainly concerns Pitot tube measurements reliability. It can be considered satisfactory in the bottom area of the jump, where air concentrations are relatively low, but it clearly decreases significantly inside the highly aerated region, close to the free surface [9]. This explanation is in the line of the observations made for

Figure 25 (b), considering that the highest presence of bubbles within the hydraulic jump is generally associated to those areas where the maximum backwards velocities take place. Despite the differences discussed, the experimental results reached a R^2 value of 0.962, when compared to Eq. 33, showing that the experimental campaign conducted in the physical model was able to capture the vertical velocity profiles within the jump roller.

4.4.2. Velocity Profiles in the Supercritical and Subcritical Flow Regimes

The study of the velocity field was extended to the supercritical and subcritical flow regimes, where several streamwise velocity vertical profiles were measured. Hence the flow upstream and downstream the hydraulic jump was also covered. As stated in previous sections regarding the experimental campaign, profiles in the subcritical regime were measured using the Acoustic Doppler Velocimeter (ADV), whereas for the supercritical regime the Pitot tube was employed, due to the high velocities reached and the presence of bubbles.

The analysis of the supercritical and the subcritical velocity profiles obtained from the numerical and physical models was conducted through a comparison with the analytical expression for open channel flow proposed by Kirkgoz and Ardiclioglu [130]:

$$\frac{u}{u^*} = 2.5 \cdot ln\left(\frac{zu^*}{\nu}\right) + 5.5 \tag{36}$$

where u^* is the shear velocity calculated as:

$$u^* = \sqrt{\frac{\tau_0}{\rho_w}} \tag{37}$$

$$\tau_0 = \gamma_w R_H I \tag{38}$$

$$Q = (y \cdot b)\frac{1}{n} R_H^{2/3} I^{1/2} \tag{39}$$

where τ_0 is the wall shear stress, γ_w is the water specific weight, R_H is the hydraulic radius, I is the linear hydraulic head loss and Eq.39 is the well-known Manning formula for open channel flow, in which n is the Manning coefficient. The value of the Manning coefficient depends on the materials of the channel. In the present research

the employed values were 0.010 for the walls (glass) and 0.007 for the streambed (PVC). The results of the analysis are presented in Figure 27. In order to organise the results, normalised values were represented in this figure:

$$Z = \frac{z}{y_1} \; ; \; Z = \frac{z}{y_2} \tag{40}$$

$$U = \frac{u}{u_{max}} \tag{41}$$

where u_{max} is the maximum streamwise velocity for each profile. Furthermore, the supercritical (y_1) and the subcritical (y_2) flow depths were used depending on the corresponding flow regime of the analysed profile (Eq. 40).

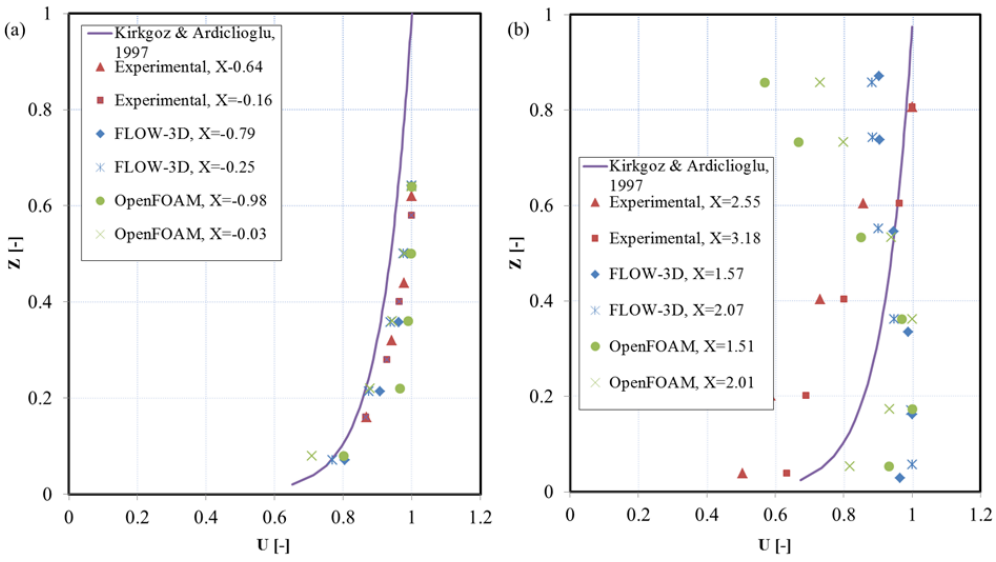

Figure 27. Vertical velocity profiles for the numerical and physical models and comparison with the expression proposed Kirkgoz and Ardiclioglu [130]: (a) Supercritical flow regime, (b) Subcritical flow regime.

The analysis of the results showed that, in terms of magnitude, the values coming from both numerical models and from the physical model were around the expected results, according to the expression by Kirkgoz and Ardiclioglu [130]. On the one hand, for the supercritical regime, the results displayed in Figure 27 (a) showed that there was a general good agreement in the trends. OpenFOAM provided a faster increase of the

velocity magnitude from the streambed, whereas this increase for FLOW-3D® was closer to the one showed by the experimental results and the analytical expression (Eq. 36). Thus, the coefficient of determination R^2 for the comparison with this expression was 0.981 for FLOW-3D® and 0.903 for OpenFOAM. On the other hand, for the subcritical regime (Figure 27 (b)), the trends observed for both numerical models seemed to differ from the rest of the results. This was probably due to the proximity of the analysed sections to the hydraulic jump roller (relatively low X values). Thus, the roller affected these velocity profiles, so that they were closer to bibliographic expressions employed for velocity profiles in this region, such as the previously referred Hager [2] velocity profile (Eq. 33). Profiles with X values not far from the end of the roller were analysed in the numerical models because of the downstream boundary condition. This condition affected the velocity distributions of the nearby sections. Therefore, profiles closer to the end of the roller were used in the analysis. In order to confirm this explanation, the subcritical regime velocity profiles obtained with FLOW-3D® and OpenFOAM were compared in Figure 28 with the expression proposed by Hager [2], following the procedure already employed for Figure 26.

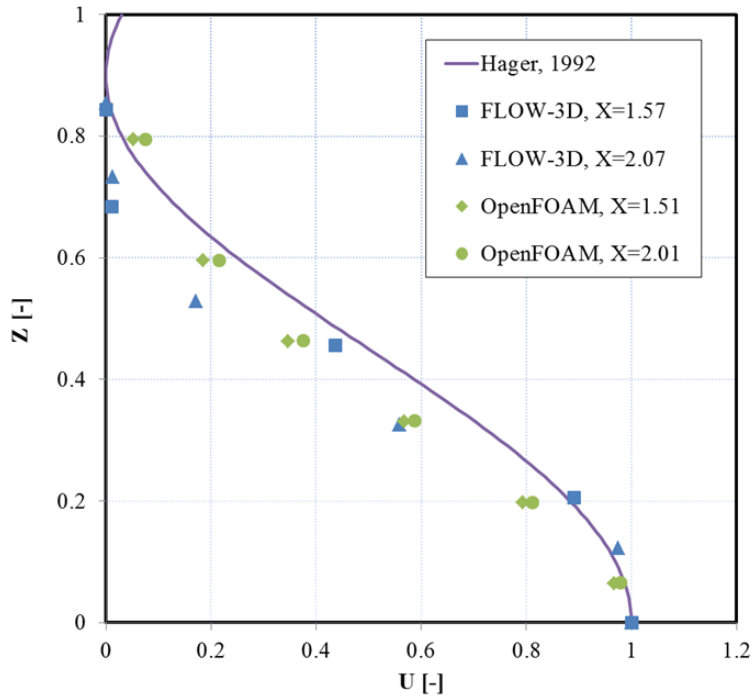

Figure 28. Vertical velocity profiles obtained in the subcritical flow regime for FLOW-3D® and OpenFOAM and comparison with the expression proposed by Hager [2] for the hydraulic jump roller region.

Figure 28 shows that the profiles obtained for FLOW-3D® and OpenFOAM were closer to the analytical expression for the hydraulic jump roller (Eq. 33) than to the one for the subcritical regime (Eq. 36). In particular, the coefficient R^2 was 0.979 for FLOW-3D® and 0.973 for OpenFOAM, in comparison with the expression by Hager [2], whereas these values fell below 0.5 in the comparison with the expression by Kirkgoz and Ardiclioglu [130].

These results can also be interpreted in terms of the hydraulic jump length (L_j). The identification of this parameter is difficult and many methods have been discussed concerning its determination [12]. Some authors stated that the analysis of the velocity field could help in this determination. Bayón et al. [29] pointed out the possibility of using the velocity profile in the section for the practical determination of the hydraulic jump end section. Moreover, Hager [2] referred to the consideration of the section

where gradually varied flow conditions reappear to estimate the hydraulic jump end location.

In the presented research, the velocity profile with the highest X value obtained with the numerical models ($X = 2.07$) followed the expression for the velocity profiles in the roller (Eq. 33). In contrast, the experimental profile measured in the subcritical regime with the lowest value of X (i.e. X =2.55) was in good agreement with the expression by Kirkgoz and Ardiclioglu [130] for open channel flow (Eq. 36). Considering that the dimensionless value X was obtained using Eq. 25, the length of the modelled hydraulic jump was approximately 2.0-2.5 times the roller length. This criterion led to a hydraulic jump length above the 3 m, which clearly overestimated the value obtained with the expression proposed by Hager [2] for hydraulic jumps with Fr_1 values between 4 and 12:

$$L_j = y_1 \cdot 220 \cdot tanh\left(\frac{Fr_1}{22}\right) \tag{42}$$

However, several qualitative observation criteria applied in the experimental campaign, such as the development of a horizontal free surface or the full deaeration of the flow supported the resulting hydraulic jump length above the 3 m found for the presented case study. These criteria were gathered by Valero et al. [12] in their review of bibliographic procedures for the determination of the hydraulic jump length.

To sum up, the present research clearly showed larger hydraulic jump lengths than those obtained by bibliographic expressions. To do so, this parameter was approached through the analysis of the velocity field and through qualitative criteria too. The determination of the hydraulic jump length is of utmost importance regarding stilling basins design. Consequently, the results here presented should undoubtedly be considered for further research, seeking for confirmation of the differences found.

4.5. Streambed Pressures

The analysis of the streambed pressures was conducted for the numerical and the physical models. To do so, average relative pressures values were collected along the hydraulic jump longitudinal axis. These results are represented in Figure 29 (a), together with observations from Toso and Bowers [49] for a classical hydraulic jump with $Fr_1 = 5.67$ (i.e. very close to the studied CHJ with $Fr_1 = 6$). Apart from this

averaged pressure values, pressure fluctuations were also analysed as a characteristic closely related to the turbulent nature of the hydraulic jump (Figure 29 (b)). This analysis was conducted following the procedure presented by Abdul Khader and Elango [44] in their research for hydraulic jumps with Fr_1 values of 4.7, 5.9 and 6.7. In these terms, pressure instant values were decomposed into: $p = \bar{p} + p'$, where $\bar{p}$ is the average pressure value and p' the instant fluctuating component. From this decomposition process, pressure fluctuations (P/P_m) were obtained as:

$$P = \frac{\sqrt{p'^2}}{\rho u_1^2/_2} \tag{43}$$

$$P_m = a(1 + aFr_1) \tag{44}$$

where $a = 0.061$ for Fr_1 values between 4.7 and 6.6.

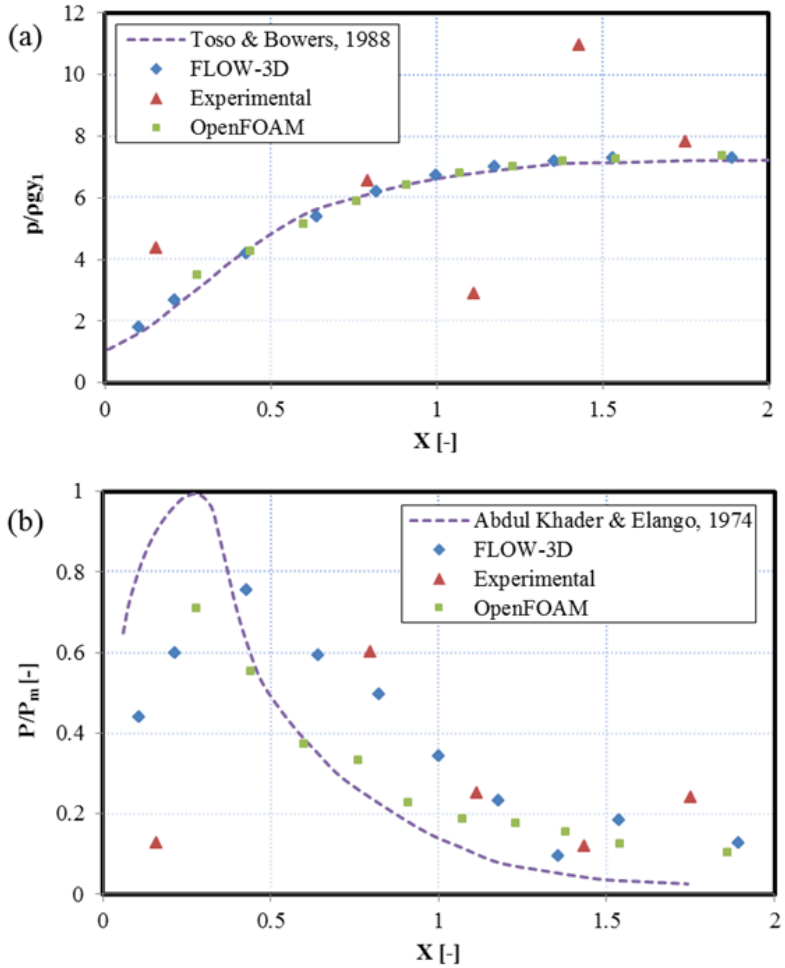

Figure 29. Streambed pressures analysis along the classical hydraulic jump for the numerical and the physical models: (a) Average relative pressures and comparison with data from Toso and Bowers [49], (b) Pressure fluctuations and comparison with data from Abdul Khader and Elango [44].

The results displayed in Figure 29 (a) show that both CFD codes were able to reproduce the averaged streambed pressures in the hydraulic jump, achieving an almost coincident agreement with the results presented by Toso and Bowers [49]. Thus, the comparison between this bibliographic information and the numerical models led to values for the coefficient of determination (R^2) of 0.995 for FLOW-3D® and 0.958 for OpenFOAM. In contrast, the experimental values obtained from the physical model

showed a high variability, making it difficult to identify trends or similarities with the numerical and bibliographic results. The performance of the pressure transmitters could have been affected by the presence of suspended solid particles in the flow, which were observed during the experimental campaign. To this end, it should be outlined the large sensitivity of such devices to this kind of particles which, apart from severely affecting the results, can also disable the transmitters permanently.

For the pressure fluctuations presented in Figure 29 (b), the general trends followed by the numerical and the physical model were close to the one observed by Abdul Khader and Elango [44]. Hence, the results showed a fluctuation peak not far from the hydraulic jump toe and then, the fluctuations decreased for further positions. Despite the good agreement found for the trend, both FLOW-3D® and OpenFOAM, showed a lower value for the peak fluctuations than the results from Abdul Khader and Elango [44], followed by a slightly slower decrease of these fluctuations for $X > 0.5$. This slower decrease, with fluctuation values above those presented by Abdul Khader and Elango, was in good agreement with the results presented by Akbari et al. [131] for a hydraulic jump with $Fr_1 = 6.2$. Regarding the location of the peak pressure fluctuations, FLOW-3D® results were close to the observations made by Toso and Bowers [49], which established this peak location for X values around 0.4. Alternatively, OpenFOAM is in the line of other bibliographic studies such as the research conducted by Spoljaric [132] and Abdul Khader and Elango [44], which indicated an X position for the peak pressure fluctuations between 0.3 and 0.35.

A series of measures were also taken with the pressure transmitters in the supercritical and the subcritical flow, far from the hydraulic jump roller region. The streambed pressure information collected for these positions showed around two or three times less variability, in terms of the standard deviation, than the data for the hydraulic jump roller region. These results clearly confirm the intensification of turbulence and pressure fluctuations associated to the hydraulic jump roller.

Finally, the ability of the developed numerical models to represent the most relevant features of a classical hydraulic jump was summarised and presented in Table 12. Hence, the performance of the models was assessed by comparing them with experimental and bibliographic results.

Table 12. Summary table. Capability of the developed numerical models to characterise the classical hydraulic jump in terms of accuracy and coefficient of determination, $\boldsymbol{R^2}$, when compared to experimental and bibliographic results.

Variable	**Referred to**	**FLOW-3D®**	**OpenFOAM**	**Compared to**
Sequent depths ratio	Accuracy	94.2%	94.7%	Exp. (DIP)
		96.4%	96.9%	Exp. (Limnimeters)
		96.4%	96.9%	Exp. (Ultrasound)
		96.5%	97.0%	Hager & Bremen [23]
Hydraulic jump efficiency		96.1%	96.4%	Exp. (DIP)
		97.7%	98.0%	Exp. (Limnimeters)
		97.7%	98.0%	Exp. (Ultrasound)
		99.0%	99.3%	Hager [2]
Roller Length		89.2%	98.7%	Experimental
		85.9%	97.5%	Hager et al. [48]
		93.3%	94.0%	Wang & Chanson [8]
Free surface profile	R^2	0.943	0.961	Exp. (DIP)
		0.991	0.996	Bakhmeteff & Matzke [39]
		0.956	0.996	Wang & Chanson [8]
Maximum velocity decay		0.872	0.868	Experimental
		0.999	0.992	Hager [2]
Maximum backwards velocities		0.858	0.754	Experimental
		0.618	0.928	Hager [2]
Velocity profiles in the roller		0.988	0.978	Hager [2]
Subcritical velocity profiles		0.979	0.973	Hager [2]
Supercritical velocity profiles		0.981	0.903	Kirkgoz & Ardiclioglu [130]
Streambed pressures		0.995	0.958	Toso & Bowers [49]

4.6. Time Analysis

The study of how certain classical hydraulic jump features follow patterns repeated in a periodic fashion was also addressed in the present research. As stated by Bayón et al.

[29], the oscillations of certain hydraulic jump characteristics in the time domain occur in a quasi-periodic fashion. This periodicity holds a great interest for the determination of the time-averaging window that must be used to achieve a successful analysis of the hydraulic jump phenomenon and its characteristic features (section 2.8).

A frequency analysis of the hydraulic jump was carried out using the Fast Fourier Transform (FFT). In particular, data regarding the subcritical flow depth (y_2) extracted from the developed numerical models (FLOW-3D® and OpenFOAM) was transformed from the temporal to the frequency domain. Thus, the analysis allowed capturing the periods for the observed quasi-periodic oscillations. In addition, the Power Spectrum Density (PSD) of the selected variable provided the resulting dominant frequencies for each of the CFD codes (Figure 30 (a)). In order to contrast the results of the frequency analysis, they were compared with bibliographic information in terms of the Strouhal number (Figure 30 (b)), which is employed for the description of oscillating flow mechanisms:

$$St_i = f\frac{y_i}{u_i} \tag{45}$$

where f is the dominant frequency.

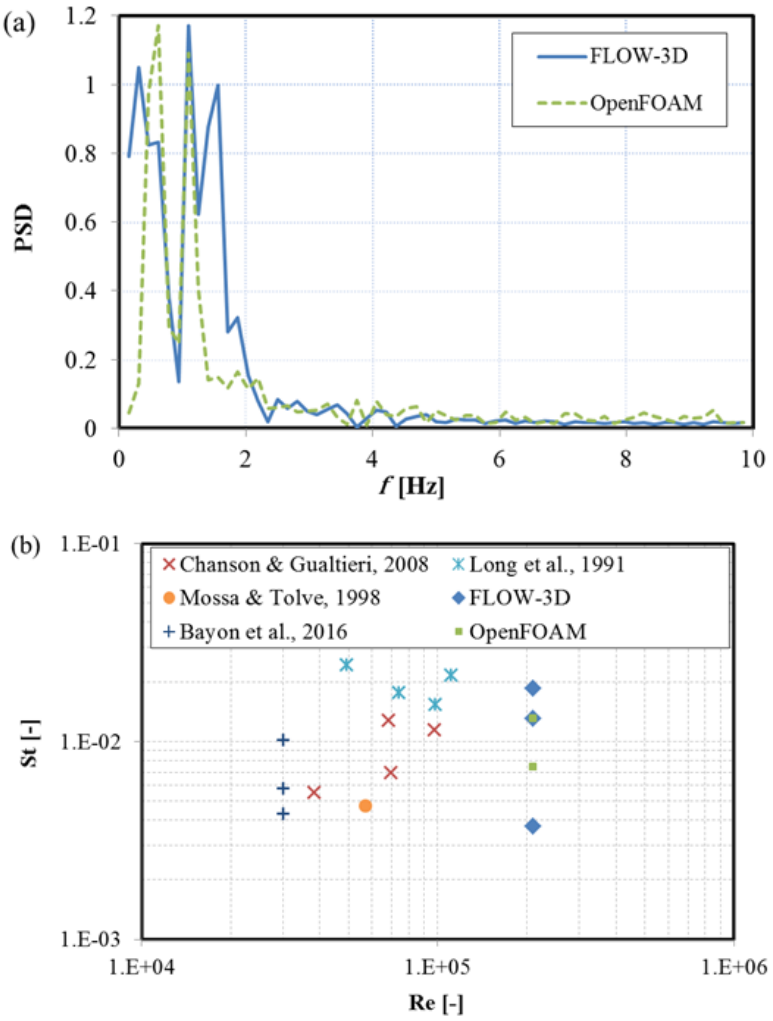

Figure 30. Frequency analysis in the classical hydraulic jump: (a) Power Spectrum Density (PSD) of the subcritical flow depth for the numerical models, (b) Strouhal number compared to the Reynolds number for the numerical models and bibliographic studies.

The observation of Figure 30 (a) showed that both, for FLOW-3D® and for OpenFOAM, there was not a clear, unique dominant frequency. Instead of this, three and two peaks were observed respectively in the PSD for these numerical models. The frequency values for which these peaks take place showed that the time-averaging window size chosen (10 s), was able to capture several characteristic oscillation periods

of the analysed variable. This choice, consequently, was adequate to avoid potential bias in the time averaging process performed [29].

These peaks were considered as dominant frequencies and allowed obtaining the results plotted in Figure 30 (b). In these terms, the Strouhal number seemed to follow the general trend observed in the bibliographic information, with certain correlation to the Reynolds number. Furthermore, as agreed by Bayón et al. [29], the similar dominant frequency values obtained for both models suggested that the regularity of the oscillating characteristics can be described as a non-random and orderly process. Hence, the RANS modelling approach was able to reproduce the unsteadiness typical of hydraulic jumps [28]. However, it is important to highlight that the RANS approach used for the presented numerical models is unsteady. The unsteady RANS approach is time-dependent, implying that the turbulence was not directly simulated. Instead of that, only the statistic properties of the flow were accounted for [133]. Consequently, any conclusion regarding turbulent fluctuations should be carefully considered.

Chapter 5. Analysis of the Typified USBR II Stilling Basin

The analysis conducted to assess the performance of the typified USBR II stilling basin is developed in this chapter. An in-depth study of the hydraulic jump occurring in this stilling basin was carried out, focusing on a series of crucial features such as the sequent depths ratio, the hydraulic jump efficiency, the roller length, the free surface profile, the velocity and void fraction distributions and the pressure on the energy dissipation devices.

Previous to the detailed analysis, a qualitative observation of the results is addressed. Both, the physical and the numerical model were able to provide a physically-consistent hydraulic jump, placed in the desired position within the case study geometry [5]. Hence, a series of macroscopic features bound to the hydraulic jump nature, such as the intense turbulence and air entrainment in the roller region, can be identified in the presented models (Figure 31).

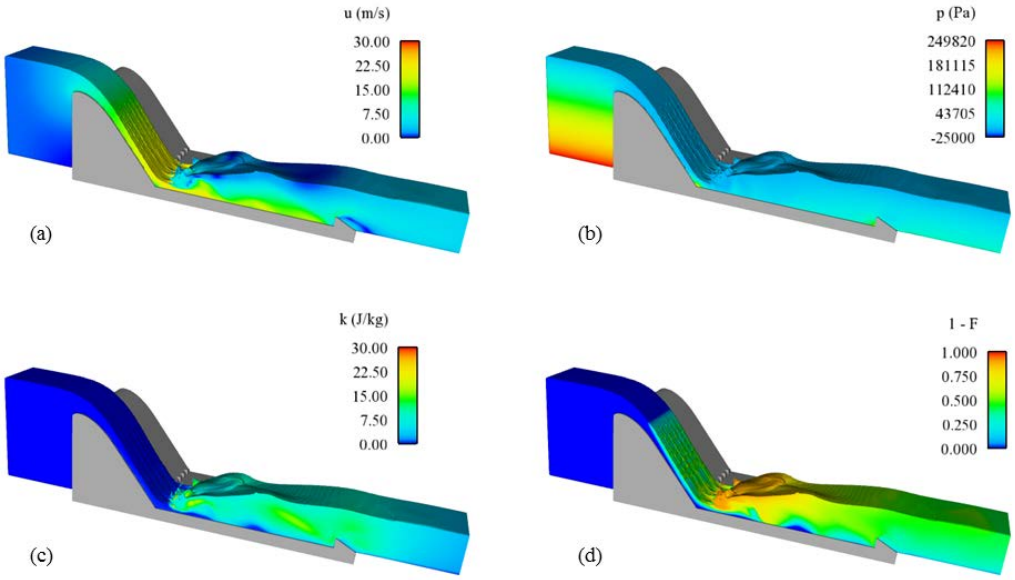

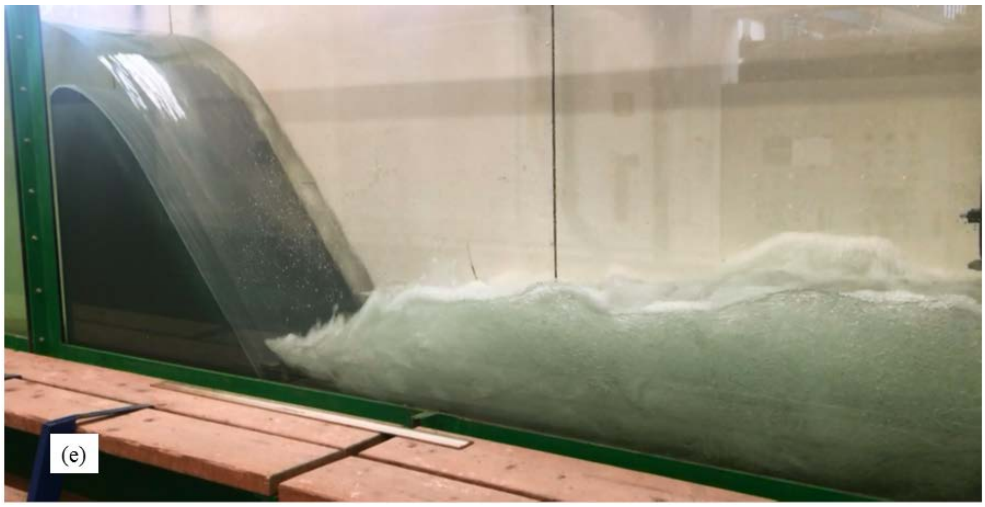

Figure 31. Typified USBR II stilling basin numerical model using FLOW-3D®: (a) Velocity field, (b) Pressure field, (c) Turbulent kinetic energy, (d) Volume fraction of entrained air expressed in terms of the Fraction of Fluid function (***F***), (e) Typified USBR II stilling basin physical model in the Hydraulics Laboratory of the Institute of Hydraulic Engineering and Water Resources Management, at the Technische Universität Wien (TUWien, Austria).

Once both, the numerical and the physical model were developed, a preliminary analysis of their performance regarding some basic variables was carried out. This analysis, summarised in Table 13, allowed comparing the models' outputs with the expected results, coming from the theoretical design of the case study.

Table 13. Basic flow variables for the numerical and physical models (TUWien) [5].

Model	Supercritical flow depth (y_1) (m)	Subcritical flow depth (y_2) (m)	Unit discharge (q) (m^2/s)	Inflow Froude number (Fr_1)
Numerical model	1.520 m	9.500 m	29.143 m^2/s	4.97
Physical model	0.061 (1.525)[1]	0.370 (9.250)[1]	0.233 (29.143)[1]	4.94

[1] In parenthesis: values at prototype scale applying the scale factor (1:25).

The results in Table 13 showed good agreement between both models, with a similar Froude number for the flow entering the stilling basin. However, the comparison of these results with the theoretical design of the case study (Figure 11 and Table 5)

showed that the modelled reservoir water level and the designed spillway led to a slightly higher than expected supercritical flow depth which, in turn, provided a lower inflow Froude number. As explained in previous sections, despite the observed differences, the modelled results fulfilled all the requirements to study energy dissipation in a typified USBR II stilling basin [6], [17]. Therefore, the analysis of these results was conducted without compromising the potential conclusions of the research.

Nevertheless, in order to extend the comparison sources for the analysis and cover higher inflow Froude numbers, a second typified USBR II stilling basin physical model was developed in the Hydraulics Laboratory of the Department of Hydraulic Engineering and Environment at the Universitat Politècnica de València (UPV, Spain) (Table 6 and Figure 14). The Fr_1 value achieved for this model was 9.02. Hence the analysis presented herein involved a FLOW-3D® numerical model at prototype scale, a reduced scale physical model (TUWien) of this prototype case study and a second physical model (UPV) covering different inflow conditions.

5.1. Free Surface Profile

5.1.1. Sequent Depths Ratio

The sequent depths ratio was obtained for the presented models, taking the flow depth in the spillway right before the entrance to the stilling basin as y_1. The values provided by the numerical and physical models were compared with the value obtained using the theoretical expression proposed by Hager and Bremen [23] for classical hydraulic jumps (Eq. 21). This comparison, in terms of accuracy (Eq. 22) is presented in Table 14.

Table 14. Sequent depths ratio for the hydraulic jump in the USBR II basin obtained with the numerical and physical models and with the theoretical expression by Hager and Bremen [23].

	Sequent depths ratio	**Hager & Bremen** [23]
Numerical model	6.25	6.32 (98.8%)[1]
Physical model (TUWien)	6.07	6.15 (98.7%)[1]
Physical model (UPV)	12.00	12.17 (98.6%)[1]

[1] In parenthesis: accuracy of the modelled values obtained using Eq. 22.

In this particular case, apart from focusing on the accuracies, which showed that the presented models were able to provide a sequent depth ratio close to the one achieved for a CHJ with the same characteristics, it is interesting to analyse the magnitude of this ratio. Hence, with the expression by Hager & Bremen [23], and using each case study inflow conditions, the sequent depths ratio values would have been 6.32 for the numerical model, 6.15 for the physical model (TUWien) and 12.17 for the second physical model (UPV). This means that the stilling basin models provided lower sequent depth ratios than the ones obtained with the expression for a CHJ. These lower values were expected for a stilling basin in which the energy dissipation devices affect the subcritical flow depth [77], [83]. The differences in the sequent depths ratio magnitude found for the physical model (UPV) in comparison with the other presented models were due to the different inflow conditions (i.e. higher Fr_1).

In these terms the ratio y_2/y_2^* was analysed, where y_2 is the subcritical depth obtained in the models and y_2^* is the subcritical depth calculated using the Bélanger [33] equation:

$$\frac{y_2^*}{y_1} = \frac{1}{2}\left(\sqrt{1 + 8Fr_1^2} - 1\right) \tag{46}$$

This expression was applied considering the particular conditions of each case study and the corresponding results were displayed in Table 15.

Table 15. Subcritical flow depths obtained from the numerical and physical models and from Bélanger's theoretical expression [33].

	y_2 (m)	y_2^* (m)	y_2/y_2^*
Numerical model	9.50	9.94	0.96
Physical model (TUWien)	0.37	0.40	0.93
Physical model (UPV)	0.36	0.37	0.97

In accordance with Peterka [6], the ratio y_2/y_2^* should fall in the range 0.6-1.0 for hydraulic jumps in stilling basins, which was accomplished by the presented models. Furthermore, Padulano et al. [83], in their research for USBR II basins, proposed a value of 0.83 for the ratio. Although the presented models reached results not far from the value presented by Padulano et al. [83], a slight overestimation was observed. This overestimation means that a lower influence of the energy dissipation devices on the

subcritical depth was obtained for the presented models, in comparison with the bibliographic observations. However, it must be considered that Padulano et al. [83] conducted their research for relatively high Froude numbers (Fr_1 values between 8.41 and 31.36), in order to establish the trend that led to the 0.83 ratio. This could partially explain the observed differences since the presented models are either close to the lower boundary or out of the range analysed by Padulano et al. [83].

5.1.2. Dimensionless Free Surface Profile

The analysis of the free surface profile for the presented models involved different techniques and particularities. Before starting with the comparison, the information collected with LIDAR techniques in the typified USBR II stilling basin physical model at UPV was specifically treated. The procedure allowed discarding anomalous values and outliers caused by splashing and droplets by providing a series of bands containing a particular percentage of the collected points along the model longitudinal axis. Figure 32 shows the lower and upper boundaries of these bands for different percentages.

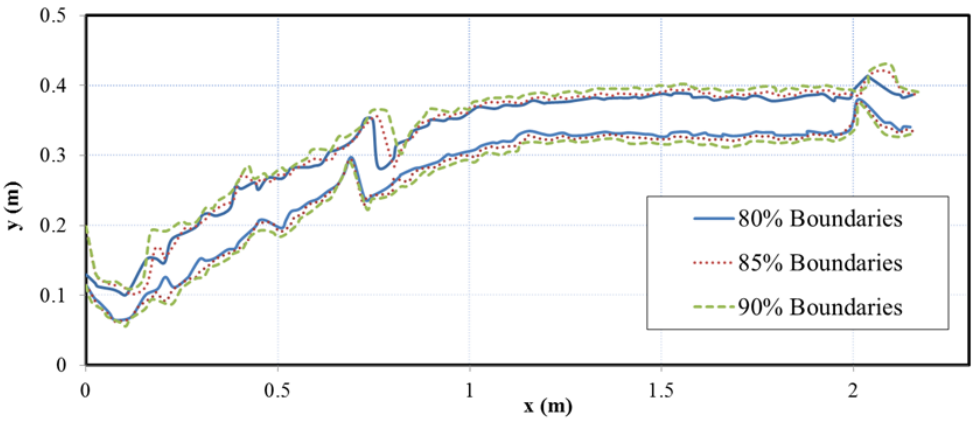

Figure 32. Bands containing the 80, 85 and 90% of the points collected with LIDAR for the free surface profile determination in the typified USBR II stilling basin physical model in the Hydraulics Laboratory of the Department of Hydraulic Engineering and Environment at the Universitat Politècnica de València (UPV, Spain).

The similarity observed for the different bands in Figure 32 showed the consistency offered by LIDAR techniques in the determination of the hydraulic jump free surface profile. Consequently, the information collected was used to obtain the mean free surface profile. However, the characteristics of the instrumentation and the

experimental device led to apply some additional filtering. On the one hand, the time-of-flight camera collected part of the free surface profile in the spillway, which can be observed for the lowest x values. This part of the free surface was thus discarded. On the other hand, for $x \sim 0.7$ m and for $x > 2$ m, the structure of the channel interfered with the instrumentation, affecting the collected data. These parts of the profile were substituted with the help of measures using limnimeters.

Once these issues were adequately treated, the analysis of the profiles was undertaken from a dimensionless perspective. To do so, the procedure presented by Hager [2] through Eqs. 25 and 26 was followed [5]. The resulting dimensionless free surface profiles were compared between them, as well as with the results presented in section 4.1.2 and with bibliographic profiles for CHJ (Figure 33). It is also important to highlight that the roller length (L_r) employed to obtain dimensionless values was estimated with the stagnation point criterion for the numerical and the physical (UPV) models. Nevertheless, the available instrumentation did not allow the application of this criterion in the physical model at TUWien. In this particular case, the expression for the determination of the hydraulic jump roller length by Wang and Chanson [8] was employed (Eq. 28).

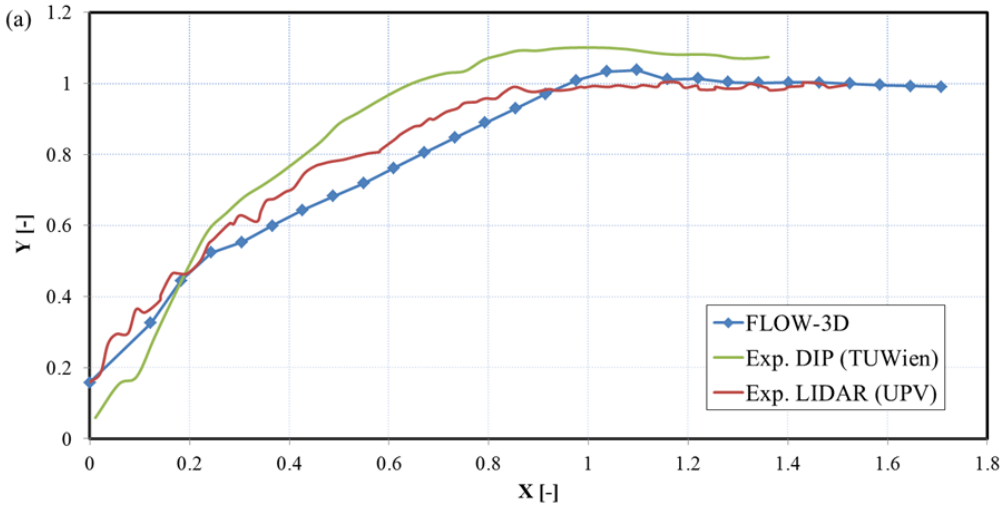

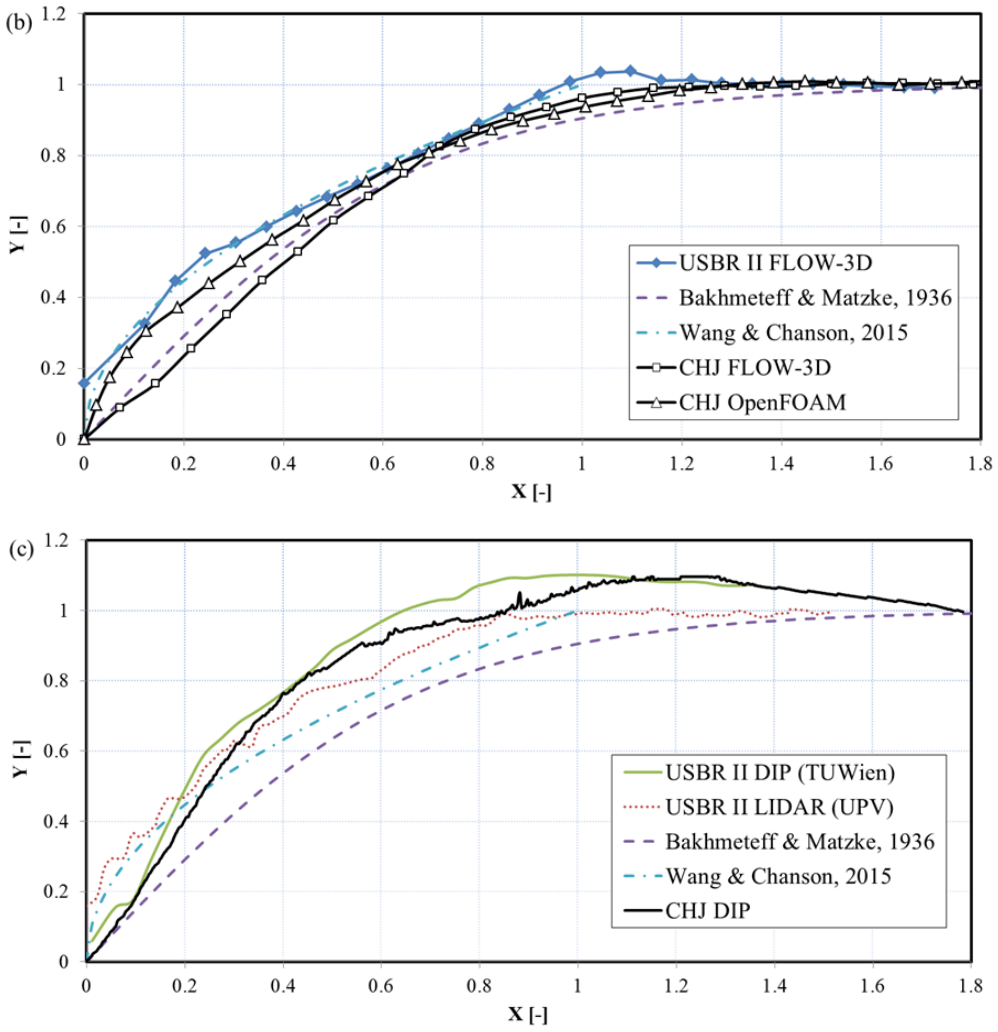

Figure 33. Comparison of the dimensionless free surface profile of the hydraulic jump in a typified USBR II stilling basin: (a) Profiles for the numerical and physical models (TUWien and UPV), (b) Comparison of the numerical model with those developed for the CHJ and bibliographic data [8], [39], (c) Comparison of the experimental results with those obtained for the CHJ and bibliographic data [8], [39].

Figure 33 (a) shows that there was a general good agreement in the trend followed by the free surface profiles obtained with all of the developed models. Hence, the coefficient of determination R^2 of the numerical model in comparison with the physical models was 0.931 (TUWien) and 0.968 (UPV), whereas between the two

physical models the value of this coefficient was 0.983. However, a slight overestimation of the profile was observed in the physical model at TUWien for $X > 0.2$. This can be explained through two factors. On the one hand, DIP techniques were employed to determine the free surface profile in this model. As observed for the CHJ, this method tended to overestimate the flow depths not only as a result of the presence of bubbles and droplets, but also because images had to be taken from the side of the experimental channel. On the other hand, the fact of not using a measured value of L_r to obtain the dimensionless profile could have affected the results. The use of a theoretical L_r value, thought for CHJ, could have particularly influenced the profile derived from this physical model. This was in good agreement with the model showing a higher sensitivity to the energy dissipation devices than the CFD model, reflected in the obtained lower sequent depths ratio and higher dissipation efficiency (Table 14 and Table 16) [5].

A specific comparison of the typified USBR II stilling basin numerical model with the CFD models presented for the CHJ (i.e. FLOW-3D® and OpenFOAM) and bibliographic CHJ results [8], [39] was also conducted (Figure 33 (b)). In spite of the general good agreement, an overestimation of the profile was observed near the origin ($X = 0$), in the proximity of the hydraulic jump toe. The main reason behind these differences was the affection of the energy dissipation devices, leading to higher flow depth values immediately downstream the chute blocks.

In terms of the comparison between physical models (Figure 33 (c)) this overestimation due to the chute blocks existing at the beginning of the stilling basin was observed too. In this particular case, the overestimation was even more significant for the central part of the roller, up to $X = 1$, regardless of the experimental technique employed (DIP or LIDAR) [5]. Furthermore, in this figure, the overestimation of the free surface profile derived from the application of DIP techniques was noted again.

In regards with the subcritical flow regime, the results from the presented models tended to stabilise and approach the subcritical flow depth, in accordance with the CHJ models and the bibliographic data reviewed [8], [39]. To sum up, the developed typified USBR II stilling basin models showed their ability to provide an accurate free surface profile for the hydraulic jump, close to those observed for a CHJ, but reflecting the influence of the energy dissipation devices on the flow.

5.2. Hydraulic Jump Efficiency

The hydraulic jump efficiency (η) for the presented models was also analysed, as a crucial feature to fulfil the energy dissipation purposes in stilling basins. This efficiency was calculated for each model on the basis of their results, using Eq. 23. The efficiency values for each model were also calculated by solving Eq. 23 with the sequent depths ratio previously obtained with the expressions for CHJ by Bélanger [33] and Hager and Bremen [23]. This was done in order to assess the influence of the energy dissipation devices on the resulting hydraulic jump efficiency (Table 16).

Table 16. Hydraulic jump efficiency obtained from the numerical and physical models and from the theoretical expressions by Bélanger [33] and Hager and Bremen [23].

	η	η **(Bélanger** [33]**)**	η **(Hager & Bremen** [23]**)**
Numerical model	0.507	0.488 (96.1%)[1]	0.502 (99.0%)[1]
Physical model (TUWien)	0.515	0.485 (93.8%)[1]	0.510 (99.0%)[1]
Physical model (UPV)	0.705	0.696 (98.7%)[1]	0.701 (99.4%)[1]

[1] In parenthesis: accuracy of the modelled values obtained using Eq. 22.

The results displayed in Table 16 show that the hydraulic jump simulated with the presented models provided efficiencies not far from those expected for a CHJ. Despite the obtained high levels of accuracy, the influence of the energy dissipation devices was detected, since the modelled efficiency values were above those others calculated using theoretical expressions for CHJ [23], [33]. These results, reflecting the specific design characteristics of the stilling basin to improve energy dissipation in the hydraulic jump, were in good agreement with previous research [5], [83]. The increase in the hydraulic jump efficiency found for the modelled results with lower Fr_1 value (namely FLOW-3D® and TUWien) was not as significant as the one reported by Padulano et al. [83]. These authors studied hydraulic jumps in a USBR II stilling basin with Fr_1 values ranging from 8.41 to 31.36. They found hydraulic jump efficiencies from 0.700 to 0.900 approximately, with decreasing efficiencies for lower Fr_1 values. In these terms, the trend established by Padulano et al. [83] from their experimental results showed that the efficiency value for a hydraulic jump with $Fr_1 \sim 4.95$ could be close to the values here reported for FLOW-3D® and the physical model at TUWien. Thus, the second physical model analysed (UPV), with $Fr_1 = 9.02$, provided an

efficiency in good agreement with the observations by Padulano et al [83]. These results showed that, although the effect of the energy dissipation devices increased the hydraulic jump efficiency, the affection caused by the inflow Froude number in this efficiency was larger.

To sum up, the observed accuracies were very similar to the ones discussed for the sequent depths ratio. This was expectable since the hydraulic jump efficiency is strongly correlated with the sequent depths ratio [5]. Consequently, the modelled sequent depths ratios were lower than the ones for a CHJ, while the efficiencies were higher. As previously mentioned these results were expected as a consequence of the energy dissipation devices existing in the USBR II stilling basin. The differences found with bibliographic research such as the one presented by Padulano et al. [83], were probably due to the higher Fr_1 values investigated by these authors in comparison with the ones used in the research here presented.

5.3. Roller Length

The hydraulic jump roller length was obtained using the stagnation point criterion for the typified USBR II stilling basin numerical model and for the physical model in the Hydraulics Laboratory of the Department of Hydraulic Engineering and Environment at the Universitat Politècnica de València (UPV, Spain). As already explained, this criterion implies measuring streamwise velocity vertical profiles along the hydraulic jump roller region [48]. For the physical model in the Hydraulics Laboratory of the Institute of Hydraulic Engineering and Water Resources Management, at the Technische Universität Wien (TUWien, Austria), the available instrumentation was not capable of taking reliable velocity measures within the roller. Therefore, as previously mentioned, the hydraulic jump roller length was not obtained for this model.

The roller length values resulting from the application of the stagnation point criterion to the developed models were compared to those calculated using bibliographic expressions for CHJ (Table 17). These theoretical expressions were the one proposed by Hager et al. [48] (Eq. 27) and the one by Wang and Chanson [8] (Eq. 28) for Fr_1 values between 1.5 and 8.5.

Table 17. Hydraulic jump roller length obtained from the numerical and physical models and from the theoretical expressions by Hager et al. [48] and Wang and Chanson [8].

	L_r	L_r **(Hager et al.** [48]**)**	L_r **(Wang & Chason** [8]**)**
Numerical model	41.00 m	39.20 m (95.4%)[1]	36.20 (86.7%)[1]
Physical model (UPV)	1.25 m	1.67 m (74.9%)[1]	--

[1] In parenthesis: accuracy of the modelled values obtained using Eq. 22.

The expression by Wang and Chanson [8] was not used for the typified USBR II stilling basin physical model because the inflow Froude number (Fr_1 =9.02) was out of the range considered by these authors. Although the obtained results were not far from those estimated with the expressions thought for a CHJ, significant differences were found. It must be considered that the stagnation point criterion employed for the estimation of the roller length depends not only on the modelled free surface profile, but also on the streamwise velocity vertical profiles along the roller region. The determination of such profiles is complex to a high degree both, for the numerical and the physical model. On the one hand, as it was noted in the CHJ simulations, the CFD codes still present some limitations to reproduce with total accuracy some internal flow features, especially in the roller region where the turbulence is particularly intense. On the other hand, the already mentioned uncertainty associated to the information collected by the Pitot tube within the roller region has to be taken into account. Hence, it was not possible to identify a clear trend on how the hydraulic jump roller length changes in a typified USBR II stilling basin in comparison with a CHJ with the same conditions. Nevertheless, the developed models and applied techniques showed their ability to provide reasonable values of this length.

5.4. Velocity Profiles

5.4.1. Velocity Distribution in the Roller Region

As explained for the determination of the hydraulic jump roller length, velocity measures within the roller were collected both for the numerical model and for the physical model in the Hydraulics Laboratory of the Department of Hydraulic Engineering and Environment at the Universitat Politècnica de València (UPV, Spain).

Consequently, the analysis of the velocity distribution within the roller region of the hydraulic jump in a typified USBR II stilling basin was focused on these two models.

The analysis was conducted through the study of a series of streamwise velocity vertical profiles collected along the hydraulic jump longitudinal axis, throughout the roller region. For the classical hydraulic jump the procedure followed consisted in adjusting the theoretical expression by McCorquodale and Khalifa [47] to the results, in order to obtain continuous velocity profiles. However, this expression was thought for CHJ and the agreement with the profiles obtained in a typified USBR II stilling basin was not satisfactory. The results from the numerical model and the qualitative observations and data collected with the Pitot tube in the physical model (UPV) showed that there was a clear affection of the chute blocks in the studied velocity profiles (Figure 34). Hence, the flow deflection caused by these energy dissipation devices provided the highest velocities in the lowest part of the profile, in contrast with the profile shape observed for the CHJ and provided by the analytical expression (Eqs. 29 and 30) [47]. This affection was observed for a significant stretch of the hydraulic jump roller region, thus preventing from undertaking the aforementioned adjustment process.

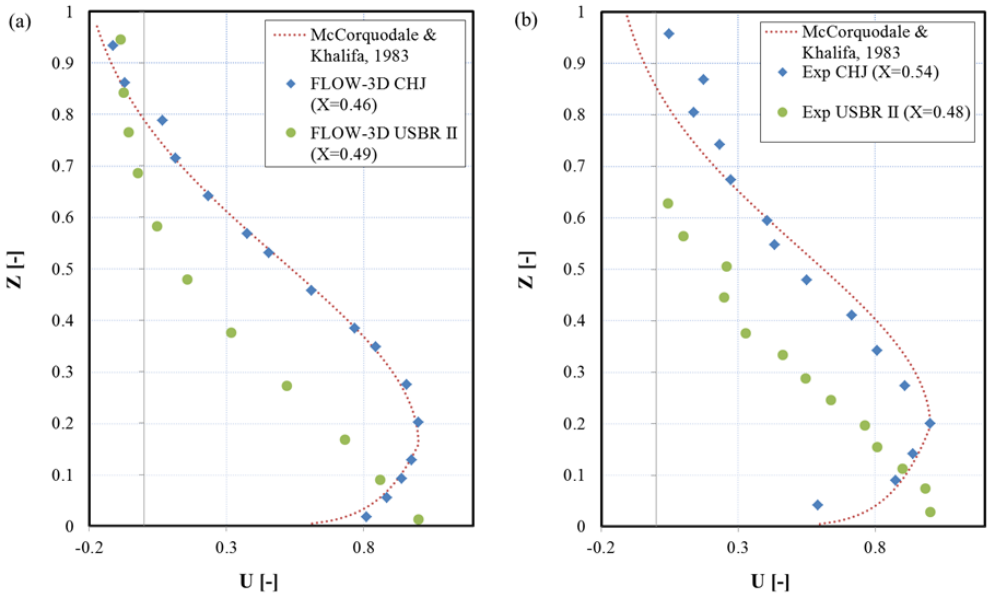

Figure 34. Vertical velocity profiles within the hydraulic jump roller region. Comparison between the CHJ and the hydraulic jump in a typified USBR II stilling basin for $\boldsymbol{X} \sim 0.5$: (a) Numerical model, (b) Physical model (UPV).

Figure 34 showed the affection of the chute blocks existing in the typified USBR II stilling basin. As a result of this influence, for a similar position within the hydraulic jump roller, there were significant differences in the streamwise velocity vertical profile for the CHJ and the hydraulic jump occurring in the basin. In order to represent together in Figure 34 data coming from different models, the following normalisation process was followed:

$$Z = \frac{z}{y} \tag{47}$$

$$U = \frac{u}{u_{max}} \tag{48}$$

where y is the flow depth and u_{max} the maximum velocity, both in the corresponding vertical profile under study. Hence, for the analysis developed in this section the adjustment using the expression by McCorquodale and Khalifa [47] was discarded and the presented results were obtained directly from the models' data. In these terms, the obtained maximum forward velocity decay from the hydraulic jump toe (Figure 35 (a)),

together with the maximum backwards velocities (Figure 35 (b)), were compared with those expected for a CHJ. The dimensionless values employed for this figure were calculated following the procedure previously described (Eqs. 31 and 32).

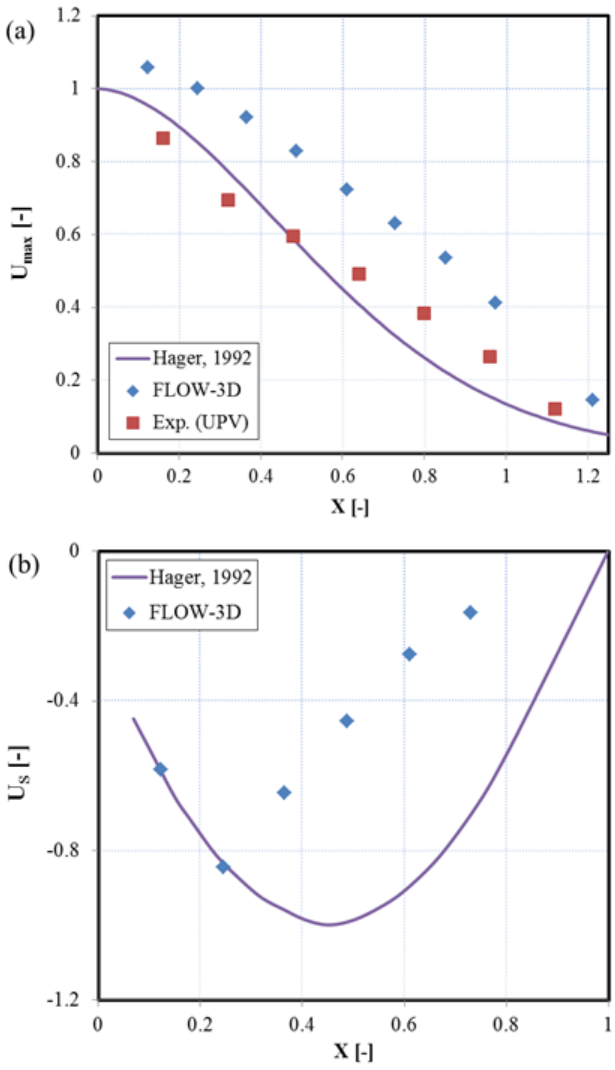

Figure 35. Velocity analysis in the hydraulic jump roller region comparing results from the numerical and physical typified USBR II stilling basin models and Hager [2]: (a) Maximum forward velocity decay, (b) Maximum backwards velocities.

Significant differences were observed in the results presented in Figure 35. This was expected since the hydraulic jump occurring in a typified USBR II stilling basin was compared with a CHJ. In these terms, the observed differences can be associated to the stilling basin design. For the maximum velocity decay (Figure 35 (a)), the values obtained for the stilling basin in the numerical model were systematically above those indicated for a CHJ. The observation of each profile separately showed that this had to do with the effect of the chute blocks. The deflection caused by these energy dissipation devices in the flow provided the highest velocities in the lowest part of the flow, for all of the profiles with $X < 1$. This alteration of the velocity profile shapes increased the difference between the maximum velocities within the hydraulic jump roller and the subcritical mean velocity. Hence, the overestimation observed in Figure 35 (a) was probably due to these differences, considering that the dimensionless values were obtained employing Eq. 31.

Two more particularities of how the stilling basin design influenced the maximum forward velocity decay can be highlighted. On the one hand, FLOW-3D® provided a value of U_{max} larger than 1 for the closest profile to the chute blocks. This indicated that the deflection caused by the energy dissipation devices was relevant enough to trigger a maximum velocity in the closest profile above the mean supercritical velocity. On the other hand, a constant decay in the maximum velocity can be observed for the profiles with $X < 1$, until the location of the end sill ($X \sim 1.1$). Then one more profile downstream the end sill was measured, whose maximum velocity was not obtained in the lowest part. This profile, although was still affected by the energy dissipation devices, was closer to the ones observed in CHJ for similar locations and hence, its maximum velocity approached the expression by Hager [2].

The results obtained in the physical model were closer to those of the CHJ. However, the slower maximum forward velocity decay already observed in the numerical model was found for these results too. Actually the trend followed by the data collected in the physical model seemed to be between the results from the USBR II stilling basin FLOW-3D® simulations and the bibliographic expression for a CHJ [2]. This was in good agreement with the subcritical flow depth and hydraulic jump efficiency values obtained for this physical model (Table 15 and Table 16). Consequently, although the affection of the energy dissipation devices in this physical model (UPV) was clearly noted, it was not as significant as for the numerical model.

Regarding the maximum backwards velocities, data from the physical model was not included in the comparison since it was neither possible to obtain backwards velocities with the Pitot tube nor to adjust the analytical profile by McCorquodale and Khalifa [47]. For the results obtained with the numerical model, a good agreement with the bibliographic results was observed for the profiles closer to the hydraulic jump toe. In profiles placed downstream $X \sim 0.3$, the differences with the expression proposed by Hager [2] increased, meaning that the backwards velocities were not as intense as those displayed for a CHJ. However, FLOW-3D® already showed some limitations to reproduce the backwards velocities in the section devoted to the CHJ analysis (section 4.4.1) and thus, these results must be carefully considered.

Apart from these maximum values, the complete vertical velocity profiles obtained with the numerical and physical models were individually analysed too. These profiles were represented in Figure 36, together with the expression by Hager [2] for the diffusion portion of velocity profiles in the CHJ roller region (Eq. 33), for comparison purposes. The dimensionless values displayed in this figure were obtained through Eqs. 34 and 35, following the process previously explained.

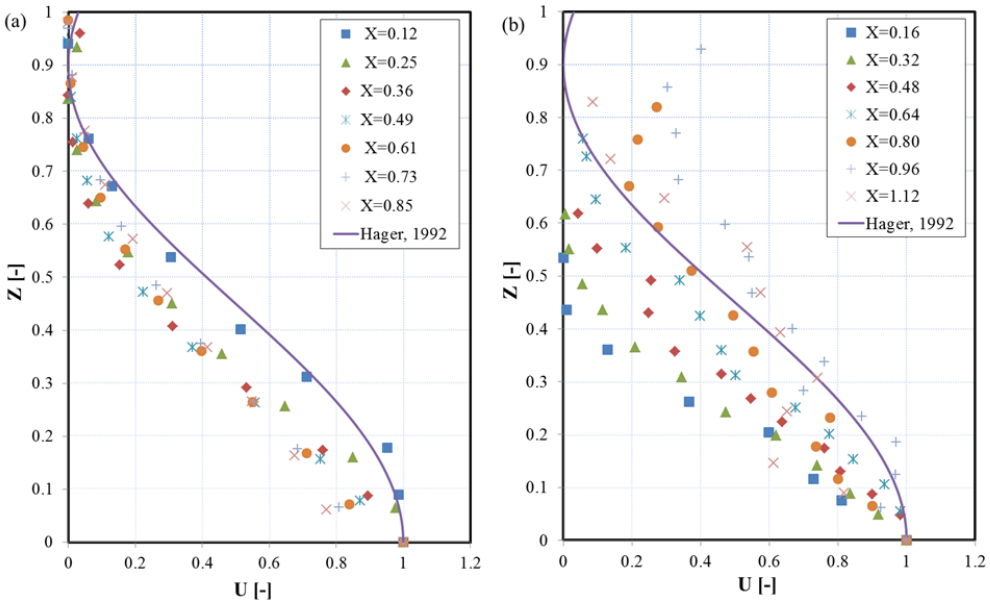

Figure 36. Vertical velocity profiles obtained along the hydraulic jump roller region in the longitudinal axis of the typified USBR II stilling basin models and comparison with the expression proposed by Hager [2] for CHJ: (a) FLOW-3D® model, (b) Physical model (UPV).

The observation of the results showed a general good agreement for all of the profiles obtained in the numerical model, regardless of their position along the roller region (Figure 36 (a)). Furthermore, despite the modelled profiles were not far from the trend proposed by Hager [2], some differences due to the design of the stilling basin were found. Hence, the profiles obtained with FLOW-3D® showed faster velocity decay from the channel streambed than the profile proposed for a CHJ. This observation is in the line of the aforementioned alterations in the profile as a result of the flow deflection in the chute blocks. This effect was not as relevant for the region closer to the free surface and hence, for Z values larger than 0.5, the modelled profiles tended to approach the analytical expression by Hager [2]. It was also detected that the profile for the lowest X value slightly differed from the general trend shared by the rest of the profiles. This profile was very close to the beginning of the stilling basin, presenting a relatively small flow depth. These conditions could have maximised the influence of the energy dissipation devices in the profile, leading to the observed differences.

Regarding the physical model (UPV) larger differences both, among the profiles and in comparison with the expression by Hager [2] were found (Figure 36 (b)). It is

important to remark that the performance of the Pitot tube can be severely affected by intense velocity turbulences and the presence of bubbles [9]. These issues already observed in the CHJ study gained relevance in the USBR II stilling basin physical model, since it was not possible to adjust the analytical expression by McCorquodale & Khalifa [47] (Figure 34). Therefore, the backwards velocities could not be estimated which particularly affected the representation of dimensionless results for high Z values (Eqs. 34 and 35). Nevertheless, some interesting results were found. As previously observed for the numerical model, there was a faster decay of U from the channel streambed in comparison with the bibliographic expression for a CHJ [2]. This faster decrease was especially relevant in sections close to the hydraulic jump toe, but as the X increased, the profiles tended to approach the CHJ velocity profile, in contrast with the observations for the numerical model. This was in good agreement with the previously developed results showing a lower influence of the energy dissipation devices in this physical model (UPV). Finally, the behaviour of the profiles with the highest X values had discrepancies with other displayed results. This is explained because the roller end section is placed at $X = 1$. Consequently, these profiles were likely to follow velocity distributions typical for the roller region, but already influenced by the subcritical flow downstream this region.

5.4.2. Velocity Profiles in the Supercritical and Subcritical Flow Regimes

A series of velocity profiles were analysed outside the roller region for the numerical model and for the physical model in the Hydraulics Laboratory of the Institute of Hydraulic Engineering and Water Resources Management, at the Technische Universität Wien (TUWien, Austria). In particular, velocity in the streamwise direction was measured in three different sections [5]. Firstly, a section in the spillway was considered, where supercritical flow with an almost uniform velocity distribution was obtained for both models. The following two locations were chosen right upstream and downstream of the end sill (Figure 19).

Regarding the profiles upstream and downstream the end sill, two profiles were measured per cross-sectional position. Consequently, the influence of the energy dissipation devices of the model in the three-dimensional structure of the flow was analysed. Figure 37 shows the cross-sectional positions considered.

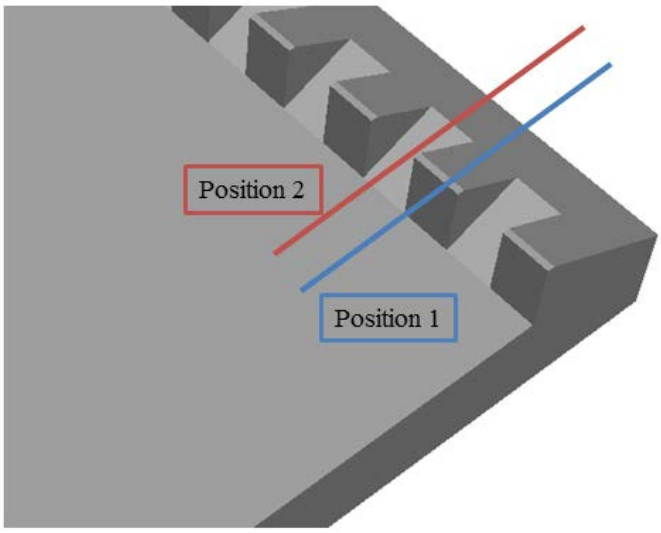

Figure 37. Cross-sectional positions considered to obtain streamwise velocity vertical profiles upstream and downstream the end sill of the typified USBR II stilling basin numerical and physical model (TUWien).

In these terms, Figure 38 compares such profiles upstream and downstream the end sill, resulting from both models [5]. The presented normalised values were obtained with the procedure described in Eqs. 40 and 41.

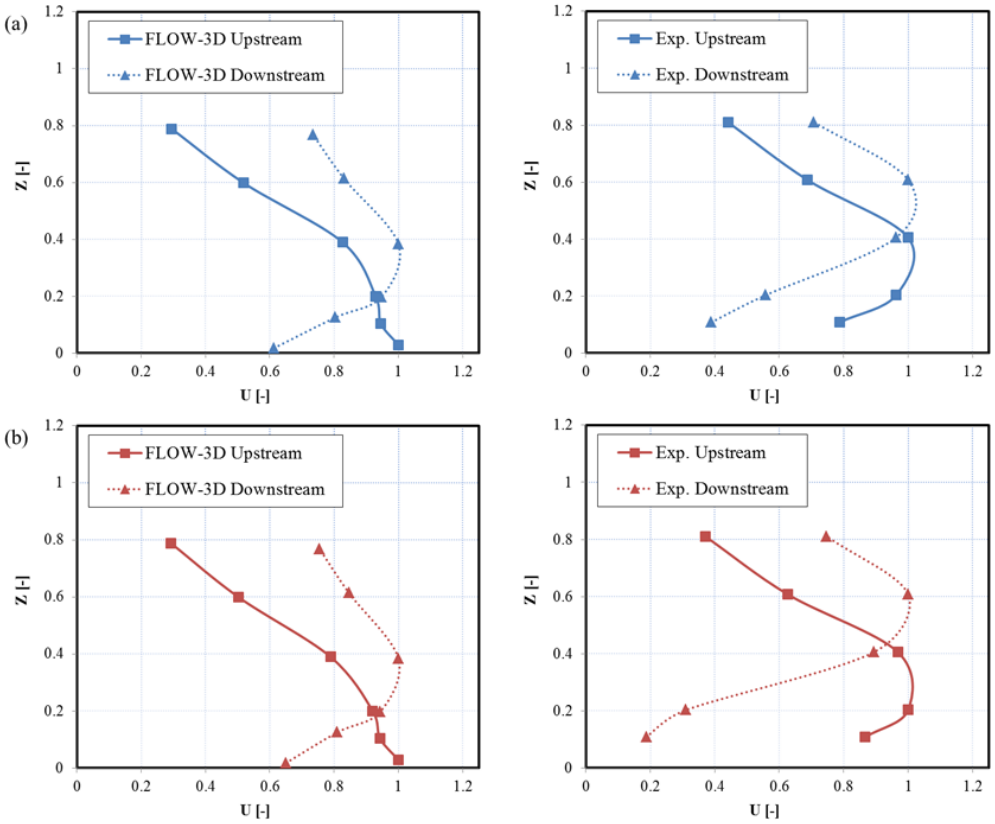

Figure 38. Streamwise velocity vertical profiles upstream and downstream the end sill of the typified USBR II stilling basin, obtained with the numerical (FLOW-3D®) and the physical model (TUWien): (a) Position 1, (b) Position 2.

Regardless of the cross-sectional position under analysis, the effect of the energy dissipation device was clearly observed in the velocity profiles. In particular, and as a result of the sill interference with the flow, the velocity magnitude decreased in the lower part of the profile for the downstream profiles. As there was not a significant variation in the flow depth for these two relatively close profiles, such velocity decrease in the lower part was necessarily linked to a velocity increase in the upper part of the profile, as showed in Figure 38. This affection of the end sill was observed both for the physical and the numerical model. Furthermore, there was a good agreement between the profiles obtained in the experimental campaign and with FLOW-3D®, especially for the upper part of the profile. However, some differences between models

were found for the lowest Z values, related with the position for the maximum velocity in the profile. For profiles in the same position, both upstream and downstream the end sill, the experimental results provided the maximum velocity magnitude for higher Z values than FLOW-3D®. It is important to highlight that, although the general shape of the profiles and the affection of the end sill is clearly reflected by both models, measures in these positions were specially challenging. Hence, the proximity of the energy dissipation device and the associated turbulent fluctuations may have contributed to the instrumentation uncertainty and affected the performance of the models.

In terms of the cross-sectional position analysed, Figure 38 shows that there were no significant differences for the numerical model. In contrast, for the physical model, the differences between the upstream and the downstream profile changed depending on the analysed position. Despite the general trend and the previously mentioned affection of the end sill remained for both positions, this affection appeared to be more relevant for position 2, with higher velocity differences. A possible explanation for this is that, for position 2 the profiles were measured upstream and downstream one of the gaps forming the end sill. In these gaps there is an adverse slope which could have deflected the flow to higher Z positions, resulting in lower velocity magnitudes for the lowest part of the profile downstream the end sill. In addition, the upstream profile in position 1 was measured close to the front side of one of the blocks forming the sill. This could have partially stopped the flow, providing the slightly lower velocity values observed for the lowest part of the profile, in comparison with the upstream profile measured in position 2.

A deeper analysis of this profiles showed that there was not a good agreement with other velocity distributions obtained for the roller region in a CHJ, such as the analytical profile by McCorquodale and Khalifa [47] (Eqs. 29 and 30). This was expectable since the profiles, besides belonging to a stilling basin model with its own particularities, were collected downstream the roller region. Furthermore, important differences were also found in comparison with other velocity profiles for free surface flow in open channels, like the one by Kirkgoz and Ardiclioglu [130] (Eq. 36). These differences were mainly due to the proximity of the profiles and the end sill, leading to an important affection of the energy dissipation device on the velocity distributions under study [5].

5.5. Pressures Analysis

Pressure values were obtained in two different positions on the front side of two of the blocks forming the end sill of the USBR II stilling basin in the numerical model and the physical model in the Hydraulics Laboratory of the Institute of Hydraulic Engineering and Water Resources Management, at the Technische Universität Wien (TUWien, Austria) [5]. First of all, it is important to highlight that the measures taken in both blocks provided similar pressure values. The pressure transmitters used and the characteristics of the physical model (Figure 20 (b)) allowed measuring in these particular positions, looking for cross-sectional differences. However, the similarity obtained in the results both for the physical and the numerical model led to the analysis presented in this section, without distinguishing the position in the cross-section.

Averaged relative pressure in the end sill was obtained as $p/(\rho g y_1)$ [5].The resulting values for both, the numerical and physical model, ranged between 5 and 6, whereas, for that same relative position in a CHJ, Toso and Bowers [49] reported values around 6.5. These lower relative pressure values can be explained through the specific properties of the hydraulic jump in a typified USBR II stilling basin. As it was observed in terms of efficiency, the hydraulic jump associated to this basin dissipated more energy than the CHJ (Table 16). Furthermore, the hydraulic jump in the stilling basin provided lower subcritical flow depths (Table 15). Considering the position of the end sill, downstream the hydraulic jump roller, these two factors are in good agreement with the lower average relative pressure values registered in the presented models.

In regards with the drag force acting on the sill, it can be expressed by means of the drag coefficient (C_d). The assessment of the force acting in the sill is crucial for its correct design. Padulano et al. [83] proposed the following expression to obtain the drag coefficient in the end sill of a typified USBR II stilling basin:

$$C_d = \frac{1-(1+S)^2\left(\frac{y_2^*}{y_1}\right)^2 - 2Fr_1^2\left\{\left[(1+S)\left(\frac{y_2^*}{y_1}\right)\right]^{-1} - 1\right\}}{\lambda\frac{d_2}{y_1}Fr_1^2} \tag{49}$$

where $S = (y_2 - y_2^*)/y_2^*$ is the submergence factor, being y_2^* the subcritical flow depth calculated using Bélanger's expression [33] (Eq. 46), λ is the ratio of blocked

width to total basin width, and d_2 is the height of the end sill (Figure 11). The drag coefficients resulting from the numerical and the physical models using this expression were 0.17 and 0.25, respectively. These values were lower than those observed by Padulano et al. [83], likely due to the higher inflow Froude numbers tested by these authors, which also led to the aforementioned differences in terms of sequent depths ratio and hydraulic jump efficiency . Hager [2] presented an alternative expression for the drag coefficient:

$$C_d = \frac{F_d}{\frac{1}{2}\rho d_2 b u_1^2} \tag{50}$$

where b is the stilling basin width and F_d the drag force. Eq. 50 can be used instead of Eq. 49 to estimate C_d coefficient, as long as the drag force value is available. Estimating F_d as the product of the measured pressure and the vertical projection of the sill area, the resulting C_d values are 0.35 for the FLOW-3D® model and 0.71 for the experimental model [5]. These values were closer but still below the ones reported by Padulano et al. [83].

Nevertheless, Ohtsu et al. [76] conducted an experimental research on the drag on vertical sills of stilling basins. On the basis of their experimental observations they proposed the following expression:

$$C_d = 0.71 - 0.85\left(\frac{x_s}{L_j}\right) \tag{51}$$

where x_s is the distance between the hydraulic jump toe and the upstream face of the sill and the hydraulic jump length is obtained as $L_j = 5.5y_2^*$. The drag coefficient obtained for the presented models using the definition by Ohtsu et al. [76] was in the line of their experimental results.

Finally, despite the physical model characteristics and the available instrumentation prevented from taking streambed pressure measures in both physical models (TUWien and UPV), some information was extracted from the FLOW-3D® numerical model. Pressure fluctuations can give information about the efficiency of a typified USBR II stilling basin, as they are related with the remaining turbulence downstream the end sill [83]. The streambed pressure was obtained in two positions in the proximity of the end sill for the numerical mode longitudinal axis, one upstream and another one downstream the energy dissipation device. In accordance with the results presented by

Fecarotta et al. [84], also for a typified USBR II stilling basin, a significant decrease of the standard deviation for the pressure fluctuations downstream the end sill was found. Hence, the largest part of the turbulence was enclosed within the basin [83]. Furthermore, the absolute value of the extreme negative fluctuations was higher than the one for the positive fluctuations, in good agreement with other bibliographic results [49], [83].

5.6. Void Fraction Distribution

The present section deals with the analysis of the void fraction distribution throughout the longitudinal axis of the hydraulic jump in a typified USBR II stilling basin. To this end, data was collected from the numerical FLOW-3D® model and from the physical model in the Hydraulics Laboratory of the Institute of Hydraulic Engineering and Water Resources Management, at the Technische Universität Wien (TUWien, Austria). The analysis was conducted through a comparison with bibliographic results regarding the void fraction distribution in a CHJ [5], [85]. To undertake this comparison it was crucial to unify criteria and work with normalised values and expressions. Therefore, the void fraction analysis was carried out on the basis of the expressions presented by Murzyn et al. [52]. The formulation proposed by these authors differentiates two flow regions in the modelling process of the void fraction vertical profiles throughout the hydraulic jump, namely, the lower and the upper region. These two regions are separated by the turbulent shear layer, with a different analytical expression for the void fraction distribution followed in each region. On the one hand, for the lower region of the flow, the void fraction (C) distribution follows a diffusion equation [134], represented by the expression:

$$C = C_{max} exp\left[-\frac{1}{4}\frac{u_1}{D}\frac{(\xi-\xi_{Cmax})^2}{x}\right] \quad (52)$$

where D is a diffusion coefficient, ξ is the normalised flow depth obtained as y/y_1 and ξ_{Cmax} is the normalised depth at which the void fraction reaches its maximum (C_{max}). On the other hand, similar conditions similar to the edge of water jets freely discharging into the air can be assumed for the upper region and, consequently, the expression by Brattberg et al. [135] is followed in this region:

$$C = \frac{1}{2}\left[1 + erf\left(\frac{\xi - \xi_{C50}}{2\sqrt{Dx/u_1}}\right)\right] \quad (53)$$

where a void fraction value of 0.5 is reached at ξ_{C50}. It should be noticed that the supercritical mean flow velocity (u_1) value is the same both for Eq. 52 and Eq. 53. In contrast, the diffusion coefficient value varies between these two equations. This is due to the different air entrainment mechanisms associated with the two defined regions.

The void fraction vertical profile proposed by Murzyn et al. [52], developed through Eqs. 52 and 53, was adjusted to laboratory data collected in a series of profiles throughout the stilling basin physical model. The same procedure was carried out on the basis of void fraction information, obtained from the numerical model [85]. In particular, 6 different profiles were employed to characterise the void fraction distribution along the hydraulic jump longitudinal axis. Table 18 shows the normalised position of these profiles for the presented models [5].

Table 18. Normalised position of the vertical profiles considered for the void fraction distribution analysis [5].

Model	x/y_1					
Numerical model	1.32	5.84	11.18	20.64	26.56	33.96
Physical model (TUWien)	1.31	5.82	11.14	20.57	26.47	33.85

The preliminary observation of the adjustment process results showed a high level of coincidence between ξ_{Cmax} and the normalised depth of the boundary between regions (ξ_*). Setting ξ_{Cmax} equal to ξ_* allowed linking the two distributions by this boundary common value, so that the approach became coherent. In practice, this implied a more parsimonious model representing the whole void fraction profile [5]. Consequently, the analysis was developed considering $\xi_{Cmax} = \xi_*$. Figure 39 exemplifies the adjustment by showing the void fraction values obtained for a particular profile (Table 18), extracted from the physical (Figure 39 (a)), and the numerical models (Figure 39 (b)). The analytical distributions fitted according to Eqs. 52 and 53 were also displayed in this figure.

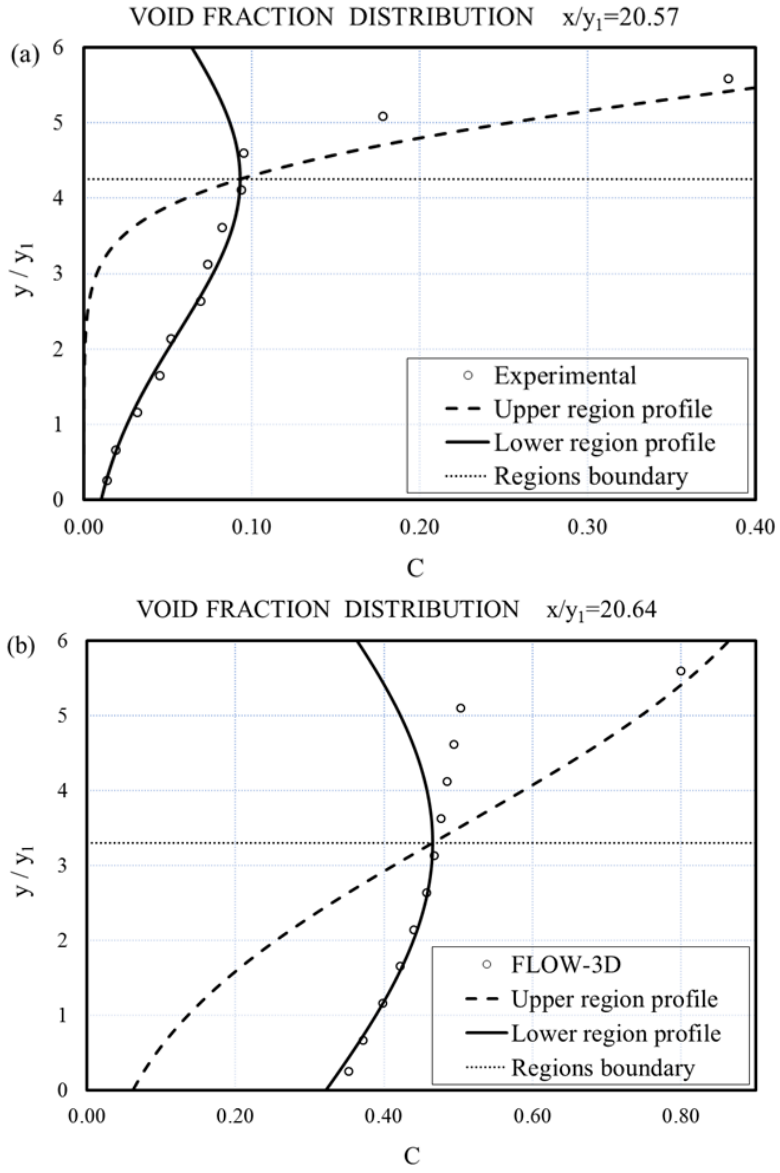

Figure 39. Void fraction profile results with the adjusted analytical expressions for the lower (Eq. 52) and the upper (Eq. 53) regions [5]: (a) Physical model ($\boldsymbol{x/y_1} = 20.57$), (b) Numerical model ($\boldsymbol{x/y_1} = 20.64$).

A first approach to the results obtained from the models and the adjustment process of the analytical profiles previously presented, led to the exclusion of part of the data from the analysis [5]. Firstly, for the numerical model, values corresponding to the upper region of the flow did not follow the distribution presented in Eq. 53. Therefore, the aeration mechanism occurring in this region was not adequately reproduced by the model (Figure 39 (b)). Actually, flow aeration in CFD modelling remains as one of its main challenges [30], [52], [85]. Highly aerated flows, such as the one here studied, remark the limitations of the VOF approach [5], [110]. Ma et al. [65] already found that a RANS approach was able to provide the void fraction profiles in the lower shear layer region, which contains the air bubbles entrained at the jump toe of the hydraulic jump. In contrast, these authors found that in the upper roller region behind the toe, the averaged results of the RANS model were not able to provide accurate predictions. Moreover, in this particular numerical set up, modelling aeration involved the estimation of several parameters by means of a thorough calibration process that needs to be extended. Hence, the numerical model was not considered for the upper region analysis in the present research.

In regards with the experimental measures, the data obtained with the optical fibre probe in the first profile ($x/y_1 = 1.31$) showed an anomalous behaviour, which was not observed in subsequent sections. This can be explained by the proximity to the hydraulic jump toe. The relatively low flow depth for this profile, together with the presence of intense turbulent fluctuations, may have affected the performance of the probe. Consequently, this first profile was excluded from the analysis concerning the physical model data [5].

Once the information coming from both models was filtered, the analysis was undertaken. Hence, the refined data sample was used to estimate the parameters from Eqs. 52 and 53. These parameters were analysed for both, the upper and the lower region. In this process, the results were compared with data from Murzyn et al. [52] and Chanson and Brattberg [51], obtained for a CHJ with a Fr_1 value of 3.7 and 6.3, respectively (Figure 40 and Figure 41) [5].

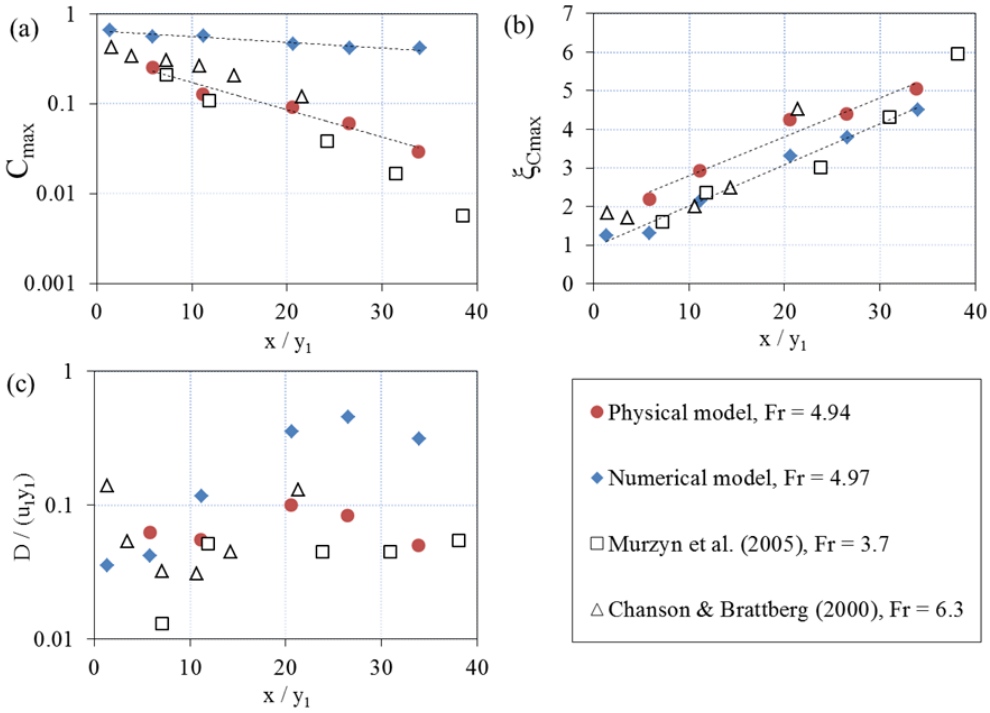

Figure 40. Parameters of the void fraction distribution in the hydraulic jump lower region for the typified USBR II stilling basin numerical and physical models [5]: (a) Maximum void fraction ($\boldsymbol{C_{max}}$), (b) Normalised height for the maximum void fraction ($\boldsymbol{\xi_{Cmax}}$), (c) Diffusion coefficient for the lower region ($\boldsymbol{D}$).

The results displayed in Figure 40 allowed discussing a series of interesting observations about the void fraction distribution parameters for a hydraulic jump in a USBR II stilling basin, in comparison with a CHJ [5]. Regarding the parameter C_{max} (Figure 40 (a)), that is, the maximum void fraction in the lower region, Murzyn et al. [52] suggested that its evolution throughout the hydraulic jump followed an expression of the form:

$$C_{max} = \alpha \times exp(-Ax/y_1) \tag{54}$$

where α and A are constant values that define the trend. For the physical model, the estimated values were α = 0.35 and A = 0.07, whereas for the numerical model values of α = 0.65 and A = 0.02 were obtained. With these values, Eq. 54 provided an

accurate representation of C_{max}variation along the hydraulic jump, in comparison with bibliographic results [51], [52]. The coefficient of determination (R^2) values were 0.966 and 0.928 for the physical and numerical model, respectively. Furthermore, in the physical model, the rate of decrease for $C_{max}$was very close to that one reported by Murzyn et al. [52] and Chanson and Brattberg [51]. In contrast, for the numerical model, such decrease was slightly slower, as it can be observed in Figure 40 (a) [5].

Results concerning the normalised height at which this maximum void fraction is reached (ξ_{Cmax}) were represented in Figure 40 (b). This figure shows larger ξ_{Cmax} values with increasing distances to the hydraulic jump toe. The estimated gradient was 0.101 for the physical model and 0.107 for the numerical model. These results showed a high level of agreement with those obtained by Murzyn et al. [52] and Chanson and Brattberg [51], who reported gradients of 0.102 and 0.108, respectively.

In regards with the estimated values of the diffusion coefficient (D) for the lower region (Figure 40 (c)), results from the present research led to generally higher D values, in comparison with previous research by Murzyn et al. [52] and Chanson and Brattberg [51]. In terms of the trend followed by this coefficient along the hydraulic jump, a significant dispersion of D values was observed, in good agreement with previous observations by Murzyn et al. [52].

To conclude with the discussion of Figure 40, it is important to remark that the estimated parameters for the lower region generally showed a satisfactory agreement with previous values reported in the literature both, for the numerical and for the physical model. Nevertheless, it was noticed that there was a slightly slower decrease in C_{max}, when compared to bibliographic data. This decrease was particularly slower for void fraction distributions extracted from the numerical model. Besides, relatively higher ξ_{Cmax} values were also found for the presented models, in comparison with other sources. Both differences could be explained by the energy dissipation devices of the typified USBR II stilling basin, causing affection to the aeration structure when compared to the CHJ phenomenon [5]. Hence, the energy dissipation devices affected the flow, increasing the air entrainment throughout the hydraulic jump, in good agreement with previous observations [17], [85]. Furthermore, the aforementioned normalisation of height for the presented void fraction profiles was carried out considering the supercritical flow depth (y_1). Thus, the higher values of ξ_{Cmax} obtained for the hydraulic jump in the USBR II basin were in accordance with

previously discussed results, which pointed out an increase in flow depths for the hydraulic jump roller, in comparison with CHJ.

Regarding the upper region of the flow, Figure 41 shows the results obtained for the estimated parameters used in the characterisation of void fraction distributions in this region [5]. Apart from the diffusion coefficient (D) and the normalised height where the boundary between regions (ξ_*) was placed, the normalised heights at which C is 0.95 (ξ_{C95}) and 0.5 (ξ_{C50}) were represented. As previously explained, the only data analysed for the upper region was the one collected in the physical model. Results from the numerical simulations were discarded, as the flow aeration in this region was not appropriately represented.

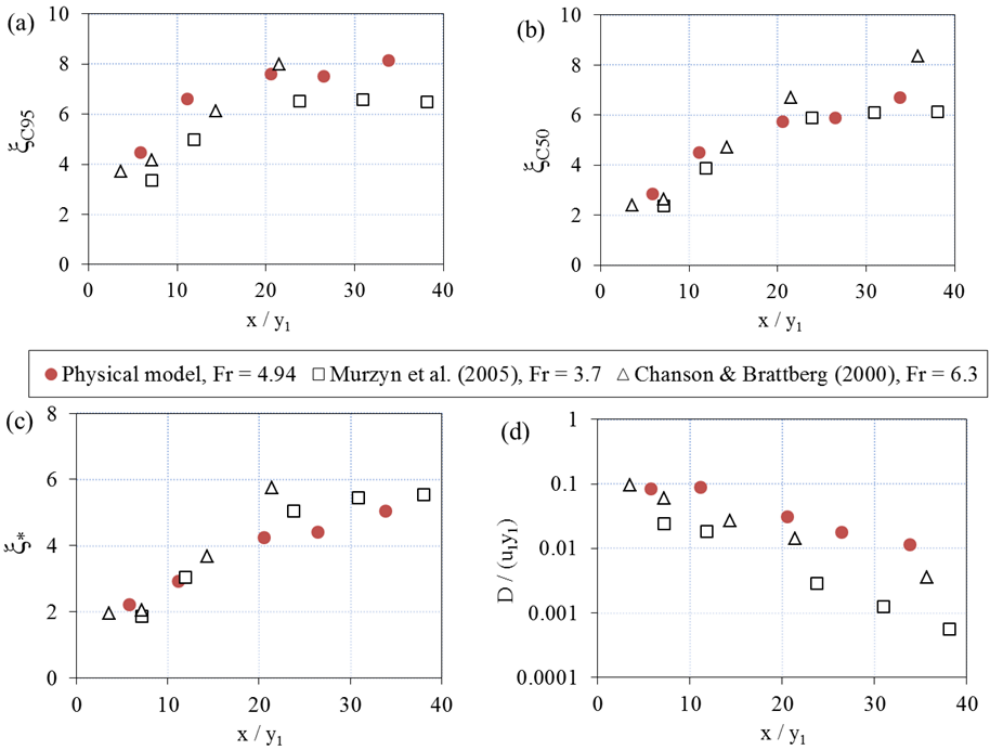

Figure 41. Parameters of the void fraction distribution in the hydraulic jump upper region for the typified USBR II stilling basin physical model [5]: (a) Normalised height at which the void fraction is 0.95 ($\boldsymbol{\xi_{C95}}$), (b) Normalised height at which the void fraction is 0.5 ($\boldsymbol{\xi_{C50}}$), (c) Normalised height of the boundary between regions ($\boldsymbol{\xi_*}$), (d) Diffusion coefficient for the upper region ($\boldsymbol{D}$).

Figure 41 shows a general good agreement between the trends followed by the results collected in the physical model and previous bibliographic results [51], [52]. The three height parameters analysed, namely ξ_*, ξ_{C95}, and ξ_{C50}, showed increasing values from the hydraulic jump toe position (Figure 41 (a)-(c)). However, this increasing trend was not constant. Hence, the rate of increase for ξ_*, ξ_{C95} and ξ_{C50} was higher in the sections closer to the hydraulic jump toe, and not so significant for further locations. These observations showed that the region where interfacial aeration is the predominant air entrainment mechanism increased its thickness with the distance to the hydraulic jump toe [5]. This behaviour was also noted by Murzyn et al. [52]. In these terms, the slowdown in the rate of increase for these normalised heights suggested a widening of the upper region along the hydraulic jump longitudinal axis. Some differences can also be remarked, due to the energy dissipation devices of the USBR II basin. An increase in the flow depth in the proximity of the hydraulic jump toe, in comparison with a CHJ, was observed in the free surface profile analysis. This increase was also noted through the higher values of ξ_{C95} and ξ_{C50} (Figure 41 (a) and (b)) obtained in the physical model when compared with bibliographic data [51], [52].

Finally, the results for the diffusion coefficient (D) (Figure 41 (d)), showed a decreasing trend with the distance from the hydraulic jump toe in the upper region, unlike previously estimated values for the lower region [5]. Although the magnitudes of the coefficient seemed higher for the presented model, the trend was in good agreement with the observations made by Murzyn et al. [52] and Chanson and Brattberg [51].

Chapter 6. Conclusions

The main conclusions derived from the research are presented in this section. In order to gain perspective on the achievements, it is important to remark the interest, but also the challenge posed by the study of the flows covered in this research. The hydraulic jump is known to be one of the most complex phenomena in fluid mechanics and, at the same time, it constitutes a tool of paramount importance for hydraulic engineering applications. It is this complexity, placing the current knowledge far from a full understanding of the phenomenon, bound to its undeniable interest for energy dissipation purposes that motivated the detailed study of the hydraulic jump.

The hydraulic jump is characterised by multiple features such as the intense air entrainment, the significant energy dissipation and large turbulence leading to velocity and pressure fluctuations, which contribute to build the complexity of the phenomenon. However, besides the influence of these physical processes separately, it is the interaction between them what makes extremely difficult to fully understand and model in detail the hydraulic jump phenomenon [8], [19].

The present research provides a solid and rigorous methodological framework for hydraulic jump modelling in large-dams operation. As such, it is a decisive methodological step forward for successful adaptation of existing stilling basins to higher discharges than those considered in their original design. This adaptation becomes even more important under the unquestionable future context of climate change, together with increasing society demands concerning safety standards for flood protection. It is precisely the energy dissipation that constitutes the most challenging part in the adaptation process of a dam, from a technical and economical point of view [5], [17]. Thus, reliable modelling of the hydraulic jump taking place in the stilling basin is the key question to successfully face this challenging engineering issue.

The most relevant specific contributions achieved in the research are highlighted herein. Firstly, the interaction of the different processes involved in the hydraulic jump flow was addressed by studying the phenomenon with multiple techniques. The systematic physical and numerical modelling approach employed allowed benefiting from the complementary nature of this double perspective. In addition to the

aforementioned double perspective itself, the application of each particular approach was remarkably detailed. On the one hand, two different CFD codes were used in the present research. This kind of benchmarking is agreed to be an advisable practice, crucial to achieve reliable comparisons [28], [30]. Furthermore, the numerical simulations were set testing different turbulence models and boundary conditions [70], [99], together with the corresponding mesh convergence analysis [118]. On the other hand, for the experimental approach, three different physical models were developed. In each one of them, a wide variety of experimental instrumentation was employed; even to gather information on a single variable. Contrasting measurements from different techniques is of paramount importance in the study of complex characteristics like the ones associated with the hydraulic jump nature. Among the techniques applied, not only traditional instrumentation was employed. Hence, it is important to highlight the use of innovative techniques in the hydraulic jump study such as the DIP [29] or the LIDAR [59], [60]. Finally, an extensive bibliographic review was carried out to build a detailed state-of-the-art which provided with data and analytical expressions to support the developed models. In certain particular cases, such expressions were not only employed, but also adapted and improved on the basis of the findings achieved in the present research [5].

Overall, these contributions must be considered as a thorough attempt to develop the hydraulic jump knowledge. The combined use of experimental techniques provides an improved representation of the hydraulic jump flow, as compared with previous results in the literature, using techniques with undoubtedly future potential. These experimental results, supported with bibliographic information, allowed developing consistent CFD models. The possibilities of these calibrated and validated models go beyond the theoretical study of the phenomenon to reach key practical applications in hydraulic engineering. Thus, the presented methodology, resulting in a multiple modelling perspective, is of utmost importance for the engineering objective described above.

In particular, the research here presented approached the hydraulic jump study addressing, in the first place, the basis of the phenomenon. Hence, a classical hydraulic jump (CHJ) was characterised through the analysis of its most relevant features. Once the basic structural properties of the phenomenon were investigated, its practical interest was brought into the spotlight. To this end, the hydraulic jump occurring in an energy dissipation stilling basin was studied. The application of the gained knowledge on the hydraulic jump and its particularities in an energy dissipation structure were

intended to improve the performance of large-dam stilling basins. All this research was conducted on the basis of the previously mentioned physical and numerical modelling approach.

For the CHJ, this research offered an insight on several relevant structural properties of a classical hydraulic jump of $Fr_1 = 6$ and $Re_1 = 210{,}000$. The choice of this high Reynolds number, although implying a very significant increase in experimental costs, represents a key contribution of the research with respect to previous developments. This Reynolds number minimises scale effects [22], thus providing a reliable extrapolation of the results, which were representative of the preferable hydraulic jumps employed in large-dam stilling basins for energy dissipation purposes [6]. In this first step, the numerical models developed using the CFD codes FLOW-3D® and OpenFOAM were assessed and contrasted with experimental data collected in a specifically designed physical model and bibliographic results coming from an extensive literature review.

The CHJ free surface profile was accurately reproduced by the presented models, with both numerical codes showing similar results. In spite of this, the presence of bubbles and droplet ejection, combined with the intense free surface turbulence, introduced a certain degree of bias, which especially affected the physical model measurements. In regards with other CHJ variables directly related with the free surface profile, like the sequent depths ratio and the hydraulic jump efficiency, both the physical and the numerical models provided an accurate representation, in comparison with previous bibliographic results. In the estimation of the hydraulic jump roller length, a general good agreement was also observed between the presented models and previous research on the topic.

Regarding the hydraulic jump velocity field, the maximum velocity decay was successfully reproduced by both CFD codes, in good agreement with the physical model too. However, significant differences were found for the maximum backwards velocities. OpenFOAM results were close to the bibliographic information, whereas FLOW-3D® was in the line of the experimental results. For the streamwise velocity vertical profiles, the developed models achieved a high level of accuracy in the hydraulic jump roller region. It should be highlighted that for both CFD codes, the dimensionless velocity profiles were almost coincident, regardless of their position inside the roller. For the physical model, despite the generally satisfactory results, slightly larger differences were found due to the limitations of the experimental

instrumentation in regards with intense fluctuations and aeration. Outside the roller region, the supercritical velocity profiles pattern was adequately reproduced by the models, in accordance with bibliographic analytical expressions. In contrast, the trends found for the velocity profiles in the subcritical flow regime showed important discrepancies, explained by the hydraulic jump roller proximity to some of the involved sections. The subcritical flow velocity information also allowed presenting an estimation of the hydraulic jump length.

Pressures distribution along the streambed was accurately reproduced by the numerical models, which provided results almost coincident with those reported in previous studies. Regarding pressure fluctuations, there were some differences since the modelled results tended to overestimate the bibliographic observations for positions far from the hydraulic jump toe, despite the good agreement in the determination of the position for the peak fluctuations. On the contrary, it was difficult to find a defined trend for experimental results, as a consequence of the limitations bound to the instrumentation employed.

To sum up, the analysis developed regarding the CHJ showed that the double modelling approach using CFD numerical simulations and experimental results successfully reproduced the main structural properties of the hydraulic jump. However, there was a slight lack of precision in the representation of some internal flow details. The difficulties to reach a total accuracy were expected since the knowledge and understanding of the hydraulic jump at its different scales remains limited and therefore, potential advances achieved with CFD techniques constitute a promising research line, which is undoubtedly worth developing.

Having assessed the ability of the developed methodology to reproduce the phenomenon under study, the analysis of an energy dissipation stilling basin was carried out. A general and representative case study consisting in a typified USBR II stilling basin was analysed. The study, involving the CFD code FLOW-3D® and two physical models, was intended to assess the particular characteristic of the hydraulic jump in a large-dam stilling basin, as well as the affection of the energy dissipation devices to the flow.

The models adequately represented the hydraulic jump in the stilling basin. In terms of the hydraulic jump free surface profile, its sequent depths ratio and efficiency, the numerical and the physical models reached successful results, in good agreement with previous research. Nevertheless, some slight differences were found between the

numerical and the physical models, being FLOW-3D® results closer to those for a CHJ. The roller length was also adequately estimated with both modelling approaches, in accordance with bibliographic data, despite a defined trend could not be identified.

Regarding the velocity distribution analysis, the influence of the energy dissipation devices existing in the typified USBR II stilling basin was revealed. The streamwise velocity vertical profiles obtained along the hydraulic jump roller region showed the changes in the velocity profiles associated to the flow deflection in the chute blocks. This affection was also noticed in the maximum velocity decay and the maximum backwards velocities. In addition, the velocity profiles obtained in the subcritical flow regime reflected the influence of the end sill in the flow. In these terms, pressures were also analysed in the end sill, showing results in the line of previous observations. Streambed pressure fluctuations were also addressed upstream and downstream this energy dissipation device for the numerical model. The results showed a decrease of these fluctuations downstream the end sill, in accordance with bibliographic results.

Finally, for the void fraction distribution, an extensive analysis was carried out, based on a reformulation of a void fraction profile analytical expression. The information collected for the physical model showed the ability of the optical fibre probe to provide a representation of the aeration process with a high level of accuracy. The model was also able to reflect the influence of the energy dissipation devices on the flow, in comparison with the CHJ void fraction profiles. Hence, the observed influence revealed a more intense air entrainment and larger flow depth values close to the hydraulic jump toe, in good agreement with the free surface profile analysis. In contrast, the numerical model showed acceptable results for the lower region, but was not able to accurately reproduce the aeration mechanisms occurring in the upper region, where interactions with the free surface dominate.

Despite very few limitations which have been clearly identified, the numerical and physical models developed showed their ability to adequately reproduce the flow under study. Hence, the presented research encourages the use of methodologies based on a double numerical and physical modelling approach in the study of complex flows in hydraulic structures. In particular, the results here reported contribute to the enhancement of the knowledge concerning the classical hydraulic jump and the flow in a typified USBR II stilling basin. These results can definitely be used to improve the design of large-dam stilling basins and their adaptation to more demanding scenarios.

Chapter 7. Future Outlook

The results and findings obtained for the research here presented confirm the enormous potential of numerical and physical modelling in hydraulic engineering applications. The wide range of possibilities offered by these complementary modelling approaches must guide the research to enhance the current knowledge on complex flows such as the hydraulic jump phenomenon and to improve the performance of key engineering structures like the ones intended for energy dissipation purposes in large dams. This was precisely the aim of the research here presented. Nevertheless, the works conducted for this research addressed a specific scope, and the number of methods applied and cases studied remained logically limited.

Hence, it is precisely the will to overcome the limitations of this study that should guide further research on the topic. In the first place, CFD techniques constitute a relatively recent tool to address hydraulic engineering applications. Despite these techniques have rapidly achieved a crucial role, they still have room for improvement [28]–[30], especially when treating complex flows such as the ones here approached. In these terms, numerical CFD simulations are bound to the available computational capabilities, which are exponentially growing. Consequently, more detailed and precise approaches to the resolution of the flow governing equations, which have already showed their potential [67], [68], must be considered in the future. In addition, community-based benchmarking and more accurate sub-grid and turbulence models are constantly being developed [28]. Apart from the undeniable potential of CFD techniques, they are already offering a large number of options for numerically modelling hydraulic phenomena. Thus, there is a wide combination of turbulence models, meshing procedures, boundary conditions, etc. that goes beyond the results here presented. Testing and exploring all of these possibilities would undoubtedly extend and improve this research.

For the physical modelling process, it constitutes an indispensable tool to address hydraulic engineering problems [5], [18]. However, there is a series of unavoidable limitations bound to the available laboratory resources. Hence, even if the recommendations and guidelines are strictly followed, it is not always possible to reach the dimensions and hydraulic conditions that ensure a minimum affection of the scale effects in the results [22]. Furthermore, time requirements in the experimental

campaign or the lack of specific instrumentation usually prevent from obtaining information in every position and under every condition for all of the relevant features analysed. These limitations join the inherent uncertainty of some experimental techniques [12]. Thus, this research would be enhanced by developing new physical models and by using new instrumentation which would lead to extended experimental campaigns. These results in turn, could be used to calibrate and validate the routines and parameters set in the numerical models, hence improving their performance.

In these terms, further research from the numerical and physical modelling perspective would improve the characterisation of the hydraulic jump aeration together with the velocity and pressure fields. Furthermore, a wider range of inflow conditions (Fr_1, Re_1, We_1) could be tested. This would provide confirmation for a series of results already detected such as the effect of aeration in the hydraulic jump shape, the influence of the energy dissipation devices on the hydraulic jump features and dimensions, or the actual hydraulic jump length. These findings must provide new recommendations for hydraulic structures such as the widely spread typified stilling basins whose design, despite having proved its efficiency, dates back many decades [6]. The improvements hence achieved, may be helpful not only for the construction of new structures, but also for the adaptation of existing stilling basins that must cope with larger discharges than those considered in their design phase (Figure 42).

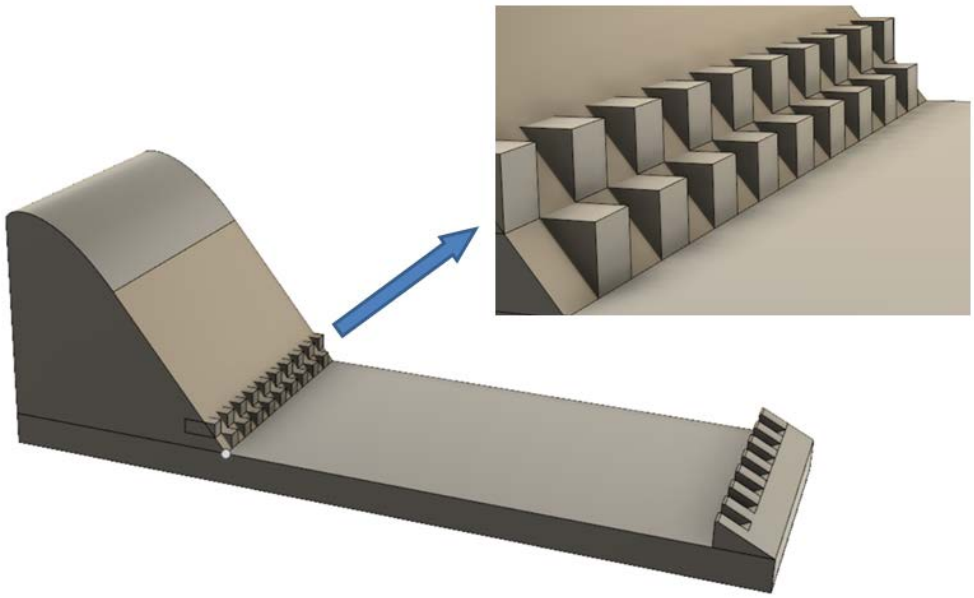

Figure 42. Possible modification in the design of a typified USBR II stilling basin for its adaptation to larger discharges.

Figure 42 shows a typified USBR II stilling basin in which an additional second row of chute blocks has been attached. The research project 'La aireación del flujo y su implementación en prototipo para la mejora de la disipación de energía de la lámina vertiente por resalto hidráulico en distintos tipos de presas' (BIA2017-85412-C2-1-R), developed in the Hydraulics Laboratory of the Department of Hydraulic Engineering and Environment at the Universitat Politècnica de València (UPV, Spain) and funded by the Spanish Ministry of Economy is directly related with the research here presented. This project seeks for the adaptation of existing dams to new standards derived from climate change effects and society demands regarding flood protection. Results from this research showed that forcibly aerating the incoming flow to the dissipation structure enhances the performance of the basin so that it can cope with the more demanding discharges [17], [136]. Following this line, the research here presented noted the influence of the energy dissipation devices on the air entrainment process. Hence, Figure 42 exemplifies one of the multiple configurations regarding energy dissipation devices size, shape or location that could be tested to improve the performance of the structure. However, further research is not limited to this typified stilling basin. There are plenty of typified and *ad hoc* designed stilling basins that can

be studied through the double modelling approach here presented, providing a better insight to the hydraulic jump phenomenon.

Actually, the methodology here presented has been used during the research to approach hydraulic engineering flows and phenomena beyond the hydraulic jump. For instance, the design of experimental hydraulic installations to quantify energy losses, such as the Venturi tube, was addressed by the means of CFD modelling [137]. Furthermore, real-life hydraulic engineering cases such as the analysis of the dam bottom spillway for a hydroelectric power plant in Mequinenza (Zaragoza, Spain) were addressed [138] (Figure 43).

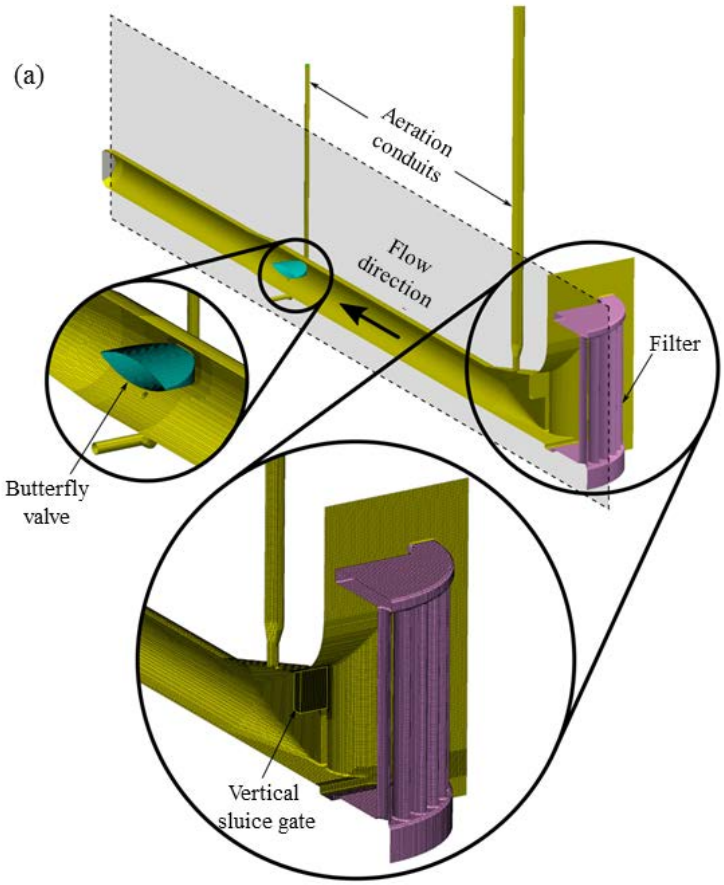

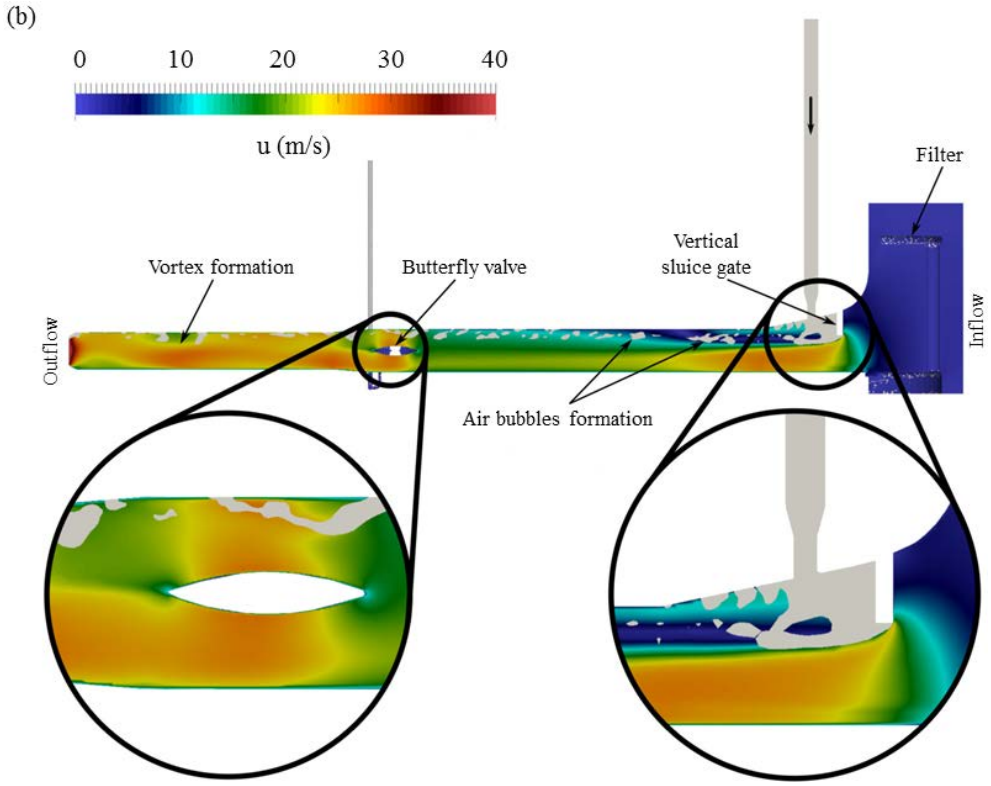

Figure 43. Mequinenza dam (Zaragoza, Spain) bottom spillway CFD analysis [138]: (a) Case study geometry, (b) Velocity field.

Hence, regarding the hydraulic engineering field, a promising potential arises for the methodology here developed, that oversteps the research interest to reach real-life applications. The wide variety of existing experimental techniques and CFD codes, which are constantly improving, ensures the possibility to contribute to a better understanding of complex flows by following multiple future research lines. Among the existing wide range of numerical and physical modelling applications, the humble intention of this research was to constitute a first step towards an improved performance of large-dam stilling basins through an enhanced knowledge of the hydraulic jump phenomenon.

References

[1] Vischer, D. L. and Hager, W. H. (1998). *Dam hydraulics*. John Wiley & Sons, Chichester, West Sussex, United Kingdom.

[2] Hager, W. H. (1992). *Energy dissipators and hydraulic jump*. Springer Science & Business Media, Dordrecht, The Netherlands.

[3] International Comission On Large Dams, "Number of Dams by Country Members," 2018. [Online]. Available: https://www.icold-cigb.org/article/GB/world_register/general_synthesis/number-of-dams-by-country-members. [Accessed: 24-Mar-2020].

[4] Ministerio para la Transición Ecológica y el Reto Demográfico. (2018). *Normas Técnicas de Seguridad para las Grandes Presas y sus Embalses*. Gobierno de España, España.

[5] Macián-Pérez, J. F., García-Bartual, R., Huber, B., Bayon, A. and Vallés-Morán, F. J. (2020). "Analysis of the Flow in a Typified USBR II Stilling Basin through a Numerical and Physical Modeling Approach," *Water*, vol. 12, no. 1, p. 227.

[6] Peterka, A. J. (1978). *Hydraulic design of stilling basins and energy dissipators*. US Department of the Interior, Bureau of Reclamation, Washington DC, United States of America.

[7] Murthy, Y. K. and Divatia, E. (1982). "Behaviour of Stilling Basins in Large Spillways," *Water Energy Int.*, vol. 39, no. 2, pp. 181–188.

[8] Wang, H. and Chanson, H. (2015). "Experimental Study of Turbulent Fluctuations in Hydraulic Jumps," *J. Hydraul. Eng.*, vol. 141, no. 7, p. 04015010.

[9] Wang, H. (2014). "Turbulence and air entrainment in hydraulic jumps," PhD Thesis. The University of Queenslands, Australia.

[10] Liu, M., Rajaratnam, N. and Zhu, D. Z. (2004). "Turbulence structure of hydraulic jumps of low Froude numbers," *J. Hydraul. Eng.*, vol. 130, no. 6, pp. 511–520.

[11] Montes, J. S. and Chanson, H. (1998). "Characteristics of undular hydraulic jumps: experiments and analysis," J. *Hydraul. Eng*., vol. 124, no. 2, pp. 192–205.

[12] Valero, D. Viti, N. and Gualtieri, C. (2019). "Numerical Simulation of Hydraulic Jumps. Part 1: Experimental Data for Modelling Performance Assessment," *Water*, vol. 11, no. 1, p. 36.

[13] Blaisdell, F. W. (1948). "Development and hydraulic design, Saint Anthony Falls stilling basin," *Trans. Am. Soc. Civ. Eng*., vol. 113, no. 1, pp. 483–520.

[14] Kuttiammu ,T. P. and Rao, J. V. (1951). "Bhavani type stilling basin for spillways of large dams," in *IV ICOLD Congress, New Delhi, India*, vol. 12, pp. 397–414.

[15] Yuditskii, G. A. (1965). "Erosion par cavitation des dissipateurs d'énergie des barrages-déversoirs et les mesures de son élimination," in *XI IAHR Congress, St. Petersburg, Russia*, vol. 1, no. 8, pp. 1–12.

[16] Gunko, F. G. (1967). "Macroturbulence of Flows Below Spillways of Medium Head Dams and Their Protection Against Undermining," in *XII IAHR Congress, Fort Collins, CO, United States of America*, pp. 135-143.

[17] Fernández-Bono, J. F. and Vallés-Morán, F. J. (2006). "Criterios metodológicos de adaptación del diseño de cuencos de disipación de energía a pie de presa con resalto hidráulico, a caudales superiores a los de diseño," in *XXII Congreso Latinoamericano de Hidráulica, Ciudad Guayana, Venezuela*.

[18] Liu, Z.-P., Guo, X.-L., Xia, Q.-F., Fu, H., Wang, T. and Dong, X.-L. (2018). "Experimental and numerical investigation of flow in a newly developed vortex drop shaft spillway," *J. Hydraul. Eng*., vol. 144, no. 5, p. 04018014.

[19] Wang, H. and Chanson, H. (2015). "Air entrainment and turbulent fluctuations in hydraulic jumps," *Urban Water J*., vol. 12, no. 6, pp. 502–518.

[20] Chanson, H. (2009). “Turbulent air–water flows in hydraulic structures: dynamic similarity and scale effects,” *Environ. fluid Mech*., vol. 9, no. 2, pp. 125–142.

[21] Chanson, H. and Gualtieri, C. (2008). “Similitude and scale effects of air entrainment in hydraulic jumps,” *J. Hydraul. Res*., vol. 46, no. 1, pp. 35–44.

[22] Heller, V. (2011). “Scale effects in physical hydraulic engineering models,” *J. Hydraul. Res.*, vol. 49, no. 3, pp. 293–306.

[23] Hager, W. H. and Bremen, R. (1989). “Classical hydraulic jump: sequent depths,” *J. Hydraul. Res.*, vol. 27, no. 5, pp. 565–585.

[24] Chanson, H. (2006). “Bubble entrainment, spray and splashing at hydraulic jumps,” *J. Zhejiang Univ. A*, vol. 7, no. 8, pp. 1396–1405.

[25] Bayón, A. and López-Jiménez, P. A. (2015). “Numerical analysis of hydraulic jumps using OpenFOAM,” *J. Hydroinformatics*, vol. 17, no. 4, pp. 662–678.

[26] Zhang, G., Wang, H. and Chanson, H. (2013). “Turbulence and aeration in hydraulic jumps: free-surface fluctuation and integral turbulent scale measurements,” *Environ. fluid Mech.*, vol. 13, no. 2, pp. 189–204.

[27] Chanson, H. (2013). “Hydraulics of aerated flows: qui pro quo?,” *J. Hydraul. Res*., vol. 51, no. 3, pp. 223–243.

[28] Viti, N., Valero, D. and Gualtieri, C. (2019). “Numerical Simulation of Hydraulic Jumps. Part 2: Recent Results and Future Outlook,” *Water*, vol. 11, no. 1, p. 28.

[29] Bayón, A., Valero, D., García-Bartual, R., Vallés-Morán, F. J. and López-Jiménez, P. A. (2016). “Performance assessment of OpenFOAM and FLOW-3D in the numerical modeling of a low Reynolds number hydraulic jump,” *Environ. Model. Softw.*, vol. 80, pp. 322–335.

[30] Blocken, B. and Gualtieri, C. (2012). “Ten iterative steps for model development and evaluation applied to Computational Fluid Dynamics for Environmental Fluid Mechanics,” *Environ. Model. Softw*., vol. 33, pp. 1–22.

[31] Chanson, H. (2015). *Energy dissipation in hydraulic structures*. CRC Press, Leiden, The Netherlands.

[32] Bidone, G. (1820). *Expériences sur le remou et sur la propagation des ondes par George Bidone*. Imprimerie Royale, Paris, France.

[33] Bélanger, J. B. (1841). *Notes sur l'Hydraulique*. Ec. R. des Ponts Chaussées, Paris, France.

[34] Darcy, H. and Bazin, H. É. (1865). *Recherches hydrauliques enterprises*. Imprimerie Nationale, Paris, France.

[35] Boussinesq, J. (1877). *Essai sur la théorie des eaux courantes*. Imprimerie Nationale, Paris, France.

[36] Safranez, K. M. (1927). "Wechselsprung und die Energievernichtung des Wassers," PhD Thesis. Germany.

[37] Bakhmeteff, B. A. (1932). *Hydraulics of open channels*. McGraw-Hill, New York, NY, United States of America.

[38] Rouse, H. (1934). "On the use of dimensionless numbers," *Civ. Eng.*, vol. 4, no. 11, pp. 563–568.

[39] Bakhmeteff, B. A. and Matzke, A. E. (1936). "The Hydraulic Jump In Terms of Dynamic Similarity," *Trans. Am. Soc. Civ. Eng.*, vol. 101, no. 1, pp. 630–647.

[40] Rouse, H., Siao,T. T. and Nagaratnam, S. (1958). "Turbulence characteristics of the hydraulic jump," *J. Hydraul. Div.*, vol. 84, no. 1, pp. 1–30.

[41] Rajaratnam, N. (1965). "The hydraulic jump as a well jet," *J. Hydraul. Div.*, vol. 91, no. 5, pp. 107–132.

[42] Schröder, R. (1963). *Die turbulente Strömung im freien Wechselsprung*. Institut für Wasserbau und Wasserwirtschaft, TU Berlin, Berlin, Germany.

[43] Resch, F. J. and Leutheusser, H. J. (1972). "Reynolds stress measurements in hydraulic jumps," *J. Hydraul. Res.*, vol. 10, no. 4, pp. 409–430.

[44] Abdul Khader, M. H. and Elango, K. (1974). “Turbulent pressure field beneath a hydraulic jump,” *J. Hydraul. Res*., vol. 12, no. 4, pp. 469–489.

[45] Rouse, H. (1970). “Work-energy equation for the streamline,” *J. Hydraul. Div*., vol. 96, no. 5, pp. 1179–1190.

[46] Narayanan, R. (1975). “Wall jet analogy to hydraulic jump,” *J. Hydraul. Div*., vol. 101, no. 3, pp. 347–359.

[47] McCorquodale, J. A. and Khalifa, A. (1983). “Internal flow in hydraulic jumps,” *J. Hydraul. Eng.*, vol. 109, no. 5, pp. 684–701.

[48] Hager, W. H., Bremen, R. and Kawagoshi, N. (1990) “Classical hydraulic jump: length of roller,” *J. Hydraul. Res*., vol. 28, no. 5, pp. 591–608.

[49] Toso, J. W. and Bowers, C. E. (1988). “Extreme pressures in hydraulic-jump stilling basins,” *J. Hydraul. Eng*., vol. 114, no. 8, pp. 829–843.

[50] Mossa, M. (1999). “On the oscillating characteristics of hydraulic jumps,” *J. Hydraul. Res*., vol. 37, no. 4, pp. 541–558.

[51] Chanson, H. and Brattberg, T. (2000). “Experimental study of the air–water shear flow in a hydraulic jump,” *Int. J. Multiph. Flow*, vol. 26, no. 4, pp. 583–607.

[52] Murzyn, F., Mouaze, D. and Chaplin, J. R. (2005). “Optical fibre probe measurements of bubbly flow in hydraulic jumps,” *Int. J. Multiph. Flow*, vol. 31, no. 1, pp. 141–154.

[53] Gualtieri, C. and Chanson, H. (2007). “Experimental analysis of Froude number effect on air entrainment in the hydraulic jump,” *Environ. Fluid Mech*., vol. 7, no. 3, pp. 217–238.

[54] Witt, A., Gulliver, J. and Shen, L. (2015). “Simulating air entrainment and vortex dynamics in a hydraulic jump,” *Int. J. Multiph. Flow*, vol. 72, pp. 165–180.

[55] Xiang, M., Cheung, S. C. P., Tu, J. Y. and Zhang, W. H. (2014). “A multi-fluid modelling approach for the air entrainment and internal bubbly flow region in hydraulic jumps,” *Ocean Eng*., vol. 91, pp. 51–63.

[56] Wang, H. and Murzyn, F. (2017). "Experimental assessment of characteristic turbulent scales in two-phase flow of hydraulic jump: from bottom to free surface," *Environ. Fluid Mech.*, vol. 17, no. 1, pp. 7–25.

[57] Jesudhas, V., Balachandar, R., Roussinova, V. and Barron, R. (2018). "Turbulence characteristics of classical hydraulic jump using DES," *J. Hydraul. Eng*., vol. 144, no. 6, p. 04018022.

[58] Chachereau, Y. and Chanson, H. (2011). "Free-surface fluctuations and turbulence in hydraulic jumps," *Exp. Therm. Fluid Sci*., vol. 35, no. 6, pp. 896–909.

[59] Montano, L., Li, R. and Felder, S. (2018). "Continuous measurements of time-varying free-surface profiles in aerated hydraulic jumps with a LIDAR," *Exp. Therm. Fluid Sci*., vol. 93, pp. 379–397.

[60] Montano, L. and Felder, S. (2020). "LIDAR Observations of Free-Surface Time and Length Scales in Hydraulic Jumps," *J. Hydraul. Eng*., vol. 146, no. 4, p. 04020007.

[61] Cheng, C.-K., Tai, Y.-C. and Jin, Y.-C. (2017). "Particle image velocity measurement and mesh-free method modeling study of forced hydraulic jumps," *J. Hydraul. Eng*., vol. 143, no. 9, p. 04017028.

[62] Caisley, M. E., Bombardelli, F. A. and Garcia, M. H. (1999). *Hydraulic model study of a Canoe Chute for low-head Dams in Illinois*. Hydraulic Engineering Series, University of Illinois, United States of America.

[63] Gonzalez, A. and Bombardelli, F. (2005). "Two-phase-flow theoretical and numerical models for hydraulic jumps, including air entrainment," in *Proceedings of the Korea Water Resources Association Conference, South Korea*, pp. 28–29.

[64] Romagnoli, M., Portapila, M. and Morvan, H. (2009). "Computational simulation of a hydraulic jump," *Mec. Comput*., vol. 28, pp. 1661–1672.

[65] Ma, J., Oberai, A. A., Lahey, R. T. and Drew, D. A. (2011). "Modeling air entrainment and transport in a hydraulic jump using two-fluid RANS and DES turbulence models," *Heat mass Transf.*, vol. 47, no. 8, p. 911.

[66] Langhi, M. and Hosoda, T. (2018). “Three-dimensional unsteady RANS model for hydraulic jumps,” *ISH J. Hydraul. Eng.*, pp. 1–8.

[67] Lubin, P., Glockner, S. and Chanson, H. (2009). “Numerical simulation of air entrainment and turbulence in a hydraulic jump,” in *Colloque SHF, Lyon et Grenoble, France*.

[68] Mortazavi, M., Le Chenadec, V., Moin, P. and Mani, A. (2016). “Direct numerical simulation of a turbulent hydraulic jump: turbulence statistics and air entrainment,” *J. Fluid Mech.*, vol. 797, pp. 60–94.

[69] Zhao, Q., Misra S. K., Svendsen, I. A. and Kirby, J. T. (2004) “Numerical study of a turbulent hydraulic jump,” in *17th ASCE Engineering Mechanics Conference, Newark, DE, United States of America*.

[70] Bayón, A., Macián-Pérez, J. F., Vallés-Morán, F. J. and López-Jiménez, P. A., (2019). “Effect of RANS turbulence model in hydraulic jump CFD simulations,” in *E-proceedings of the 38th IAHR World Congress, Panama City, Panama*.

[71] Riegel, R. M. and Beebe, J. C. (1928). *The hydraulic jump as a means of dissipating energy*. Miami Conservancy Distric, United States of America.

[72] Rehbock, T. (1925). *Die Bekämpfung der Sohlen-Auskolkung bei Wehren durch Zahnschwellen*. Buchdr. CF Müller, Germany.

[73] Chitale, S. V. (1959). “Energy Dissipation in Hydraulic Jump below Weirs and Falls,” *Water Energy Int.*, vol. 16, no. 4, pp. 465–477.

[74] Lopardo, R. A., De Lio, J. C. and Vernet, G. F. (1982). “Physical modelling on cavitation tendency for macroturbulence of hydraulic jump,” in *Int. Conf. Hydraulic Modelling of Civil Engineering Structures, Coventry, United Kingdom*.

[75] Rahmeyer, W. (1988). “Alternate Designs for the Sidewalls of Hydraulic Jump Stilling Basins,” in *Hydraulic Engineering*, pp. 963–968.

[76] Ohtsu, I., Yasuda,Y. and Yamanaka, Y. (1991). “Drag on vertical sill of forced jump,” *J. Hydraul. Res.*, vol. 29, no. 1, pp. 29–47.

[77] Hager, W. H. and Li, D. (1992). “Sill-controlled energy dissipator,” *J. Hydraul. Res.*, vol. 30, no. 2, pp. 165–181.

[78] Carvalho, R. F., Lemos, C. M. and Ramos, C. M. (2008). “Numerical computation of the flow in hydraulic jump stilling basins,” *J. Hydraul. Res.*, vol. 46, no. 6, pp. 739–752.

[79] Wang, Y., Bao, Z. and Wang, B. (2012). “Three-dimensional numerical simulation of flow in stilling basin based on Flow-3D,” *Eng. J. Wuhan Univ.*, vol. 45, no. 4, pp. 454–458.

[80] Tajabadi, F., Jabbari, E. and Sarkardeh, H. (2017). “Hydrodynamic analysis of flow in USBR stilling basin types I, II, III,” *J. Dam Hydroelectr. Powerpl.*, vol. 4, no. 13, pp. 43–54.

[81] Valero, D., Bung, D. B. and Crookston, B. M. (2018). “Energy dissipation of a Type III basin under design and adverse conditions for stepped and smooth spillways,” *J. Hydraul. Eng.*, vol. 144, no. 7, p. 04018036.

[82] Wu, J., Zhou, Y. and Ma, F. (2018). “Air entrainment of hydraulic jump aeration basin,” *J. Hydrodyn.*, vol. 30, no. 5, pp. 962–965.

[83] Padulano, R., Fecarotta, O., Del Giudice, G. and Carravetta, A. (2017). “Hydraulic design of a USBR Type II stilling basin,” *J. Irrig. Drain. Eng.*, vol. 143, no. 5, p. 04017001.

[84] Fecarotta, O., Carravetta, A., Del Giudice, G., Padulano, R., Brasca, A. and Pontillo, M. (2016). “Experimental results on the physical model of an USBR type II stilling basin.,” in *Proceedings of Riverflow 2016—8th Int. Conf. on Fluvial Hydraulics, St. Louis, United States of America*.

[85] Macián-Pérez, J. F., García-Bartual, R., Huber, B., Bayón, A. and Vallés-Morán, F. J. (2019). “Approach to the void fraction distribution within a hydraulic jump in a typified USBR II stilling basin,” in *E-proceedings of the 38th IAHR World Congress, Panama City, Panama*.

[86] Flow Science Inc. (2017). *Flow-3D User Manual*. Flow Science Inc., Santa Fe, NM, United States of America.

[87] McDonald, P. W. (1971). “The computation of transonic flow through two-dimensional gas turbine cascades,” in *ASME 1971 International Gas Turbine Conference and Products Show, Houston, TX, United States of America*.

[88] Hirt, C. W. and Nichols, B. D. (1981). “Volume of fluid (VOF) method for the dynamics of free boundaries,” *J. Comput. Phys*., vol. 39, no. 1, pp. 201–225.

[89] Dong, Z., Wang, J., Vetsch, D. F., Boes, R. M. and Tan, G. (2019). “Numerical Simulation of Air–Water Two-Phase Flow on Stepped Spillways behind X-Shaped Flaring Gate Piers under Very High Unit Discharge,” *Water*, vol. 11, no. 10, p. 1956.

[90] Valero, D. and Bung, D. B. (2016). “Sensitivity of turbulent Schmidt number and turbulence model to simulations of jets in crossflow,” *Environ. Model. Softw*., vol. 82, pp. 218–228.

[91] Sarfaraz, M. and Attari, J. (2011). “Numerical Simulation of Uniform Flow Region over a Steeply Sloping Stepped Spillway,” in *6th National Congress on Civil Engineering, Semnan University, Semnan, Iran*.

[92] Ho, D. K. H. and Riddette, K. M. (2010). “Application of computational fluid dynamics to evaluate hydraulic performance of spillways in Australia,” *Aust. J. Civ. Eng*., vol. 6, no. 1, pp. 81–104.

[93] Weller, H. G., Tabor, G., Jasak, H. and Fureby, C. (1998). “A tensorial approach to computational continuum mechanics using object-oriented techniques,” *Comput. Phys*., vol. 12, no. 6, pp. 620–631.

[94] Teuber, K., Broecker, T., Bayón, A., Nützmann, G. and Hinkelmann, R. (2019). “CFD-modelling of free surface flows in closed conduits,” *Prog. Comput. Fluid Dyn. an Int. J*., vol. 19, no. 6, pp. 368–380.

[95] Fuentes-Pérez, J. F., Silva, A. T., Tuhtan, J. A., García-Vega, A., Carbonell-Baeza, R., Musall, M., and Kruusmaa, M. (2018). “3D modelling of non-uniform and turbulent flow in vertical slot fishways,” *Environ. Model. Softw*., vol. 99, pp. 156–169.

[96] Rodi, W., Constantinescu, G. and Stoesser, T. (2013). *Large-eddy simulation in hydraulics*. CRC Press, Leiden, The Netherlands.

[97] Spalart, P. R. (1997). “Comments on the feasibility of LES for wings, and on a hybrid RANS/LES approach,” in *Proceedings of first AFOSR international conference on DNS/LES, Ruston, LO, United States of America*.

[98] Pope, S. B. (2001). “Turbulent Flows,” *Meas. Sci. Technol.*, vol. 12, no. 11, pp. 2020–2021.

[99] Macián-Pérez, J. F., Huber, B., Bayón, A., García-Bartual, R. and Vallés-Morán, F. J. (2019). “Influencia de la elección del modelo de turbulencia en el análisis numérico CFD de un cuenco amortiguador tipificado USBR II,” in *VI Jorandas de Ingeniería del Agua, Toledo, Spain*.

[100] Harlow, F. H. and Nakayama, P. I. (1967). “Turbulence transport equations,” *Phys. Fluids*, vol. 10, no. 11, pp. 2323–2332.

[101] Launder, B. E. and Sharma, B. I. (1974). “Application of the energy-dissipation model of turbulence to the calculation of flow near a spinning disc,” *Lett. heat mass Transf.*, vol. 1, no. 2, pp. 131–137.

[102] Rodi, W. (1993). *Turbulence models and their application in hydraulics*. Routledge, London, United Kingdom.

[103] Yakhot, V., Orszag, S. A., Thangam, S., Gatski, T. B. and Speziale, C. G. (1992). “Development of turbulence models for shear flows by a double expansion technique,” *Phys. Fluids A Fluid Dyn.*, vol. 4, no. 7, pp. 1510–1520.

[104] Wilcox, D. C. (1998). *Turbulence modeling for CFD*. DCW industries, La Canada, CA, United States of America.

[105] Menter, F. R. (1994). “Two-equation eddy-viscosity turbulence models for engineering applications,” *AIAA J.*, vol. 32, no. 8, pp. 1598–1605.

[106] Li, S. and Zhang, J. (2018). “Numerical investigation on the hydraulic properties of the skimming flow over pooled stepped spillway,” *Water*, vol. 10, no. 10, p. 1478.

[107] Zhang, W., Wang, J., Zhou, C., Dong, Z. and Zhou, Z. (2018). “Numerical simulation of hydraulic characteristics in a vortex drop shaft,” *Water*, vol. 10, no. 10, p. 1393.

[108] Bombardelli, F. A., Meireles, I. and Matos, J. (2011). "Laboratory measurements and multi-block numerical simulations of the mean flow and turbulence in the non-aerated skimming flow region of steep stepped spillways," *Environ. Fluid Mech.*, vol. 11, no. 3, pp. 263–288.

[109] Falvey, H. T. (1980). "Air-water flow in hydraulic structures," *NASA STI/Recon Tech. Rep. N*, vol. 81.

[110] Valero, D. (2018). "On the Fluid Mechanics of Self-Aeration in Open Channel Flows," PhD Thesis. Université de Liège, Belgium.

[111] Valero, D. and Bung, D. B. (2015). "Hybrid investigations of air transport processes in moderately sloped stepped spillway flows," in *E-proceedings of the 36th IAHR World Congress, The Hague, The Netherlands*.

[112] Brethour, J. M. and Hirt, C. W. (2009). "Drift model for two-component flows," *FSI-09-TN83Rev. Flow Sci. Inc*.

[113] Richardson, J. F. and Zaki, W.N. (1954). "Sedimentation and fluidization," *Trans. Instn. chem. Engrs. Bd*, vol. 32, p. 35.

[114] Biswas, R. and Strawn, R. C. (1998). "Tetrahedral and hexahedral mesh adaptation for CFD problems," *Appl. Numer. Math.*, vol. 26, no. 1–2, pp. 135–151.

[115] Hirsch, C. (2007). *Numerical computation of internal and external flows: The fundamentals of computational fluid dynamics*. John Wiley & Sons, Chichester, West Sussex, United Kingdom.

[116] Keyes, D., Ecer, A., Satofuka, N., Fox, P. and Periaux, J. (2000). *Parallel Computational Fluid Dynamics' 99: Towards Teraflops, Optimization and Novel Formulations*. Elsevier, Amsterdam, The Netherlands.

[117] Kim, S.-E. and Boysan, F. (1999). "Application of CFD to environmental flows," *J. Wind Eng. Ind. Aerodyn.*, vol. 81, no. 1–3, pp. 145–158.

[118] Celik, I. B., Ghia, U., Roache, P. J. and Freitas, C. J. (2008). "Procedure for estimation and reporting of uncertainty due to discretization in CFD applications," *J. fluids Eng. ASME*, vol. 130, no. 7.

[119] Von Karman, T. (1930). “Mechanische ahnlichkeit und turbulenz,” *Math.-Phys. Klasse*.

[120] Castro-Orgaz, O. and Hager, W. H. (2009). “Classical hydraulic jump: Basic flow features,” *J. Hydraul. Res*., vol. 47, no. 6, pp. 744–754.

[121] Şentürk, F. (1994). *Hydraulics of dams and reservoirs*. Water Resources Publication, Littleton, CO, United States of America.

[122] United States Bureau of Reclamation (1987). *Design of small dams*. US Department of the Interior, Bureau of Reclamation, Washington DC,United States of America.

[123] Thompson, A. C. (1987). *Basic hydrodynamics*. Butterworth-Heinemann, Oxford, United Kingdom.

[124] Houichi, L., Ibrahim, G. and Achour, B. (2006). “Experiments for the discharge capacity of the siphon spillway having the Creager-Ofitserov profile,” *Int. J. Fluid Mech. Res*., vol. 33, no. 5.

[125] Cartellier, A. and Achard, J. L. (1991). “Local phase detection probes in fluid/fluid two-phase flows,” *Rev. Sci. Instrum*., vol. 62, no. 2, pp. 279–303.

[126] Cartellier, A. and Barrau, E. (1998). “Monofiber optical probes for gas detection and gas velocity measurements: Conical probes,” *Int. J. Multiph. Flow*, vol. 24, no. 8, pp. 1265–1294.

[127] Boyer, C., Duquenne, A.-M. and Wild, G. (2002). “Measuring techniques in gas–liquid and gas–liquid–solid reactors,” *Chem. Eng. Sci*., vol. 57, no. 16, pp. 3185–3215.

[128] Zhang, G., Valero, D., Bung, D. B. and Chanson, H. (2018). “On the estimation of free-surface turbulence using ultrasonic sensors,” *Flow Meas. Instrum*., vol. 60, pp. 171–184.

[129] Bennett, N.D., Croke, B.F.W., Guariso, G., Guillaume, J.H.A., Hamilton, S.H., Jakeman, A.J., Marsili-Libelli, S., Newham, L.T.H., Norton, J.P., Perrin, C., et al. (2013). “Characterising performance of environmental models,” *Environ. Model. Softw*., vol. 40, pp. 1–20.

[130] Kirkgöz, M. S. and Ardiçlioğlu, M. (1997). "Velocity profiles of developing and developed open channel flow," *J. Hydraul. Eng.*, vol. 123, no. 12, pp. 1099–1105.

[131] Akbari, M. E., Mittal, M. K. and Pande, P. K. (1982). "Pressure fluctuations on the floor of free and forced hydraulic jumps," in *Proceedings of the International Conference Modeling Civil Engineering Structures, Coventry, United Kingdom*, pp. 163–170.

[132] Spoljaric, A. (1984). "Dynamic Characteristics of the Load on the Bottom Plate Under Hydraulic Jump," in *Hydrosoft'84: Hydraulic Engineering Software: Proceedings of the International Conference, Portorož, Slovenia*.

[133] Iaccarino, G., Ooi, A., Durbin, P. A. and Behnia, M. (2003). "Reynolds averaged simulation of unsteady separated flow," *Int. J. Heat Fluid Flow*, vol. 24, no. 2, pp. 147–156.

[134] Chanson, H. (1996). *Air bubble entrainment in free-surface turbulent shear flows*. Academic Press Inc., San Diego, CA, United States of America.

[135] Brattberg, T., Toombes, L. and Chanson, H. (1998). "Developing air-water shear layers of two-dimensional water jets discharging into air," *Am. Soc. Mech. Eng. Fluids Eng. Div. FED*.

[136] Vallés-Morán, F. J., Nácher-Rodríguez, B., Bayón, A., Macián-Pérez, J. F., Marco-Segura, J. B. and López-Jiménez, P. A. (2015) "Generación de resaltos hidráulicos de alto número de Froude a partir de regímenes rápidos emulsionados. Una investigación experimental." in *IV Jornadas de Ingeniería del Agua, Córdoba, Spain*.

[137] Bayón, A., Vallés-Morán, F. J., Macián-Pérez, J. F. and López-Jiménez, P. A. (2017). "Diseño de instalaciones hidráulicas experimentales con apoyo de la dinámica de fluidos computacional (CFD)," *Rev. Hidrolatinoamericana Jóvenes Investig. y Prof.*, no. 1, pp. 23–26.

[138] Bayón, A., Macián-Pérez, J. F., Río, F., Conesa, F. J. and García-lorenzana, D. (2017). "Modelado CFD del flujo aire-agua en un desagüe de fondo de presa," in *V Jornadas Ing. del Agua, A Coruña, Spain*.